# Scattering Studies of Excitations and Phase Transitions

by

Sharon Fulton

Wadham College, University of Oxford

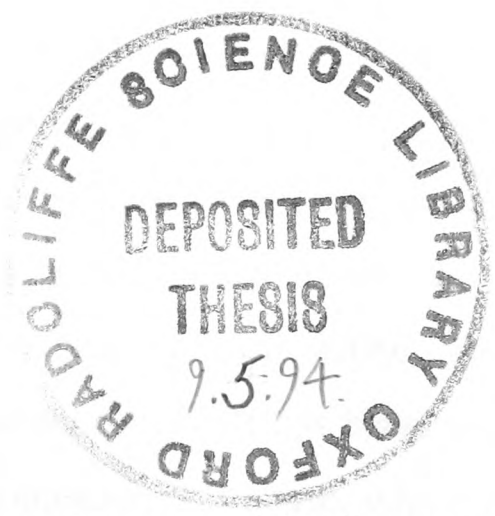


Thesis for the degree of Doctor of Philosophy, Michaelmas Term, 1993.

# Scattering Studies of Excitations and Phase Transitions

**Sharon Fulton, Wadham College**

**Thesis for the degree of Doctor of Philosophy, Michaelmas Term, 1993**

This thesis describes a diversity of scattering experiments on a number of different systems. Using time-of-flight neutron scattering, a study of polycrystalline sodium in the high-momentum limit known as the impulse approximation has been performed. The purpose of this study was to look for anharmonic effects in the neutron recoil scattering of sodium as the temperature was increased from 30K to 300K. No such effects were detected and the results agreed with an isotropic harmonic solid to an accuracy of about 4%. Two experiments were carried out on antiferromagnetic systems using triple-axis neutron scattering techniques to measure the spin-wave dispersion relations. The first was on CuO to verify its description as a spin 1/2 one-dimensional antiferromagnet. The dispersion relation was measured along the chain direction up to an energy transfer of 80meV. This was done above and below the Néel temperature ($T_N$=240K). However, no evidence was seen to justify the description of CuO as a one-dimensional antiferromagnet, with the spin waves behaving like those in a classical three-dimensional system. The other spin-wave study examined the two-dimensional antiferromagnet $KFeF_4$. The measurement of the spin-wave dispersion relation at two temperatures (50K and 100K) below the Néel temperature ($T_N$=136.75±0.25K), confirmed the description of $KFeF_4$ as a two-dimensional Heisenberg antiferromagnet with small Ising anisotropy. Studies of the magnetic phase transition in $KFeF_4$ revealed that below the Néel temperature, the critical behaviour is described by two-dimensional Ising models, and above a crossover to Heisenberg behaviour is seen. This crossover was detected by measuring the order parameter below $T_N$, and the static and dynamic susceptibilities above $T_N$ using neutron scattering techniques. The results were compared to power-law behaviour and also to theories for the classical Heisenberg antiferromagnet and the more recent quantum Heisenberg antiferromagnetic model. The final study of $KFeF_4$ involved an x-ray experiment on the structural phase transition around 400K. It has been suggested that there is a second-order transition at 410K to an incommensurate phase, which then undergoes a first-order lock-in transition at 400K to the low-temperature structure. This single crystal x-ray scattering study confirms the existence of the first-order phase transition, but shows no evidence for a higher temperature second-order transition or for the incommensurate phase.

# Scattering Studies of Excitations and Phase Transitions

## Table of Contents

# Acknowledgments

During the course of my thesis, I have had help and encouragement from many friends and colleagues and I would like to thank all of them here. I am especially grateful to my supervisor, Roger Cowley, for his guidance and advice throughout my time at Oxford. Thanks must also go to Steve Nagler, without whom my first experiment would not have been so fruitful, and also to Andrew Boothroyd for all his help with the copper oxide experiments. I also appreciate all the help given by Mark Harris and Jon Goff during the course of many x-ray experiments and also for their time reading the thesis. On that note, a special word of thanks must go to David Jehan for his tireless efforts with a red pen.

Publications arising from this work:

"A Deep Inelastic Neutron Scattering Study of Sodium": S.Fulton, R.A.Cowley, A.C.Evans: To be published in J.Phys.: Condens. Matter.

"Spin Waves in the Quasi Two-Dimensional Antiferromagnet $KFeF_4$": S.Fulton, S.E.Nagler, R.A.Cowley, L.M.Needham: Physica B180&181 225 (1992).

"Spin Waves and Temperature Dependent Behaviour In the Quasi Two-Dimensional Antiferromagnet $KFeF_4$": S.Fulton, S.E.Nagler, L.M.Needham, B.M.Wanklyn: To be published in J.Phys.: Condens. Matter.

"Static and Dynamic Critical Behaviour of the Two-Dimensional Heisenberg Antiferromagnet $KFeF_4$.": S.Fulton, R.A.Cowley, A.Desert, T.Mason: To be published in J.Phys.: Condens. Matter.

# Chapter 1

# Introduction

The bulk of the work in this thesis has been performed using neutron scattering techniques. These include time-of-flight neutron scattering at a pulsed source, as well as neutron triple-axis spectrometer experiments at reactor sources. An experiment involving x-rays has also been performed using a rotating anode triple-axis spectrometer which is similar in many ways to the neutron instruments. The details of a neutron triple-axis spectrometer are given in chapter 2, after a discussion of the scattering theory of neutrons from structural and magnetic processes. The properties of the neutron have also been compared and contrasted with those of x-ray and Raman photons, and the situations in which each of these techniques is useful is also discussed in chapter 2.

In chapter 3, the first of the "excitation" experiments is described. This experiment is different in many ways to the others reported here. It involves the high-energy neutrons (>500meV) available at a spallation source and uses time-of-flight techniques to collect the scattered neutrons. The experiment has been performed on polycrystalline sodium in the high-momentum limit where the impulse approximation is valid. In this regime the scattering of neutrons from condensed matter systems becomes incoherent and approaches the limit of free-atom scattering. This is often referred to as deep inelastic neutron scattering and can be used to determine the momentum distribution of the target system, which can then be compared to theoretical predictions. This type of experiment is very difficult to perform at a reactor source, where there is a limited flux of high-energy neutrons available. The study of sodium was undertaken to look for anharmonic effects in the momentum distribution which should increase with increasing temperature. The momentum distribution of sodium was thus measured at four temperatures: 30K, 100K, 200K, 300K, on the inverse geometry spectrometer EVS, at the Rutherford-Appleton's ISIS facility. EVS has been specially designed for deep inelastic neutron scattering experiments.

In chapter 4, the classical theory of magnetic excitations known as linear spin-wave theory is introduced before two experiments measuring the spin-wave dispersion relations in CuO (chapter 5) and $KFeF_4$ (chapter 6) are reported. Both of these experiments have been performed using triple-axis spectrometers at reactor sources. The CuO spin-wave dispersion relation was measured on the HB3 instrument at the Oak Ridge National Laboratory. This was performed to determine the quality of the samples grown at the Clarendon Laboratory and to help characterise the nature of CuO, whose bonding suggests it may be a candidate for a spin 1/2 chain antiferromagnet. These systems have attracted a great deal of interest lately, and shall be discussed in more detail in chapter 5. This experiment measured the spin excitations above and below the Néel temperature ($T_N$=240K) along the chain direction in CuO at energy transfers below 80meV. Results from a two-magnon Raman scattering study are also examined in this chapter. These aimed to measure the high energy zone-boundary excitations (~160meV) which could not be reached using thermal neutrons.

The spin-wave dispersion relation of $KFeF_4$ is described in chapter 6 and was measured using the IN3 instrument at the Institute Laue Langevin (I.L.L.). This study is complementary to the experiment on the magnetic phase transition in $KFeF_4$ detailed in chapter 8. The purpose of the dispersion relation experiment was to characterise fully the nature of the magnetic interactions in this layered system, so that the magnetic phase transition study could be better understood. The spin-wave dispersion relation was measured at two temperatures (50K and 100K) below the Néel temperature ($T_N$=136.75±025K), along different directions in reciprocal space, so that any directional differences in nearest-neighbour exchange interactions could be determined. A detailed temperature study of the anisotropy effect was also undertaken and this was compared with the temperature dependence of the order parameter below $T_N$.

Two phase transition studies have been performed on $KFeF_4$. The first as already mentioned, involves the magnetic phase transition around 137K. The second involves a structural phase transition at 400K and is described in chapter 9. Before the details of these studies, chapter 7 outlines some of the basics of the theories of phase transitions. This is applicable to both types of phase transition in $KFeF_4$. The magnetic phase transition in $KFeF_4$ has been measured using neutron scattering techniques. The order parameter below $T_N$ was

measured as part of the spin-wave dispersion study and is described in chapter 6. Above $T_N$, the HB3 instrument at the Risø National Laboratory was used to measure the static and dynamic correlation functions. The data have been compared to the conventional power-law behaviour indicative of a two-dimensional Ising system or a classical three-dimensional system, as well as to the more recent theories developed for two-dimensional Heisenberg systems. The details of the Heisenberg theories are given in chapter 8 and are also applicable to the undoped cuprate systems important in the study of high-temperature superconductivity.

The structural phase transition in $KFeF_4$ at 400K has raised much interest because of the possibility of an incommensurate phase in this region. An incommensurate structure is one in which the modulation in reciprocal space is not a rational fraction of the basic structure. So far, there has been no conclusive evidence for such a phase in $KFeF_4$, and there is still much conflict as to the nature of the structural phase transition. Chapter 9 describes a single-crystal x-ray scattering study performed at the Clarendon Laboratory to clear up some of the confusion surrounding this structural phase transition in $KFeF_4$.

# Chapter 2

# Scattering Theory

In this chapter, scattering theory is discussed in order that the experiments which are described in chapters 3-9 can be understood. In the first section 2.1, there is a brief review of those properties of neutrons, x-rays and light scattering which make them useful for studying materials. Then the general theory of the scattering processes is examined in section 2.2, and it is shown how this can be applied to the nuclear scattering of neutrons and to x-ray scattering in section 2.3. The magnetic neutron scattering cross-section is then described in section 2.4. In later chapters it will be shown how the scattering cross-sections developed here can be applied to specific situations. To finish off there is a general discussion of the triple-axis spectrometer in section 2.5. This the basis for most of the instruments used to perform experiments in this work.

## 2.1 Introduction

Before describing the scattering theory, a brief resumé is given of the properties of neutron, x-ray and of Raman scattering. The main technique used in this work was neutron scattering. This was used to probe the high-energy scattering from sodium, the magnetic excitations of CuO and $KFeF_4$, and the magnetic phase transition in $KFeF_4$. X-ray scattering has also been used to study the structural phase transition in $KFeF_4$, and some Raman scattering results have been analysed which probe the high-energy magnetic excitations in CuO and $KFeF_4$.

Neutron scattering techniques have proved to be very valuable tools in the field of solid state physics[2.1], [2.2], [2.3]. This is due to the unique properties of the neutron: zero charge, a mass, $m$, of 1.0087 atomic mass units, a spin of 1/2 and a magnetic moment, $\mu_n$, of -1.9132 nuclear magnetons. The zero charge means that the neutron only interacts weakly with matter and so is able to penetrate into the bulk of a material. The simple Born approximation can then be used to interpret the results, whereas x-ray and particularly

electron diffraction techniques are strongly affected by multiple scattering. The Born approximation is based on first-order perturbation theory[2.4] and is valid when the scattering amplitude from a system is small.

The mass of the neutron is such that the de Broglie wavelength is of the order of the interatomic spacing in condensed matter systems. The neutrons scattering from different atoms in a solid or liquid interfere with one another giving rise to information about the correlations between the atoms in a system. The energy of a neutron is given by

$$E=k_BT=\frac{h^2}{2m\lambda^2}=\frac{\hbar^2k^2}{2m}, \qquad \textbf{(2.1)}$$

so that a neutron in thermal equilibrium with a temperature T=300K has a wavelength of 1.8Å, and a kinetic energy of 25meV. The energies of the neutrons which can be obtained from reactor and spallation sources are of the same order of magnitude as that of many excitations in solids, liquids and gases. The energy transferred in a neutron scattering process is easily resolved, in contrast to energies in x-ray scattering. Neutrons are also useful because they can scatter from two different mechanisms in a system - magnetic and non-magnetic interactions. Magnetic neutron scattering occurs via the interaction of the neutrons with the unpaired electrons of magnetic ions, while non-magnetic neutron scattering is the result of neutron-nuclear interactions. Magnetic scattering is a consequence of the neutron having a magnetic moment, and thus it can be used to study the magnetic properties of a system allowing the magnetic structures and excitations, such as spin waves, to be measured.

**Table 2.1 Comparing the properties of neutrons with x-ray and Raman photons.**

| | Typical $\lambda$ (Å) | Typical $k=2\pi/\lambda$ ($Å^{-1}$) | Typical Energy (meV) |
|---|---|---|---|
| Thermal Neutrons | 1.8 | 3.5 | 25 |
| X-rays (Cu $K_\alpha$) | 1.54 | 4 | $7.5x10^6$ |
| Raman | 5000 | 0.0002 | 400 |

X-rays from a Cu $K_\alpha$ source have similar wavelengths to thermal neutrons, but have energies which are of order $10^6$ times larger (see table 2.1)

$$E=\frac{hc}{\lambda}=\hbar ck. \tag{2.2}$$

The change in the energy of the x-rays when they scatter from the excitations in condensed matter systems is too small to measure accurately at present. However x-rays have an advantage over neutrons for determining chemical structures because the sources generally have higher intensity and the instruments better resolution than neutron facilities. X-ray scattering occurs from the interaction of the x-rays with the electrons of an atom[2.5]. This means that the scattering amplitude increases with the atomic number of the scattering system. This is not the case with neutron scattering, where the scattering by the nucleus is a complex nuclear property and varies for different isotopes and for neighbouring elements.

Raman scattering[2.6] is the inelastic scattering of laser light, and unlike x-rays and neutrons, the wavevector, k, is much smaller than typical reciprocal lattice vectors and so only small wavevector transfers, **Q**, can occur (see table 2.1). It thus probes excitations with **Q**~0. It does however allow access to high-energy excitations which occur in solids, with the energy of a typical light source of order 400meV. Furthermore, laser sources are very intense, but coupling between the light and the excitations is much more complex than for neutron and x-ray scattering.

In the following sections the theory for neutron scattering experiments is described. For more details on the nature of x-ray scattering see reference [2.5], while Raman scattering is discussed in detail in reference [2.6].

## 2.2 The Scattering Cross-Section

During an experiment, the neutrons interact with the scattering system and the scattered neutrons provide information about the properties of the sample being studied. While scattered by a sample, the neutron may have its energy, momentum and spin state changed. If the neutron has an initial momentum $\hbar\mathbf{k}_i$, and momentum $\hbar\mathbf{k}_f$ after the scattering process, the

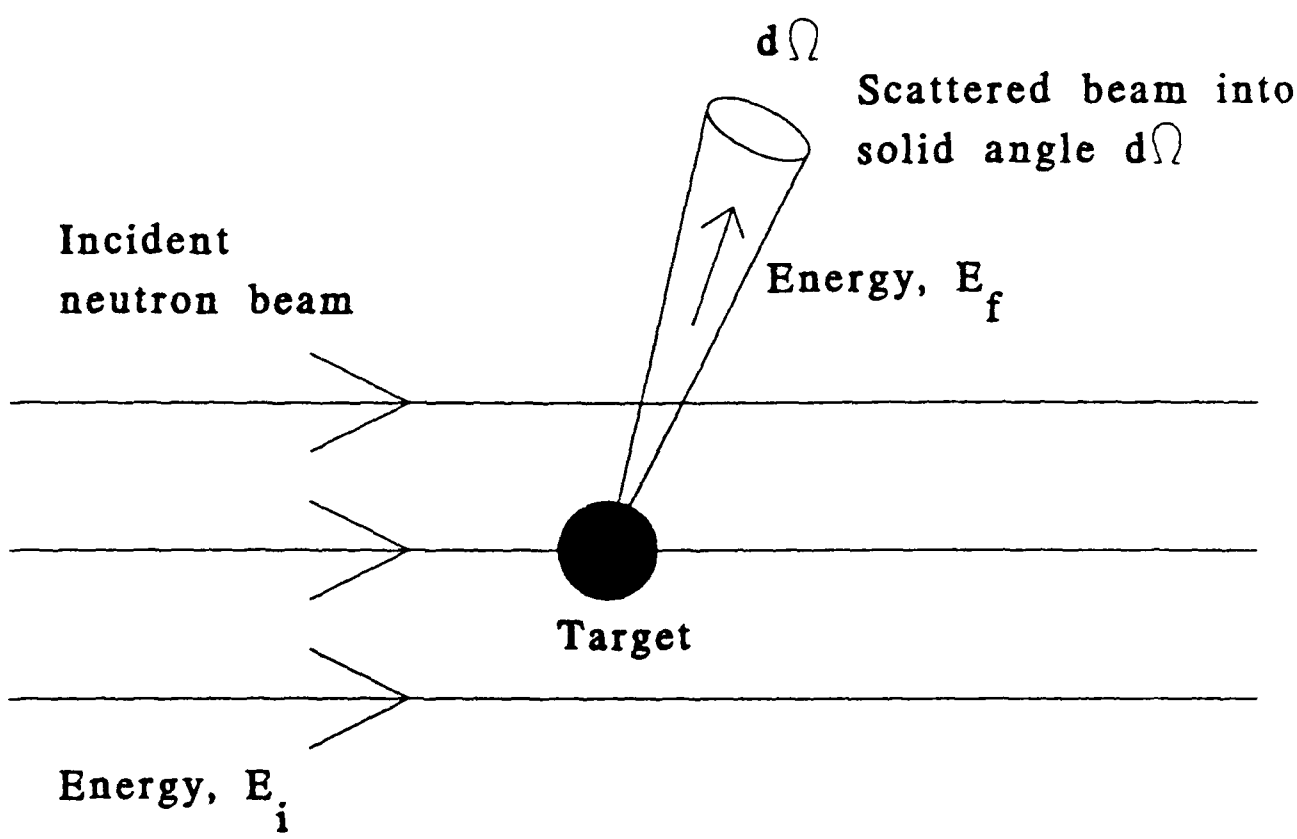


Figure 2.1: The scattering of a neutron beam by a small target into a solid angle $d\Omega$.

momentum transfer to the system is

$$\hbar Q=\hbar k_i-\hbar k_f. \tag{2.3}$$

In the same way, if the neutron's initial energy is $E_i$, and the scattered energy is $E_f$, the energy transfer to the system is defined by

$$E=\hbar\omega=E_i-E_f=\frac{\hbar^2}{2m}(k_i^2-k_f^2). \tag{2.4}$$

The intensity of the scattering associated with the momentum and energy transfers is a measure of a property of the system known as the scattering cross-section. Figure 2.1 shows a schematic sketch of a scattering process. The cross-section, $\sigma$, is the quantity which is measured in any scattering experiment. By detecting the neutrons scattered in a solid angle $d\Omega$, the differential cross-section, $d\sigma/d\Omega$, is measured. Furthermore, if only neutrons in a energy range $dE_f$ are measured, the partial differential cross-section is obtained, $d^2\sigma/d\Omega dE_f$. The master formula for the partial differential cross-section is written as

$$\left(\frac{d^2\sigma}{d\Omega dE_f}\right)_{\lambda_i\to\lambda_f}=\frac{k_f}{k_i}\left(\frac{m}{2\pi\hbar^2}\right)^2\sum_{\lambda_i,\sigma_i}p_{\lambda_i}p_{\sigma_i}\sum_{\lambda_f,\sigma_f}|\langle k_f\sigma_f\lambda_f|V|k_i\sigma_i\lambda_i\rangle|^2\delta(E+E_{\lambda_i}-E_{\lambda_f}) \tag{2.5}$$

as shown in Squires[2.1] equation 2.16. This equation provides the basis for the interpretation of all neutron scattering experiments. It represents the probability that the system will make a transition from a state $\lambda_i$ to $\lambda_f$ when a neutron is scattered from the system. $\lambda_i$ and $\lambda_f$ represent the initial and final state of the scattering system, with energies $E_{\lambda i}$ and $E_{\lambda f}$ respectively. $\sigma_i$ and $\sigma_f$ are the initial and final spin states of the neutron. The probability that the system is in an initial state $\lambda_i$ is written as $p_{\lambda i}$, and $p_{\sigma i}$ is the probability of the initial neutron spin state. The spin state of the neutron must be taken into account when performing polarization analysis experiments. The matrix element $|\langle k_f\sigma_f\lambda_f|V|k_i\sigma_i\lambda_i\rangle|^2$ arises from Fermi's Golden rule[2.4] for the probability of a transition from an initial to a final state with a perturbation $V$. Here the neutron changes state from $|k_i\sigma_i\rangle$ to $|k_f\sigma_f\rangle$ as a result of an interaction potential, $V$, between the system and the neutron, while the system changes from $|\lambda_i\rangle$ to $|\lambda_f\rangle$. The $\delta(E+E_{\lambda i}-E_{\lambda f})$ term represents the fact that energy must be conserved during

the scattering process, i.e. any gains or losses of energy by the neutron, must be taken up by the scattering system (equation 2.4). Notice the term $k_f/k_i$ which makes it desirable to have initial and scattered wavevectors of comparable magnitudes for strong scattering.

## 2.3 Nuclear Scattering

In this section the simplest type of scattering of neutrons is considered, this involves only the short-range forces arising from the nuclear interactions between the nuclei of the sample and the neutron. The more complicated case of magnetic scattering will be treated in section 2.4.

The form of scattering by the nuclear interactions is determined by the interaction potential, $V$. Nuclear interactions arise from the strong nuclear forces and have a small spatial extent, three orders of magnitude smaller than the de Broglie wavelength of the thermal neutron. Fermi showed that the scattering was isotropic and that the potential could be approximated by a delta function form known as the Fermi pseudo-potential[2.1], [2.2],

$$V_j=\frac{2\pi\hbar}{m}b_j\delta(\boldsymbol{r}-\boldsymbol{R}_j), \tag{2.6}$$

where $\boldsymbol{R}_j$ is the position of the nucleus of the jth atom in the sample, and $\boldsymbol{r}$ is the position of the neutron. Here, $b_j$ is the appropriate scattering length of the atom, which in general is different not only for the different types of atoms, but for each isotope and for the relative orientations of the neutron and nuclear spins.

This interaction potential can be used to calculate the matrix elements required for evaluation of the partial differential cross-section (equation 2.5). In the Born approximation the wavefunction for the incident neutron has the form $\exp(i\mathbf{k}_i.\mathbf{r})$ and that of the scattered neutron is $\exp(i\mathbf{k}_f.\mathbf{r})$, so that

$$\langle k_f|V_j|k_i\rangle=\frac{2\pi\hbar}{m}b_j\int e^{-i\boldsymbol{k}_f\cdot\boldsymbol{r}}\delta(\boldsymbol{r}-\boldsymbol{R}_j)e^{i\boldsymbol{k}_i\cdot\boldsymbol{r}}dr=\frac{2\pi\hbar}{m}b_j e^{i\boldsymbol{Q}.\boldsymbol{R}_j}, \tag{2.7}$$

where $\mathbf{Q}$, the wavevector transfer, is given by equation 2.3. Substituting equation 2.7 into

equation 2.5 and neglecting the polarisation of the neutron beam gives

$$\left(\frac{d^2\sigma}{d\Omega dE_f}\right)_{\lambda_i\to\lambda_f} = \frac{1}{N}\frac{k_f}{k_i}\sum_{\lambda_i} p_{\lambda_i}\sum_{\lambda_f} |\Sigma_j b_j\langle\lambda_f|e^{iQ.R_j}|\lambda_i\rangle|^2\delta(E+E_{\lambda_i}-E_{\lambda_f}), \qquad \textbf{(2.8)}$$

which is true for all nuclear scattering processes. The properties of a system are contained in the eigenstates $|\lambda\rangle$.

### 2.3.1 The Van Hove Formalism

By introducing an integral representation for the delta function in equation 2.8, and by summing over the final states of the system, and averaging the initial states, the partial differential cross-section can be written

$$\frac{d^2\sigma}{d\Omega dE_f} = \frac{k_f}{k_i}\frac{1}{2\pi\hbar}\Sigma_{j',j} b_j b_{j'}\int\langle e^{\{-iQ.R_{j'}(0)\}}e^{\{iQ.R_j(t)\}}\rangle \times e^{(-i\omega t)}dt. \qquad \textbf{(2.9)}$$

Here $\boldsymbol{R}_j(t)$ is the time-dependent Heisenberg operator of the position of the $j^{th}$ ion in the scattering system (see appendix D in reference [2.1]). Equation 2.9 shows that the cross-section is proportional to the time Fourier transform of the correlation function of the position vectors of the ions in the scattering system.

Equation 2.9 can be split into two parts corresponding to coherent and incoherent scattering. For a monatomic system this is

$$\frac{d^2\sigma}{d\Omega dE_f} = \frac{\sigma_{coh}}{4\pi}\frac{k_f}{k_i}NS(\boldsymbol{Q},\omega) + \frac{\sigma_{incoh}}{4\pi}\frac{k_f}{k_i}NS_i(\boldsymbol{Q},\omega) \qquad \textbf{(2.10)}$$

where N is the number of ions in the system, with

$$\sigma_{coh} = 4\pi(\overline{b})^2 \qquad \textbf{(2.11)}$$

and

$$\sigma_{incoh}=4\pi(\overline{b^2}-(\overline{b})^2). \tag{2.12}$$

The first term in equation 2.10 is the coherent scattering and arises from the interference of the scattering from the different atoms and so depends on the average scattering. $S(\mathbf{Q},\omega)$ is known as the van Hove scattering function and is related by double Fourier transforms to the time-dependent total pair correlation function[2.2]. This is the scattering which would arise if all the atoms in the system had the same scattering length *b*. The incoherent scattering is proportional to the mean square deviation of the scattering length and so is due to the correlations between the positions of the same nucleus at different times. $S_i(\mathbf{Q},\omega)$ is the incoherent scattering function and is the time-dependent self correlation function. This scattering is isotropic and gives rise to a flat background[2.7].

Concentrating on the coherent scattering, it is this contribution which leads to Bragg peaks and phonon scattering. By splitting the coherent scattering function into time-dependent and time independent parts, $S(\mathbf{Q},\omega)$ can be written as

$$S(\mathbf{Q},\omega)=S^{B}(\mathbf{Q})+S^{Inel}(\mathbf{Q},\omega). \tag{2.13}$$

$S^{B}(\mathbf{Q})$ represents the Bragg scattering from the system and has the following form

$$S^{B}(\mathbf{Q})=\frac{(2\pi)^3}{v}\Sigma_{\tau}|F_N(\mathbf{Q})|^2\delta(\mathbf{Q}-\tau). \tag{2.14}$$

This function leads to peaks in the scattering when the wavevector transfer **Q** is equal to a lattice reciprocal lattice vector, τ. The volume of the unit cell of the crystal lattice is given by *v*, while $F_N(Q)$ is the scattering amplitude of the scattering function and is known as the unit-cell structure factor. It has the following form for a non-Bravais crystal

$$F_N(\mathbf{Q})=\Sigma_d \overline{b}_d e^{(i\mathbf{Q}.d)}e^{(-W_d)}, \tag{2.15}$$

where *d* is the position of the ion within the unit cell. The $\exp(-W_d)$ term is the Debye-Waller factor and gives a reduction of the amplitude of the scattering due to the thermal motion of the ions in the scattering system. The other term, $S^{inel}(\mathbf{Q},\omega)$, in equation 2.13 gives rise inelastic scattering. It shall not be discussed further except in chapter 3 where the inelastic

scattering from sodium in the impulse approximation will be discussed.

Note that the form of the Bragg scattering given in equation 2.14 is also valid for x-ray scattering, except that the neutron scattering length, $b$, is replaced by the x-ray scattering length also known as the atomic scattering factor[2.7]. This is Q dependent and decreases to zero for short wavelength radiation scattered through a large angle. Thus is not the case for neutron scattering length, which is wavelength and angle independent.

## 2.4 Magnetic Scattering

In this section, the master formula (equation 2.5) for the partial differential cross-section is used to obtain the scattering arising from magnetic interactions between the neutrons and the sample. Magnetic scattering is due to the interaction of the neutron with the unpaired electrons in the scattering system. For an electron, the magnetic interaction potential has the following form

$$V_M = -\boldsymbol{\mu}_n . \boldsymbol{B}, \tag{2.16}$$

where $\boldsymbol{B}$ is the magnetic field produced by an electron in the sample and has spin and orbital contributions. The operator corresponding to the magnetic dipole moment is $\boldsymbol{\mu}_n$ and is given by

$$\boldsymbol{\mu}_n = -\gamma \mu_N \sigma. \tag{2.17}$$

$\mu_N$ is the nuclear magneton, $\gamma$=1.913 is a constant, and $\sigma$ is the Pauli spin operator for the neutron. The local magnetic field **B** arising from the spin of an electron is given by[2.1], [2.2]

$$\boldsymbol{B} = \frac{\mu_0}{4\pi} \left[ curl \left( \frac{\boldsymbol{\mu}_e \times \boldsymbol{R}}{|\boldsymbol{R}|^3} \right) \right], \tag{2.18}$$

where the electron at position **R** has a magnetic moment $\boldsymbol{\mu}_e$ arising from its spin. $\boldsymbol{\mu}_e$ is the electron magnetic dipole moment operator, and is defined in a similar way to that for the neutron (equation 2.17)

$$\boldsymbol{\mu}_e = -2\mu_B \mathbf{s}, \tag{2.19}$$

with **s** being the spin operator for the electron. If the scattering arises from a crystal in which the electrons are localised about the ions in the lattice, the model can be simplified. This is the case in insulating salts, such as $KFeF_4$ where the model can be restricted to ions with zero total angular orbital momentum, ie L=0, such is the case for the $Fe^{3+}$ ion.

The cross-section for an unpolarised experiment from a sample with a Bravais lattice and only spin contributions to the magnetic scattering can then be written as[2.1], [2.2]

$$\begin{aligned}\frac{d^2\sigma}{d\Omega dE_1} = (\gamma r_o)^2 \frac{k_f}{k_i} \sum_{\alpha\beta} (\delta_{\alpha\beta} - \hat{Q}_\alpha \hat{Q}_\beta) \sum_l \sum_j F(Q)^2 \\ \times \sum_{\lambda_i \lambda_f} p_\lambda \langle \lambda_i | e^{(-iQ.R_l)} S^\alpha{}_l | \lambda_f \rangle \\ \times \sum_{\lambda_i \lambda_f} p_\lambda \langle \lambda_i | e^{(iQ.R_j)} S^\beta{}_j | \lambda_f \rangle \delta(\hbar\omega + E_{\lambda_f} - E_{\lambda_i}).\end{aligned} \tag{2.20}$$

$\gamma r_o$=5.39fm is analogous to the nuclear scattering length, *b*, with a similar magnitude. $F(\mathbf{Q})$ is the magnetic form factor of the magnetic ions, and is **Q** dependent. $\boldsymbol{R}_l$ is the position of the magnetic ion with *l* denoting the unit cell. $S^\alpha{}_l$ is the spin vector of the $l^{th}$ ion, and has replaced the single electron spin vector, **s**. The unit vectors in the direction of the scattering **Q** have been used, and $\alpha$ and $\beta$ are sums over the cartesian coordinates *x,y,z*. $\delta_{\alpha\beta}$ is the Kronecker delta such that $\delta_{\alpha\beta}$=1 only if $\alpha$=$\beta$, and means that there is only magnetic scattering from spin components perpendicular to the scattering vector **Q**.

This can be written in a more concise and useful form as described by Van Hove[2.8] in terms of correlation functions, by replacing the delta function with its integral representation, and by introducing the time-dependent Heisenberg operators of the spin operators. This gives the magnetic scattering as

$$\frac{d^2\sigma}{d\Omega dE_f} = \frac{k_f}{k_i} \frac{N}{\hbar} (\gamma r_o)^2 |F(Q)|^2 \sum_{\alpha\beta} (\delta_{\alpha\beta} - \hat{Q}_\alpha \hat{Q}_\beta) S^{\alpha\beta}(Q,\omega) \tag{2.21}$$

where

$$S^{\alpha\beta}(Q,\omega)=\frac{1}{2\pi N}\sum_{jl} e^{iQ.(R_j-R_l)}\int e^{-i\omega\tau}\langle S^{\alpha}{}_{l}(0)S^{\beta}{}_{j}(t)\rangle dt. \qquad (2.22)$$

$S^{\alpha\beta}(\mathbf{Q},\omega)$ is the temporal Fourier transform of the correlation function between the spin vectors, **S**, of the $l^{th}$ ion along the direction $\alpha$ at zero time, with the $j^{th}$ ion along direction $\beta$ at time $t$. In most materials the symmetry is sufficiently high that the correlation functions are zero unless $\alpha=\beta$. This can be split into long and short range time correlations as was done for the structural scattering in section 2.3.1. The long time correlations, $t\rightarrow\infty$, give rise to the magnetic Bragg scattering, which decreases with increasing temperature, as the magnetic order decreases. In a simple antiferromagnetic system the intensity of a magnetic Bragg peak is proportional to the square of the staggered magnetisation. The short-time correlations, representing the inelastic scattering, can be described in terms of the susceptibility. $S^{\alpha\beta}(\mathbf{Q},\omega)$ is thus written schematically, dropping the $\alpha$ and $\beta$ and suffixes, as[2.9]

$$S^{\alpha\beta}(Q,\omega)=[S_B(Q)+S_D(Q,\omega)], \qquad (2.23)$$

where

$$S_B(Q)=NM^2\sum_{\tau}\delta(Q-q_s-\tau)\delta(E) \qquad (2.24)$$

and

$$S_D(Q,\omega)=[n(\omega)+1]\chi(Q)F(Q,\omega)\sum_{\tau}\delta(Q-q-\tau). \qquad (2.25)$$

$S_B(\mathbf{Q})$ is the elastic scattering from a magnetic system, ie the magnetic Bragg peaks from an ordered system, and is proportional to the square of the staggered magnetisation in an antiferromagnetic system (where $M=\langle S\rangle$). $S_D(\mathbf{Q},\omega)$ represents the inelastic part of the magnetic scattering and arises from short-time correlations between the spin fluctuations. In equation 2.25, **q** represents the wavevector of the magnetic excitation. In the low temperature limit equation 2.25 describes how the spin waves in the scattering system interact with the neutrons. This will be discussed in chapter 4. Close to $T_N$ it gives a measure of the critical fluctuations as the magnetic phase transition is approached. $\chi(\mathbf{Q})$ is the wave-vector dependent static susceptibility and $F(\mathbf{Q},\omega)$ is known as the spectral weight function. The form of these functions will be discussed in chapter 7.

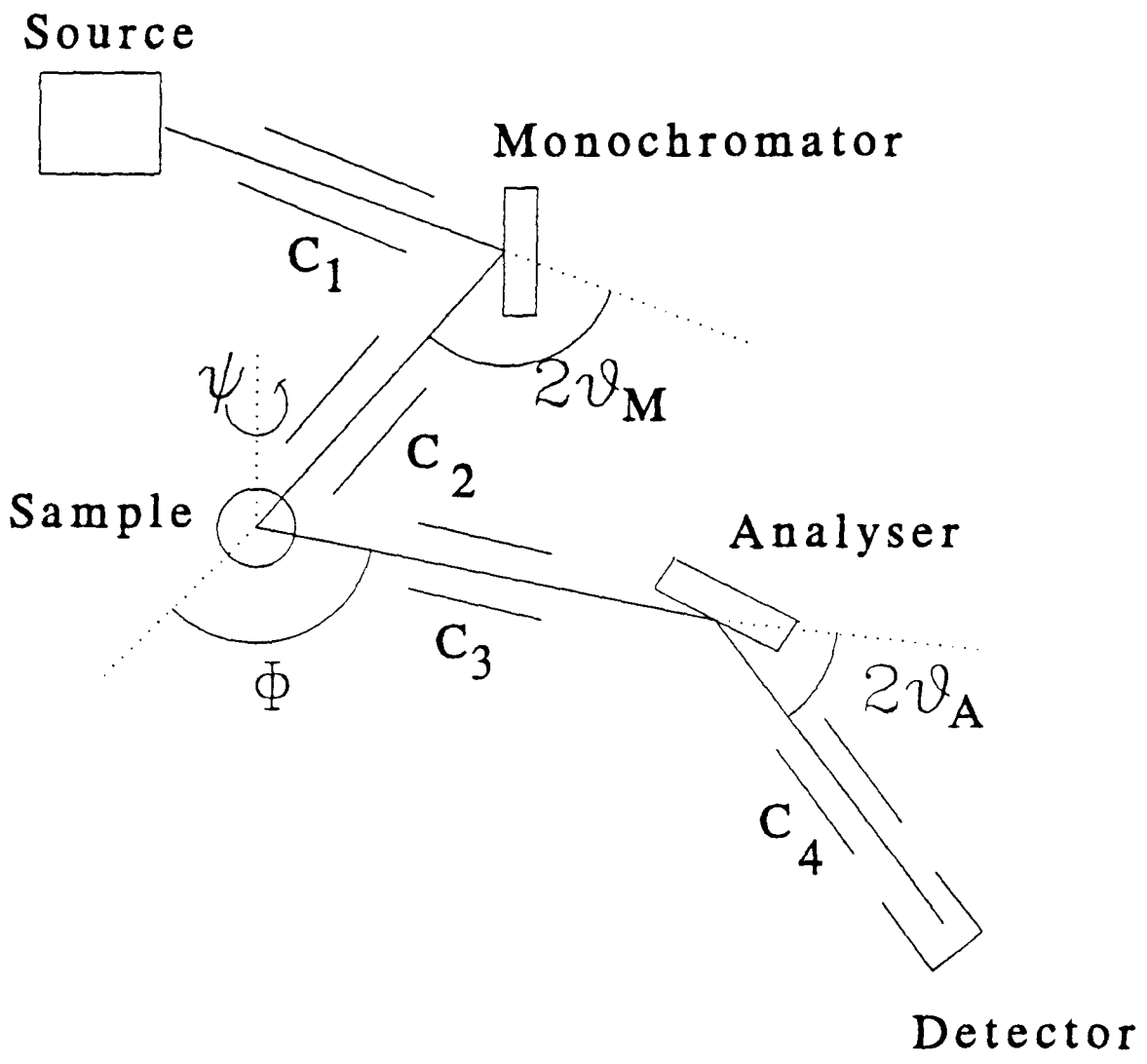


Figure 2.2: Schematic diagram of a triple-axis spectrometer.

## 2.5 The Triple-Axis Spectrometer

It will be useful, before discussing the experiments, to describe the main instrument used to measure the neutron scattering function: the triple-axis spectrometer (TAS)[2.10]. This type of instrument has been used to measure the spin-wave dispersion relation in CuO and $KFeF_4$, and is the basis for the x-ray triple-axis spectrometer used in chapter 9 for the phase transition study of $KFeF_4$. The only experiment which does not use a variation of a TAS instrument is the study of the recoil scattering in sodium described in the next chapter. This experiment was carried out on an indirect-geometry spectrometer at a spallation source, and shall be described in detail in chapter 3.

The triple-axis spectrometer is a very versatile and valuable tool for measuring the scattering cross-sections from single-crystal samples. The sources of neutrons for these instruments are nuclear reactors which produce a continuous flux of neutrons with a Maxwellian energy distribution, the peak energy being determined by the moderator temperature. The TAS is so called because it has three axes of rotation: the one around which the monochromator crystal rotates, the axis of rotation of the sample and finally that of the analyser crystal. The components of a TAS instrument are shown in figure 2.2.

To define the initial energy, $E_i$, of the neutrons reaching the sample, Bragg scattering from the monochromator crystal is used, with the analyser crystal defining the detected scattered energy, $E_f$, from the sample. Monochromator and analyser crystals are made from large single crystals, typically pyrolytic graphite or copper. The energies, and thus wavelengths of the neutrons required, are selected from the monochromator crystal using Braggs law:

$$\lambda = 2d_M \sin\theta_M. \qquad \textbf{(2.26)}$$

In this equation $d_M$ is the plane spacing of the monochromator crystal, and $\theta_M$ is the Bragg angle as marked in figure 2.3, and is half the angle between the incident and scattered beam. This can also be applied to the analyser crystal, by replacing the monochromator spacing and scattering angle by the appropriate analyser values. The wavevector transfer, **Q**, to the sample is defined by the magnitude of the wavevectors of the incident and scattered neutrons and also

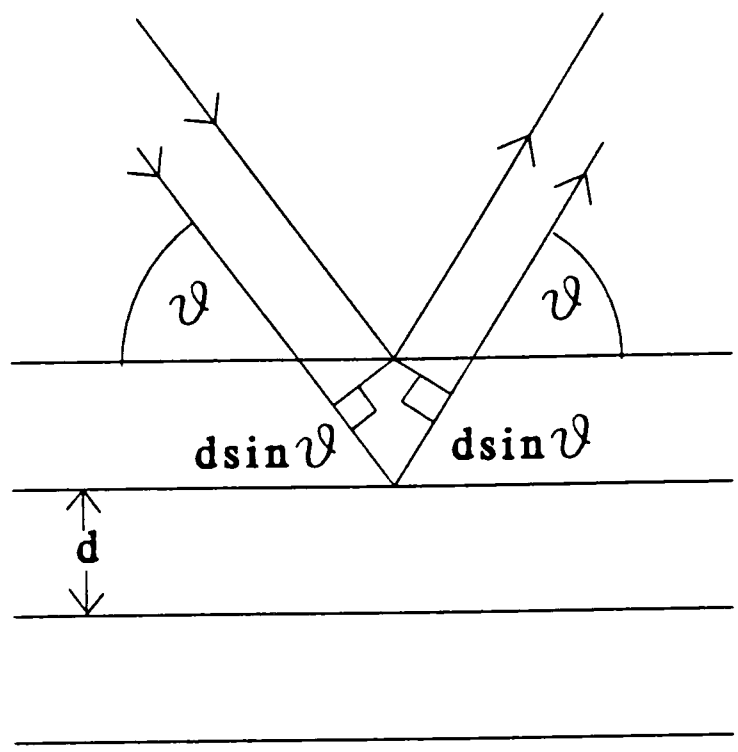


Figure 2.3: A Bragg reflection from planes separated by d.

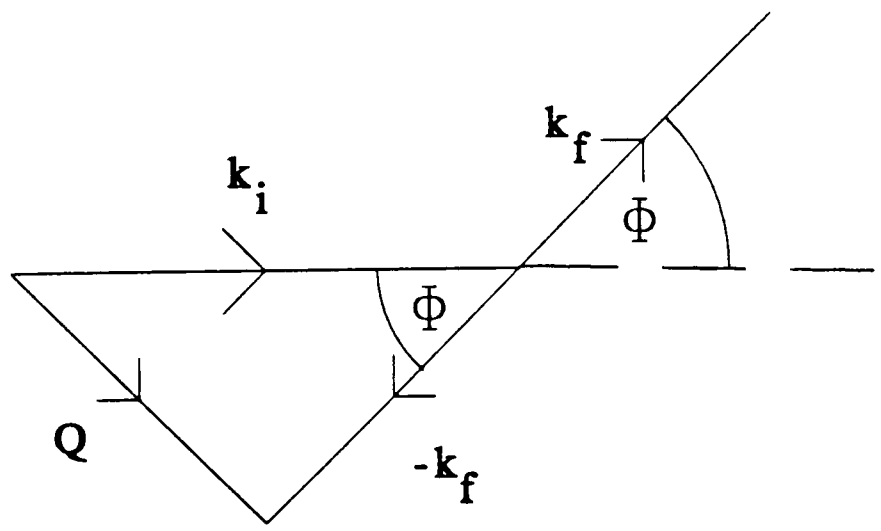


Figure 2.4: The scattering triangle for a wavevector transfer Q.

by the scattering angle $\Phi$ (as shown in figure 2.4)

$$Q=(k_i^2+k_f^2-2k_ik_f\cos\Phi). \tag{2.27}$$

Thus, knowing the incident and final energy of the scattered neutron, the energy transfer to the system can be determined. If the scattering angle $\Phi$ is also known then the wavevector transfer, **Q**, can be determined. When the energy transfer is zero, the scattering is elastic. In this situation, and in the more general case where the energy transfer is finite but held constant, if a scan is performed in which the wavevector transfer is allowed to vary, this is called a constant-energy scan. If on the other hand, the wavevector transfer, **Q**, is held constant while the energy transfer is allowed to vary, this is known as a constant-Q scan.

During a scattering experiment it is often desirable to use a neutron filter either before or after the sample to reduce the contamination from higher-order wavelengths that are allowed by the monochromator. These filters are of two main types: beryllium and pyrolytic graphite. The pyrolytic graphite filter is optimum in a narrow band of energies around 14meV. This is because at twice this energy, the filter has essentially zero transmission and thus there are few $\lambda/2$ wavelength neutrons present in the beam. The zero transmission arises at these energies (around 56meV) because, the incident wavelength satisfies the Bragg condition for $2\theta_M=180°$, and thus most of the incident beam is reflected. The beryllium filters operate at energies less than 5.2meV. The beryllium filter is polycrystalline and allows the passage of low-energy neutrons with wavelengths greater than the Bragg cut-off.

To define the neutron path and to reduce the angular spread of the beam, collimators are used[2.10]. These are usually of the Soller slit variety, as these define the beam without too much attenuation. They tend to be variable, the angular divergence depending on the resolution requirements of the experiment. More slits are added to decrease the angular spread, the angle $\alpha$, being defined by the following equation

$$\alpha=\frac{W}{L}, \tag{2.28}$$

where W is the separation of the slits of length L. The slits are sometimes made from mylar coated with gadolinium or cadmium, and typical angular spreads for neutron work are 10′-

120′ depending on the requirements of the experiment- high intensity requires large collimation angles, good resolution requires small collimation angles. The resolution function of a TAS instrument shall be discussed in more detail in chapter 5. TAS instruments usually have four collimators, and these are shown in figure 2.2. $C_1$ is the pre-monochromator collimation, and is defined by the neutron guide tube. This usually has a horizontal divergence $H_1$=20′ and is energy dependent. This collimation plays an important role in determining the resolution function of an instrument. The collimator $C_2$ is placed between the monochromator and the sample, and $C_3$ is the sample to analyser collimator. These can normally be varied, and their angular divergence is determined by the resolution requirements of the particular experiment. $C_4$ is the pre-detector collimator and is found not to play an important role in the resolution of the instrument, but helps to cut down on background neutrons entering the detector.

To detect the neutrons $^3$He detectors are used. These have the advantage of being efficient for slow neutrons, and at the same time having a low efficiency for γ-rays and fast neutrons, thus reducing background effects. These detect neutrons using the following reaction

$$n+{}^3He \rightarrow {}^3H+p+0.77MeV. \qquad \textbf{(2.29)}$$

Thus the neutron produces a γ-ray which is easily detected from the ionisation of the gas.

## References


[2.1].G.L.Squires: "Introduction to the Theory of Thermal Neutron Scattering" (Cambridge University Press, 1978).

[2.2].W.Marshall, S.W.Lovesey: "Theory of Thermal Neutron Scattering" (Oxford University Press, 1971).

[2.3].D.L.Price, K.Skold: Methods of Experimental Physics 23A 1 (1986).

[2.4].A.I.M.Rae: "Quantum Mechanics" (Adam Hilger, 2nd edition, 1986).

[2.5].D.M.McKie, C.McKie: "Crystalline Solids" (Thomas Nelson & Sons Ltd, 1974).

[2.6]. W.Hayes, R.Loudon: "Scattering of Light by Crystals" (John Wiley & Sons, 1978).

[2.7].W.Cochran: "The Dynamics of Atoms in Crystals" (Edward Arnold, 1973).

[2.8].L.Van Hove: Phys. Rev. 95, 1374 (1954).

[2.9].R.A.Cowley: Methods of Experimental Physics 23C 1 (1987).

[2.10].C.G.Windsor: Methods of Experimental Physics 23A 197 (1986).
C.G.Windsor: Neutron Scattering at a Pulsed Source, Chapter 7 (Edited by R.J.Newport, B.D.Rainford, R.Cywinski; IOP Publishing Ltd., 1988).

# Chapter 3

# A Deep Inelastic Neutron Scattering Study of Sodium

In this chapter the first of the "excitation" experiments is described. This experiment, on polycrystalline sodium, was performed at a spallation neutron source in the high-momentum transfer limit known as the impulse approximation. This technique measures the momentum distribution of the scattering system, which can be compared with the theoretical predictions. Section 3.1 discusses some of the previous work carried out using the impulse approximation, and the advantages of spallation sources for these experiments. In section 3.2 there is a brief overview of the scattering theory required, with an introduction to an analysis technique for recoil scattering known as y-scaling. The details of the EVS time-of-flight instrument are described in section 3.3, and this includes a discussion of the resolution function for the instrument. The validity of the impulse approximation for this experiment on sodium is shown in section 3.4, before a comparison of the results for the momentum distribution is made with the theory for an isotropic harmonic solid.

## 3.1 Introduction

Spallation sources produce an abundance of neutrons with energies in the 1-50eV region of the spectrum, and these allow a direct determination of atomic momentum distributions by use of a technique known as deep inelastic neutron scattering (DINS). This technique requires high energy and momentum transfers in order that the impulse approximation can be used to interpret the scattering data. The first studies using the impulse approximation were made on liquid $^4$He[3.1], [3.2], [3.3] following the proposal made by Hohenberg and Platzman[3.4] that it enabled the proportion of atoms in the zero-momentum superfluid state to be determined. The development of spallation sources with high-energy neutron intensities - two orders of magnitude larger than those from reactor sources in the 1-50ev

region - has now made it possible to make similar measurements on light atoms in crystals[3.5], [3.6].

At the Rutherford Appleton Laboratory's ISIS facility the inverse geometry spectrometer EVS has been developed for work in the high-energy regime required to analyse impulsive recoil scattering. The purpose of this experiment on sodium was to study the temperature dependence of the atomic momentum distribution and to compare the results with calculations based on the harmonic approximation and the known density of phonon states[3.7]. When this comparison was made in solid helium[3.8], the widths observed were 15% larger than those calculated and the difference was attributed to anharmonic effects in the phonon momentum distribution, and thus the calculations based on the harmonic theory were inadequate. A similar comparison has been made in the case of beryllium[3.5] and lithium[3.9] on the HET instrument at ISIS, and in these experiments the widths were 6% and 12% larger than theory. However, more recently the momentum distribution obtained for lithium on EVS showed that the results were only 2% larger than those expected for an isotropic harmonic solid[3.10]. It seems therefore that the harmonic approximation for the atomic momentum distribution is affected by anharmonicity. In sodium[3.11] these effects are expected to be large at high temperatures, and a comparison between the measured width and the calculated width should provide further information about the effects of anharmonicity and the validity of interpreting the impulse approximation in terms of the harmonic model.

## 3.2 The Impulse Approximation

It is found that the scattering function for a single free particle can be applied to a real sample of identical atoms, assuming that the impulse approximation is valid. The impulse approximation assumes that the neutron has an incident energy much larger than any collective excitations in the system (such as phonons) and thus the neutron probes the properties of the individual particles. The impulse approximation is valid in the high-Q limit and takes into account only short-time properties of the sample. In the following section, the scattering function for a single particle will be evaluated, and it will be shown how this can be applied to a real system of particles. Section 3.2.2 then deals with an analysis technique

known as y-scaling. This removes the Q-dependence of the scattering and means that the results from different detectors on EVS can be averaged together.

### 3.2.1 The Single Particle Scattering Function

Now the theory is developed for a single free particle[3.12]. A single atom has a partial differential cross section of the following form

$$\frac{d^2\sigma}{d\Omega dE_f} = \frac{k_f}{k_i} b^2 S(\boldsymbol{Q},\omega), \tag{3.1}$$

where $S(\mathbf{Q},\omega)$ is known as the scattering function and $b$ is the scattering length of the atom. From equation 2.8 it is seen that the scattering function can be written as

$$S(\boldsymbol{Q},\omega) = \sum_{\lambda_i} p_{\lambda_i} \sum_{\lambda_f} |\langle \lambda_f | e^{i\boldsymbol{Q}.\boldsymbol{R}} | \lambda_i \rangle|^2 \delta(\hbar\omega + E_{\lambda_i} - E_{\lambda_f}). \tag{3.2}$$

If the wavefunction for a particle in a box is written in the form $\exp(i\mathbf{p}.\mathbf{R})$, the $\langle \ | \ | \ \rangle$ term integrates to zero unless

$$\boldsymbol{Q} + (\boldsymbol{p}_i - \boldsymbol{p}_f) = 0. \tag{3.3}$$

When this condition is true the matrix element equals unity, and this gives the scattering function as

$$S(\boldsymbol{Q},\omega) = \sum_{p_i} n_f(p_i) \delta\left(\hbar\omega - \frac{\hbar^2 Q^2}{2M} - \frac{\hbar^2 \boldsymbol{Q}.\boldsymbol{p}_i}{M}\right), \tag{3.4}$$

where $n_f(p_i)$ is the momentum distribution for the initial state of a free particle. Equation 3.4 represents the scattering from a particle with recoil energy $\hbar^2Q^2/2M$, since the average of $\hbar^2\mathbf{Q}.\mathbf{p}_i$ is zero. In this equation $\hbar\mathbf{p}_i$ is the initial momentum of an atom in the target system, $\hbar\mathbf{Q}$ is the momentum transferred from the neutron to the particle, $\hbar\omega$ is the energy transfer and M is the atomic mass of the scattering system.

The impulse approximation assumes that when an atom in a system is struck by high

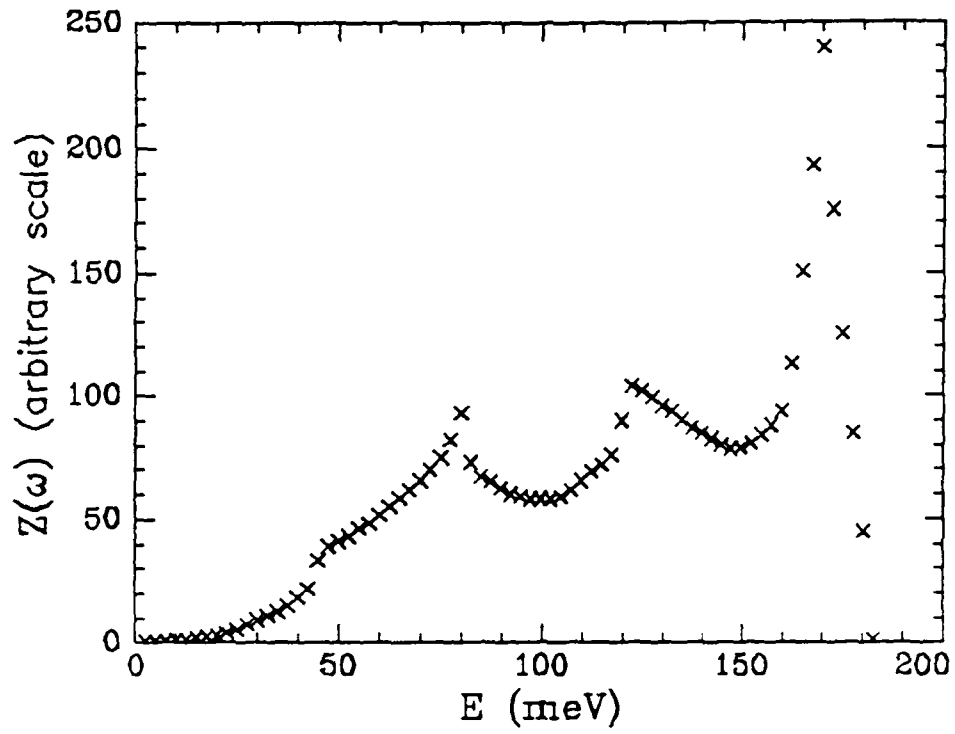


**Figure 3.1: The density of phonon states for sodium, as calculated by Woods et al[3.10].**

energy neutrons, the scattering atom recoils freely and the effects of interatomic collisions can be neglected[3.13]. Then equation 3.4 can be used to represent the scattering from a real system with a momentum distribution *n(p)*. For any solid, the impulse approximation is valid asymptotically at high wavevector transfers[3.14]. In this region the wavelength of the neutron is much smaller than the interatomic spacing and thus interference cannot occur, and the scattering is from individual particles in the system. Here the coherent scattering is behaving like incoherent scattering. For an isotropic harmonic system the atomic momentum distribution is identical to that for an ideal gas, except that the temperature T is replaced by $T^*$ - an effective temperature[3.15] which takes into account the environment of an atom. Thus *n(p)* is given by

$$n(p)=\left(\frac{1}{2\pi M k_b T^*}\right)^{\frac{3}{2}}\exp\left(-\frac{\hbar^2 p^2}{2Mk_bT^*}\right), \tag{3.5}$$

with the effective temperature, $T^*$, being related to the average kinetic energy, $K_{av}$, of the atoms in the system by[3.15]

$$k_bT^*=\frac{2}{3}K_{av}=\frac{1}{2}\int\hbar\omega Z(\omega)\coth\left(\frac{\hbar\omega}{2k_bT}\right)d\omega. \tag{3.6}$$

In this equation, $Z(\omega)$ represents the density of states of the lattice vibrations and shows that the effective temperature of an atom in the crystal is modified by its environment. Figure 3.1 shows the measured density of states for sodium[3.10] used to evaluate the effective temperature here. Using the momentum distribution defined by equations 3.5 and 3.6, the theory then predicts[3.16] that a monatomic system has high-energy wavevector scattering given by

$$S_{IA}(Q,\omega)=\left(\frac{1}{2\pi\sigma_S^{\,2}}\right)^{\frac{1}{2}}\exp\left(-\frac{(\hbar\omega-\hbar^2Q^2/2M)^2}{2\sigma_S^{\,2}}\right), \tag{3.7}$$

which is a Gaussian centred at a recoil energy of $\hbar^2\mathbf{Q}^2/2M$ for a wavevector transfer **Q**, with width $\sigma_s=\hbar^2\mathbf{Q}.\mathbf{p}/M$. $\hbar\mathbf{p}/M$ is the root-mean-square initial velocity of the atom, which can be

used to calculate the average kinetic energy. The $Q^2$ dependence of the recoil energy and the **Q** dependence of the width can be used to check the validity of the impulse approximation. The slope of the width, $\sigma_s$, versus **Q** gives the mean momentum of the atoms, which can be directly compared with the theory.

Departures from the impulse approximation cause changes in the predicted Gaussian scattering. For example, an asymmetric line shape and a lowering of the expected peak position may arise due to initial-state effects[3.17]. These arise in quantum systems at low temperatures, where the initial momentum distribution is not a Boltzmann distribution. These effects are important in $^4$He and affect measurement of the Bose condensate. They are not expected to be of importance in this study on sodium, which is carried out at relatively high temperatures. There are also departures from the impulse approximation due to final-state effects. These arise because the recoiling atom is not free. These final-state effects result in a broadening of the recoil scattering and have been partially accounted for already in the harmonic, isotropic model of a solid by introducing an effective temperature. If the system does not behave like a harmonic solid, then obviously this model will not fully account for the scattering measured. Final-state effects also change the peak position of the dynamical scattering, but in the opposite sense to initial state effects[3.18].

### 3.2.2 Y-Scaling

It is useful to introduce an analysis technique for DINS known as *y*-scaling[3.18]. In the *y*-scaling transformation every point in (**Q**,ω) space corresponds to a unique point in the atomic momentum space $\hbar$**p**. For an isotropic system the following relations hold

$$S(Q,\omega)=\frac{M}{\hbar Q}J(y), \tag{3.8}$$

$$\hbar y=\frac{M}{\hbar Q}\left(\hbar\omega-\frac{\hbar^2Q^2}{2M}\right), \tag{3.9}$$

$$J(y)=\int n(p_x,p_y,y)dp_x dp_y, \tag{3.10}$$

where the z-axis has been taken to lie along the scattering vector, **Q**. J($y$) is known as the neutron Compton profile and is analogous to the Compton profile for x-ray scattering[3.19]. Consequently, J($y$) is the probability that an atom has the momentum component of magnitude $\hbar y=\hbar p_z$ along **Q**, the direction of scattering. Substituting equation 3.5 for the momentum distribution into equation 3.10, the neutron Compton profile for an isotropic harmonic system has the following Gaussian form

$$J(y)=\left(\frac{1}{2\sigma_y}\right)^{\frac{1}{2}}\exp\left(-\frac{y^2}{2\sigma_y^{\,2}}\right), \tag{3.11}$$

with the width $\sigma_y$ given by

$$\sigma_y=|\hbar y|=(Mk_bT^*)^{\frac{1}{2}}. \tag{3.12}$$

Note that the width of J($y$), $\sigma_y$, is equal to $\hbar y$ - the initial z-component of the momentum of an atom in the target system. For an isotropic system the width of the neutron Compton profile is Q independent, and means that widths from different detectors can be averaged together.

If the density of states, $Z(\omega)$, for a system is known it is a simple matter to compare the widths extracted from the neutron Compton profiles with equation 3.12 - assuming the impulse approximation holds. It can then be determined whether the scattering system behaves like an isotropic harmonic solid or not.

## 3.3 The Experiment

The sodium sample used in this study was polycrystalline and was placed between two flat aluminium plates with 3cmx3cm vanadium windows, such that the sample thickness was 5mm. At this thickness the sodium gave about 4% scattering- low enough that multiple-

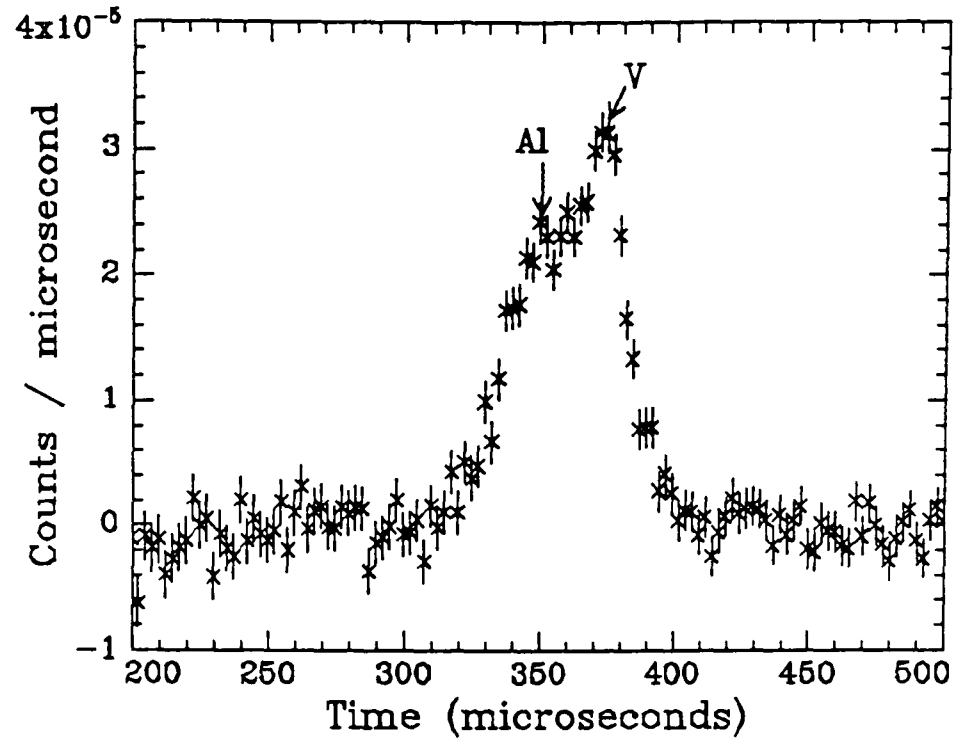


Figure 3.2: The background scattering from the empty can and cryostat. Measured using back-scattering detector 2 with a gold analyzer foil.

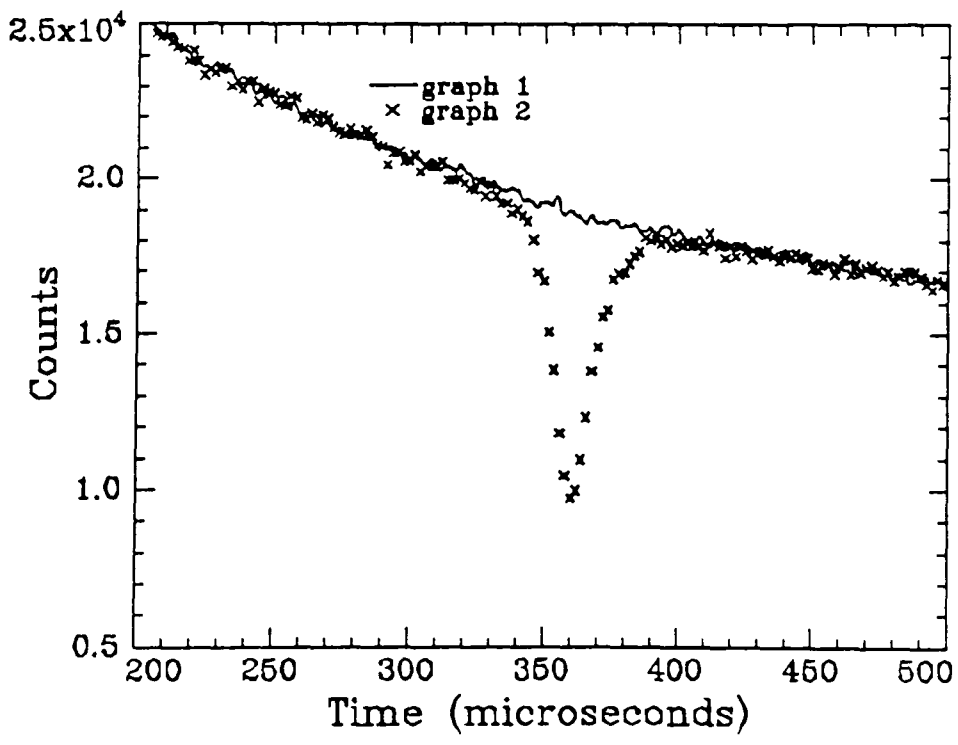


Figure 3.3: Measuring the recoil scattering using the foil difference technique. Graph 1 represents the foil out measurement, graph 2 the foil in. Gold foil, detector 2.

scattering effects were not significant. In a previous experiment on beryllium the multiple-scattering effects caused an asymmetric line shape, and thus looking for deviations from the impulse approximation was not possible[3.5]. The vanadium windows were 0.04mm thick, and were chosen because vanadium (M=51amu) has a mass which is significantly different from sodium (M=23amu) and because it is a weak scatterer. The sample can was placed in a cryostat in order that the neutron Compton profile could be measured at various temperatures (30K, 100K, 200K, 300K) to observe any systematic changes in the widths with increasing temperature. An empty-can run was also measured so that the background effects could be subtracted from the measured recoil scattering, leaving the sodium signal. The empty-can run is shown in figure 3.2. There is a contribution from the vanadium windows of the sample holder and from the cryostat which is aluminium (M=27amu). Notice the cryostat scattering appears at lower times than the sodium (compare with figure 3.3), due to the fact that the scattering distances of the cryostat are different from the sample.

### 3.3.1 The Time-of-Flight Spectrometer EVS

The data to measure the atomic momentum distribution of sodium were collected as time-of-flight spectra on the EVS spectrometer at the Rutherford Appleton Laboratory. This has a large flux of high-energy neutrons, as required for DINS. EVS has four banks of $^3$He detectors, two in the forward scattering position (±36°- ±54°) and two in the back scattering (±140°- ±152°) as shown in figure 3.4. The forward scattering banks contain ten detectors each and the back scattering fifteen. The moderator to sample distance on EVS is 11m, the distance from the sample to the forward scattering detectors is approximately 0.8m, and for the back scattering detectors the distance is 1m. These distances were calibrated along with the detector angles using a standard lead sample, by the methods outlined in Mayers et al[3.21]. The experiment was set up using two different types of analyser foil: gold and uranium, positioned such that each covered a forward and back scattering bank of detectors. The analyser foils use the nuclear resonance absorptions (Au-4.922eV, U-6.671eV) to define the final energy of the scattered neutrons, and a filter difference technique is then used to collect the data. This is illustrated in figure 3.3 where graph 1 represents the data collected when the foil is out, and graph 2 represents the scattering collected when the foil is in. Subtracting graph 2 from graph 1 gives the recoil scattering from the sample as a function

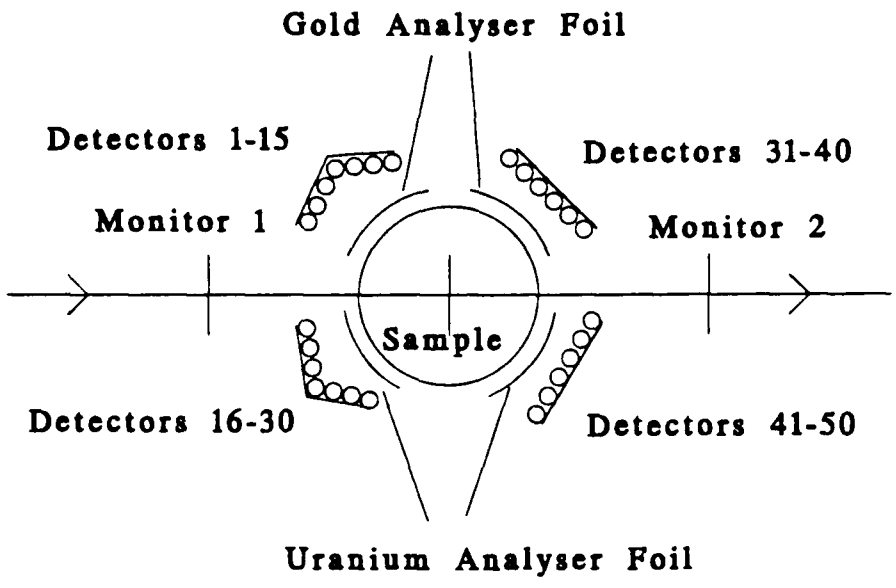


Figure 3.4a: Schematic diagram of EVS.

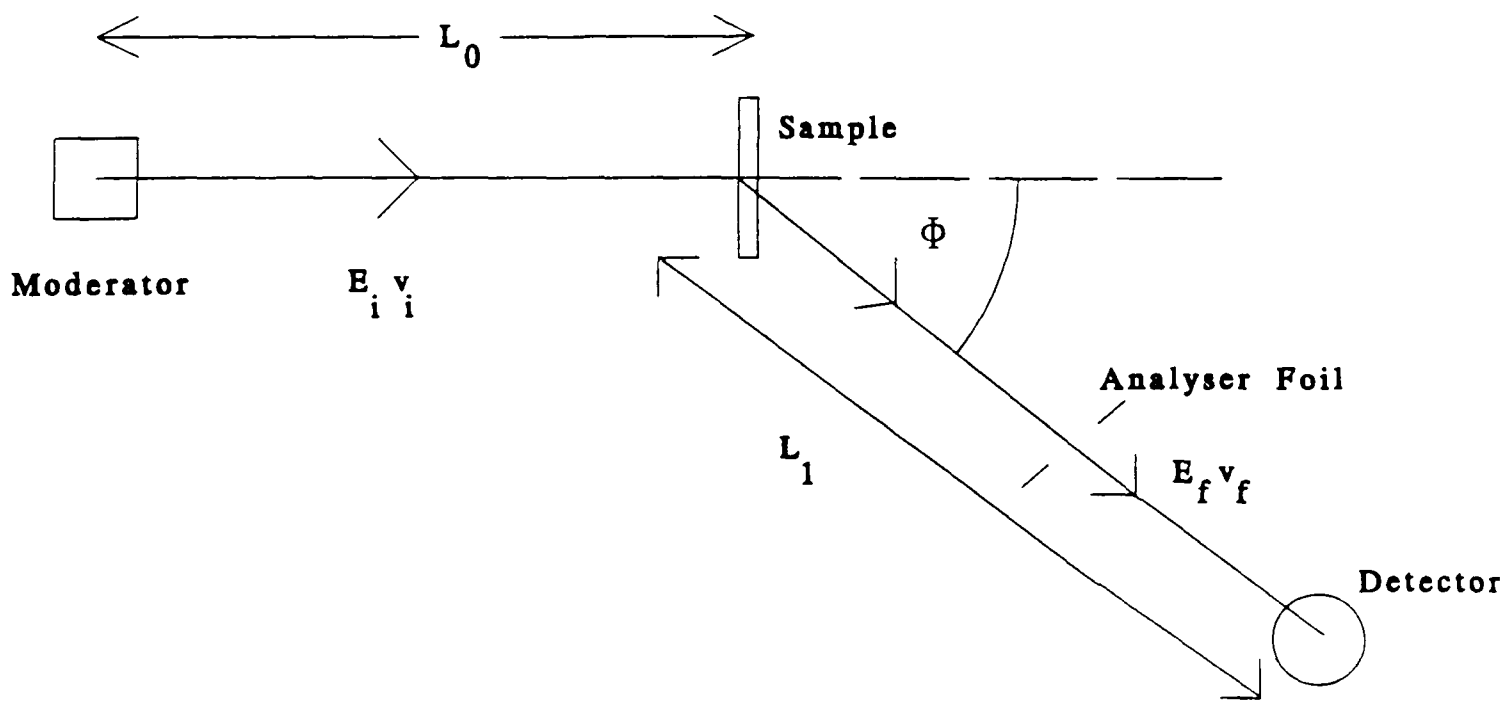


Figure 3.4b: Defining lengths and angles on EVS.

of time of flight. These scans are both normalised to the incident monitor count taking into account the energy efficiency of the monitor[3.10], [3.21]. The result of this subtraction is a time-of-flight spectrum containing the recoil scattering from the sodium as well as the background scattering from the can and the cryostat- this must be subtracted to give the scattering from the sodium alone. The remaining spectrum is then converted into (Q,ω)-space before the final transformation to y-space can be done.

## 3.3.2 Converting from Time-of-Flight to (Q,ω)-Space

The conversion from time-of-flight to (Q,ω)-space is now discussed. The energy lost by the scattered neutron to the system is calculated using the following equation

$$E=\hbar\omega=E_i-E_f=\frac{1}{2}m(v_i^2-v_f^2), \tag{3.13}$$

Where the scattered neutron energy, $E_f$, and therefore the final velocity, $v_f$, are fixed by the analyser foil. The initial energy, $E_i$, and velocity, $v_i$, can be determined from the time of flight, $t$, using equation 3.14

$$t=\frac{L_0}{v_i}+\frac{L_1}{v_f}+t_0. \tag{3.14}$$

$L_0$ is the primary neutron flight path from the moderator to the sample, and $L_1$ is the secondary flight path from the sample to the detector, as shown in figure 3.4b. Also, $t_0$ is a delay time in measuring $t$ which is approximately 5μs, and arises from the counting electronics.

The wavevector transfer can be calculated from the magnitude of the scattering vectors using

$$Q=(k_i^2+k_f^2-2k_ik_f\cos\Phi). \tag{3.15}$$

where Φ is the scattering angle as shown in figure 3.4b. Once **Q** and ω are known, equation 3.9 can be used to define the data in terms of $y$, and thus these values of **Q** and ω uniquely

relate $y$ to a point in the time-of-flight spectrum. These are easily calculated if $L_0$, $L_1$, $\Phi$ and $E_f$ are known.

### 3.3.3 The Resolution of EVS

When a neutron scattering Compton profile has been extracted from the data it not only contains contributions from the recoil scattering, but also resolution components, such that the measured profile has the form

$$J_m(y)=J(y)*R_\Phi(y)*R_L(y)*R_t(y)*R_E(y). \tag{3.16}$$

Here $J_m(y)$ is the measured profile, $J(y)$ is the contribution from the recoil scattering. $R_\Phi(y)$, $R_t(y)$, $R_L(y)$ and $R_E(y)$ are the resolution functions arising from the uncertainty in the detector angular positions, $\Phi$, the time of flight t, the flight paths $L_0$, $L_1$, and from uncertainty in the measured energy respectively. The uncertainty in the time-of-flight measurements is due to the finite width of the time bins. For these time of flights, the uncertainty is of the order 0.1% of the measured time. The most important contribution is that arising from the energy resolution and this component is proportional to the resonance width of the foil used. The different foils give different energy resolutions, $\Delta E$, because they have different resonance widths (FWHM, $\Delta E_{Au}$=0.134eV, $\Delta E_U$=0.051eV). The uranium foils have better resolution, but lower transmission than the gold foils and thus result in worse statistics for equal counting times. The energy component of the resolution function on EVS is Lorentzian in shape and is the dominant instrumental effect. As well as depending on the widths of the resonance of the foil, in $y$-space it also depends upon the mass of the target system, which for sodium is 23amu. In $y$-space, when the mass of the target system is much larger than the mass of a neutron the width of the energy contribution has been formulated by Andreani et al[3.20] as

$$\sigma_E=\frac{M\left[1+\frac{L_1}{L_0}\right]}{2\hbar k_f \sin\left(\frac{\Phi}{2}\right)}\left(\frac{\Delta E}{2}\right). \tag{3.17}$$

$\Delta E$ is the resonance width of the analyser foil, with all the other symbols in equation 3.17 defined previously. Tables 3.1 and 3.2 show the energy resolution widths for a detector from the forward and back scattering banks with gold and uranium resonance foils for the sodium sample. Here $\sigma_E$ is the HWHM of the Lorentzian component of the resolution function. It is seen that the resolution from the back scattering detectors (ie higher angle) is smaller than that from the forward scattering banks, and that the uranium foils have better resolution than the gold, due to the narrower uranium resonance width.

**Table 3.1 The Resolution Widths For Sodium Using a Gold Analyser Foil.**

| Scattering Angle, $\Phi$ | $\sigma_E/\hbar$ (Å$^{-1}$) | $\sigma_\Phi/\hbar$ (Å$^{-1}$) | $\sigma_t/\hbar$ (Å$^{-1}$) | $\sigma_L/\hbar$ (Å$^{-1}$) |
|---|---|---|---|---|
| 44° | 23.0 | 0.46 | 1.5 | 2.2 |
| 145° | 9.3 | 0.67 | 1.2 | 0.8 |

The resolution due to the uncertainties in the angular spread of the detectors, the detector and sample distances as well as the time of flight are assumed to be Gaussian functions. For sodium these widths are small compared to the energy contribution. The angular component, $\sigma_\Phi$, and those arising from the times of flight, $\sigma_t$, and distances, $\sigma_L$, are given in tables 3.1 and 3.2. Note in these cases $\sigma$ corresponds to the standard deviation of the Gaussian which models these resolution components. These resolution widths have been estimated using the uncertainties obtained from the calibration of EVS[3.10], [3.21] and using the formulae developed by Andreani et al[3.20].

**Table 3.2 The Resolution Widths For Sodium Using a Uranium Analyser Foil.**

| Scattering Angle, $\Phi$ | $\sigma_E/\hbar$ (Å$^{-1}$) | $\sigma_\Phi/\hbar$ (Å$^{-1}$) | $\sigma_t/\hbar$ (Å$^{-1}$) | $\sigma_L/\hbar$ (Å$^{-1}$) |
|---|---|---|---|---|
| 44° | 9.5 | 0.65 | 1.3 | 2.6 |
| 145° | 4.0 | 0.95 | 1.0 | 0.9 |

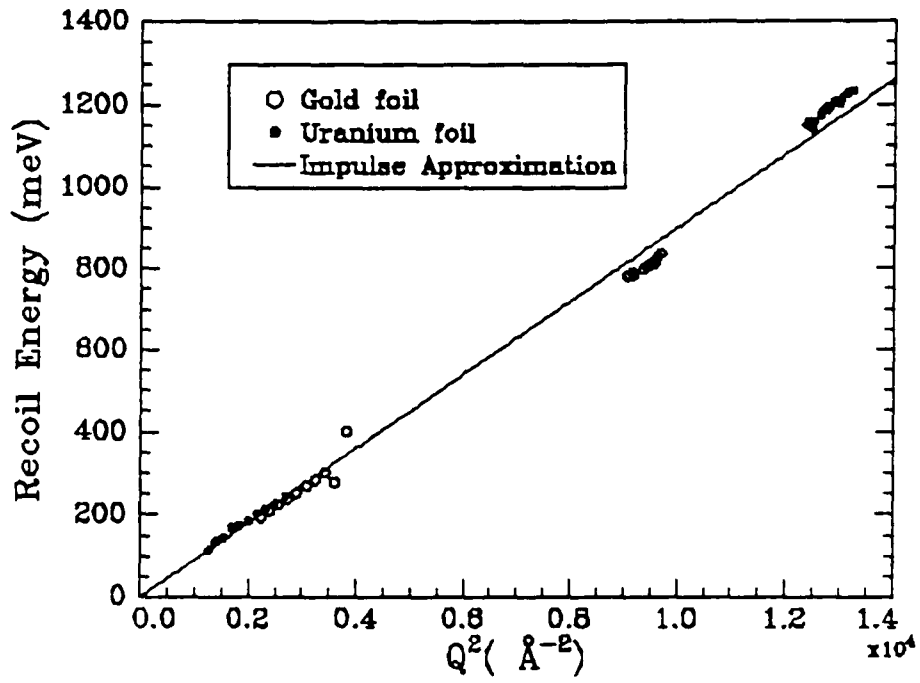


Figure 3.5: Checking the Impulse Approximation is valid for sodium by comparing the recoil energy, determined at 30K, with the theory.

Once the resolution components are known, the contribution of the recoil scattering can be extracted from the measured neutron compton profile. This is done by fitting the data to a convolution of the Lorentzian energy resolution function with a Gaussian including the width from the angular, length and time resolutions for each detector, with a Gaussian modelling the unknown recoil scattering.

## 3.4 The Data

As discussed previously, the data was initially collected as time-of-flight spectra, first with the analyser foil in and then out. These two spectra must be subtracted before any other transformations can take place, the result is data at a fixed final energy as defined by the analyser foil. Next the empty can run was subtracted from the data. Then the time-of-flight data for each detector was transformed into $(\mathbf{Q},\omega)$-space using standard EVS routines described in reference [3.21]. Once the data is in this format it can be used to check the validity of the impulse approximation for the system in question.

### 3.4.1 The Validity of the Impulse Approximation for Sodium

Before proceeding with the comparison of the sodium data with the model for a harmonic solid, it is important to know if the impulse approximation is valid for this experiment. To test the validity of the impulse approximation, a graph of the recoil energy versus $Q^2$, ie the peak positions of $S(\mathbf{Q},\omega)$, is shown in figure 3.5 for each detector. This was done for the recoil energies at all temperatures measured, and figure 3.5 shows the data at 30K. The straight line is the prediction of the impulse approximation, $E_{Recoil}=\hbar^2Q^2/2M$. The data points are from both the gold and uranium foil detectors at forward and back-scattering angles. The back scattering detectors do not lie exactly on the impulse approximation line: the uranium sitting slightly above and the gold slightly below. If these deviations were due to the failure of the impulse approximation both would be expected to lie on the same side of the line. For example, any deviations from the impulse approximation due to final-state effects would result in data points which lay below the straight line[3.13]. It is thus concluded that there is no significant deviation from linear behaviour and that the discrepancies in the back-scattering detectors are due to systematic errors arising in the data analysis, probably due to the can

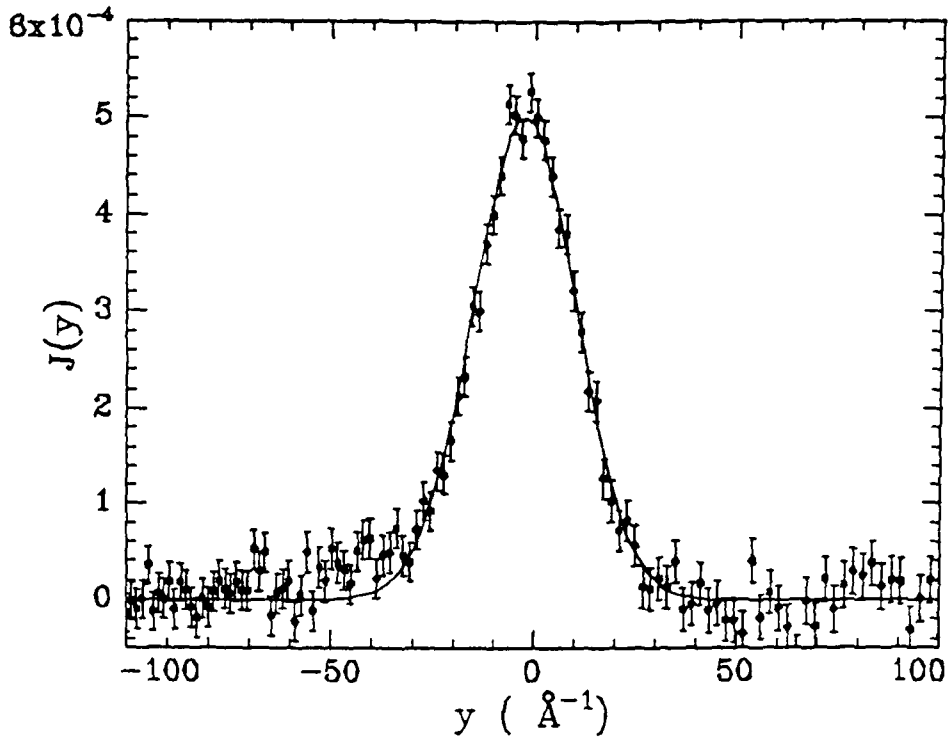


Figure 3.6: The neutron compton profile from a gold forward scattering detector at 100K. The solid line represents a fit to a Voigt function.

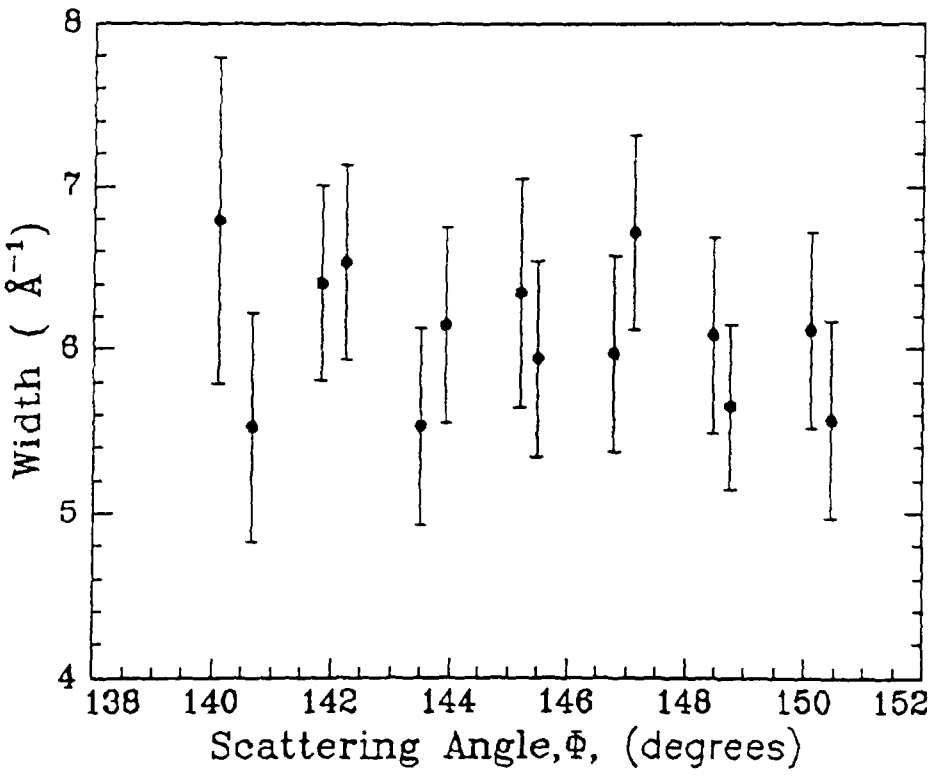


Figure 3.7: Widths, $\sigma_y/\hbar$, extracted form the neutron compton profiles for the uranium back-scattering detectors at 30K. Notice the widths are angle independent.

subtraction.

Next a transformation to y-space was performed[3.21]. The result of one of these transformations for a gold forward scattering detector is shown in figure 3.6 along with a fit to a Voigt function - a Gaussian convoluted with the Lorentzian energy resolution function as discussed in the previous section. Note that the recoil scattering is symmetric, as expected for an isotropic harmonic solid. The width of the recoil scattering was extracted from the Voigt function and figure 3.7 shows a graph of these widths at 30K, versus the detector angle for the uranium back-scattering bank. The widths of the neutron Compton profiles are independent of the detector angle within the accuracy- the Q dependence having been removed by the y-scaling. This, along with the $Q^2$ dependence of the peak positions (figure 3.5) shows that the data collected on EVS for sodium are consistent with the impulse approximation, between 30K and 300K, and hence that the analysis method is appropriate. Note that at T=30K, the average width of the recoil scattering is 5.9±0.3Å. This is smaller than the energy resolution widths shown in tables 3.1 and 3.2, and leads to relatively large errors, of order 10%, in the widths extracted from the fits for individual detectors, and thus necessitates averaging. This problem is aggravated by the large atomic mass of sodium compared to that of a neutron.

### 3.4.2 Comparing the Compton Widths with an Isotropic Harmonic Model

Having shown that the impulse approximation holds for this experiment, the widths extracted from the neutron Compton profiles can now be compared with the theory outlined in section 3.2.3 for an isotropic harmonic solid. The widths extracted from the fits are known only to an accuracy of 6% for each detector in the back scattering bank and 10% for the forward scattering. Since the **Q**-dependence has been removed by the *y*-scaling (figure 3.7), the widths from the detectors in each bank have been averaged. Figure 3.8 shows the temperature dependence of the widths along with a comparison of the theory for a harmonic solid (equation 3.12) using the measured density of states for sodium, $Z(\omega)$, in the effective temperature calculation. The density of states for sodium, shown in figure 3.1, was calculated by Dixon et al[3.7] from the phonon dispersion relation measured by Woods et al[3.11] using inelastic neutron scattering techniques. This density of states was digitised and a numerical

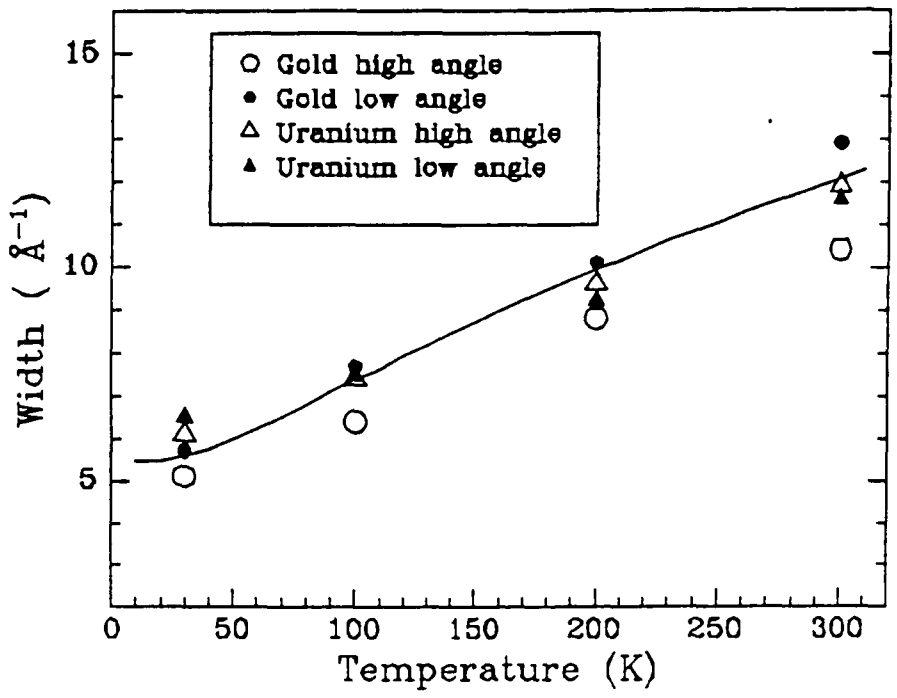


Figure 3.8a: The temperature dependence of the recoil widths, $\sigma_y/\hbar$, for sodium. The symbols represent the average from each bank. The solid line is the isotropic harmonic model.

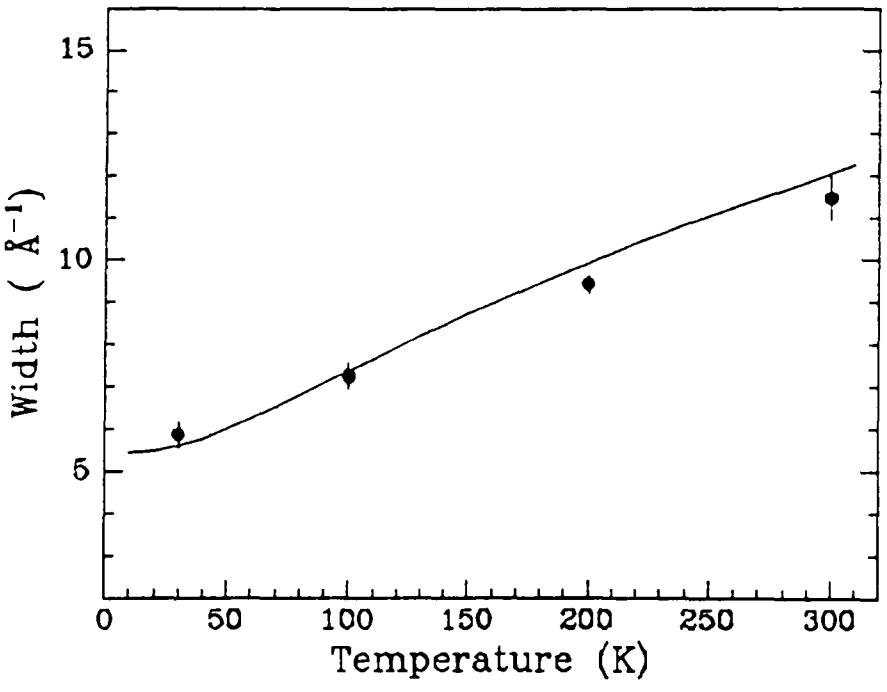


Figure 3.8b: The average width, $\sigma_y/\hbar$, of the recoil from the four banks of detectors. The error bars are defined by the standard deviation of the mean for the four banks.

integration was used to evaluate the effective temperature from equation 3.6. Figure 3.8a shows that the widths from the gold high-angle detectors are systematically lower than the widths from the other banks, this is due to errors introduced when subtracting the empty can run. Figure 3.8b shows the average widths from all four banks. Within the experimental spread of widths, the data are well described by the theory and hence there is no evidence for any systematic deviations from harmonic solid behaviour. At 30K, below the structural phase transition in sodium at 35K from the body-centred cubic structure to the hexagonal close-packed structure temperature[3.22], no evidence is seen for any change.

On EVS the instrumental resolution in $y$-space deteriorates with target mass according to equation 3.17, and so it will be difficult to obtain more accurate results for the recoil scattering for large masses and hence to observe any deviations from the impulse approximation. In fact, with the present resolution on EVS, accurate measurements of atomic momentum distributions are limited to atomic masses of less than 15amu, and thus it is not surprising that there is no deviation from isotropic harmonic behaviour seen with sodium. EVS has been designed primarily for studying the momentum distribution of hydrogen and deuterium. This makes it useful in the study of polymers for confirming the hydrogen bonding. Successful studies have also been carried out on metal hydrides[3.6], [3.10].

## 3.5 Conclusions

Using the EVS spectrometer it has been shown that the neutron recoil scattering from sodium below 300K is consistent with the impulse approximation. Comparing the widths extracted from the neutron Compton profiles, between 30K and 300K, with the harmonic model for sodium, good agreement is seen within the accuracy of the data (about 4% using the standard deviation of the means for the four banks as an estimate of the error). Thus from this experiment the recoil scattering from sodium may be considered to be essentially from a collection of particles interacting with harmonic forces.

## References


[3.1].R.A.Cowley, A.D.B.Woods: Phys.Rev.Letts. 21 787 (1968).

[3.2].O.K.Harling: Phys.Rev.Letts. 24 1046 (1970).

[3.3].H.A.Mook, R.Scherm, M.K.Wilkinson: Phys.Rev. A6 2268 (1972).

[3.4].P.C.Hohenberg, P.M.Platzman: Phys. Rev. 152 198 (1966).

[3.5].D.F.McMorrow, R.A.Cowley, R.M.Nicklow, P.W.Mitchell, A.D.Taylor, M.Mostoller: J.Phys:C 2 1045-1057 (1990).

[3.6].A.C.Evans, J.Mayers, D.N.Timms, M.J.Cooper: Z.Naturforsch 48a 425 (1993).

[3.7].A.E.Dixon, A.D.Woods, B.N.Brockhouse: Proc.Phys.Soc. 81 973 (1963).

[3.8].R.O.Hilleke, P.Chaddah, R.O.Simmons, D.L.Price, S.K.Sinha: Phys. Rev. Lett. 52 847-50 (1984).

[3.9].M.Hewitt: PhD Thesis, Edinburgh University (1989) and M.Hewitt, R.A.Cowley, A.D.Taylor: to be published.

[3.10].A.C.Evans: Ph.D. Thesis, University of Warwick (1993).

[3.11].A.D.Woods, B.N.Brockhouse, R.H.March, A.T.Stewart, R.Bowers: Phys. Rev. 128 1112 (1962).

[3.12].D.L.Price, K.Skold: Methods of Experimental Physics 23A 1 (1986).

[3.13].J.Mayers: Europhys. Lett. 10 727-732 (1989).

[3.14].J.M.F.Gunn, M.Warner: Z.Phys. B56 13 (1984).

[3.15].M.S.Nelkin,D.E.Parks: Phys.Rev. 119 1060 (1960).

[3.16].S.W.Lovesy: "Theory of Neutron Scattering from Condensed Matter" Vol1 (Oxford:OUP 1984).

[3.17].J.Mayers: Phys. Rev. B41 41 (1990).

[3.18].V.F.Sears: Phys. Rev. B30 44 (1984).

[3.19].B.Williams: "Compton Scattering "(McGraw-Hill, New York, 1977).

[3.20].C.Andreani, G.Baciocco, R.S.Holt, J.Mayers: Nucl. Inst. Meth. Phys. Res. A276 297 (1989).

[3.21].J Mayers, A.C.Evans: "Measurements of Atomic Momentum Distributions by Neutron Compton Scattering; Progress on the EVS Spectrometer During 1990." (RAL-91-048) June 1991.

[3.22].D.L.Martin: Proc. Roy. Soc. A254 433 (1960).

# Magnetic Excitations

# Chapter 4

# An Introduction to Antiferromagnetism

In this chapter, models are developed from classical spin-wave theory for the magnetic excitations in antiferromagnetic systems. Before the details of the excitations are outlined, section 4.1 reviews some basic concepts of magnetism. Section 4.2.1 deals with the Néel ground state of an antiferromagnet, which is used as a basis for the linear spin-wave theory developed in section 4.2.2. The notation developed there is then used to evaluate the neutron scattering function for one-magnon processes in section 4.2.3. Finally, the predictions for two-magnon Raman scattering studies are examined as a complementary technique. The theory for this scattering is discussed in section 4.2.4.

## 4.1 Exchange Interactions and the Heisenberg Hamiltonian

Long-range magnetic order arises from quantum mechanical exchange interactions between the magnetic ions in a system[4.1]. The exchange mechanism causing the ordering is the Coulomb interactions between the electrons of the ions combined with the Pauli exclusion principle. This is positive in ferromagnets, where the moments of neighbouring ions are parallel to each other and is known as the *direct exchange*. In systems where the exchange interaction is negative, antiparallel alignment of nearest-neighbour spins occurs and this gives rise to antiferromagnetic structures. Many antiferromagnets are insulators in which the magnetic ions are separated from each other by non-magnetic ions often over large distances. In such systems, the overlap of the magnetic-ion wavefunctions is negligible and the interaction occurs via the intervening ligand ion in a process known as *superexchange* [4.2]. The interaction Hamiltonian for these ordered systems, with only nearest-neighbour interactions can be written in the form shown in equation 4.1

$$H=-2J_{NN}\sum_{(l,m)}[aS_l^ZS_m^Z+b(S_l^YS_m^Y+S_l^XS_m^X)]. \qquad \textbf{(4.1)}$$

The summation is over pairs of spins *(l,m)*. $J_{NN}$, the exchange integral between nearest-

neighbour pairs of spins is positive for a ferromagnetic system and negative for antiferromagnets. $S_l^z$ is the $z$-component of the spin of the $l$th ion. For the case when $a$=$b$=1, equation 4.1 is known as the *Heisenberg* model. In this model the interactions are wholly isotropic, and the spins have no preferred direction. Theoretically, it has been shown that no long-range order can exist for a Heisenberg system above T=0 K, if the dimensionality is less than three[4.3]. In practise, however, anisotropies in two-dimensional systems and interchain coupling in one-dimensional systems lead to finite Néel temperatures, below which long-range ordering occurs[4.4]. At the other extreme, when $a$=1 and $b$=0, equation 4.1 describes a system in which the exchange interactions are wholly anisotropic, with the spins constrained to lie along the $z$-direction. This limit is known as the *Ising* model. The Ising model can have long-range order for all systems at temperatures above T=0 K, except for a one-dimensional magnet. In an ideal one-dimensional system no long-range order exists in either the Ising or the Heisenberg models, when only nearest-neighbour interactions exist. Finally, in the Hamiltonian 4.1, if $a$=0 and $b$=1, this is called the *XY-model*, or the planar Heisenberg model. This has the spins constrained to lie in the $xy$-plane. The Heisenberg and Ising models shall be concentrated on in this work. The wholly-isotropic Heisenberg model is used as a basis for the linear spin-wave theory described in section 4.2. In chapter 7, the phase transition of the two-dimensional Ising model will be discussed in more detail. The Ising model is one of the most important and fundamental models in magnetism because in two dimensions it has exact solutions.

Realisations of the models discussed above are found in some crystals, and these have been used to test the predictions of the theoretical models[4.5]. The earliest examples of antiferromagnets studied were the three-dimensional insulating structures: the cubic perovskite structures ($RbMnF_3$ and $KNiF_3$), the rutile structures ($MnF_2$, $FeF_2$ and $NiF_2$) and the rocksalt structures (MnO and NiO)[4.6]. The development of theories for magnetism involving lower dimensions prompted studies of two and one-dimensional antiferromagnets in the early 1970's. The layered $K_2MF_4$ structures, with M being Ni or Mn, were found to be excellent examples of two-dimensional Heisenberg systems[4.7]. When M is Co, the system behaves like a two-dimensional Ising system[4.8].

The discovery of the cuprate superconductors has brought about a renewed interest in

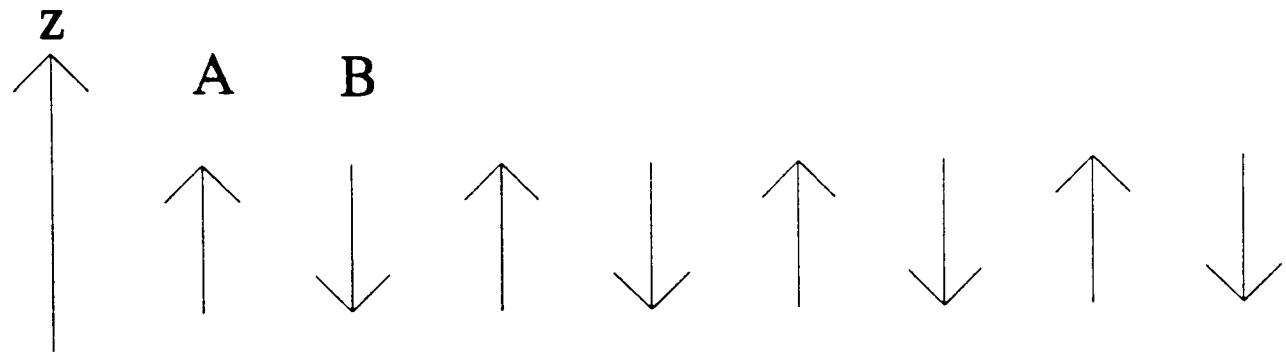


Figure 4.1a: The Néel State.

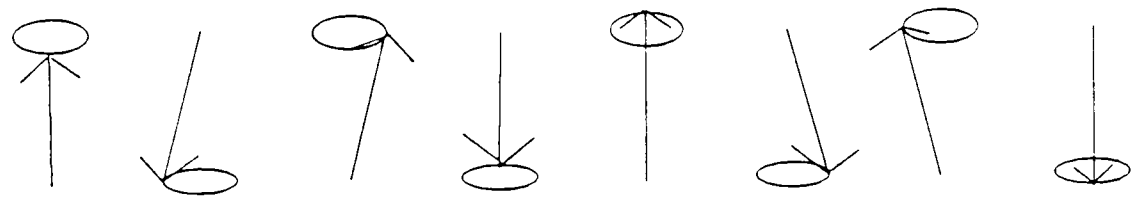

Figure 4.1b: Antiferromagnetic Spin Waves.

two-dimensional antiferromagnetism, with the undoped systems being antiferromagnetic (see chapters 6 and 8, and references therein). These planar systems have weak interactions perpendicular to the layers, with a ratio of interplanar to intraplanar magnetic interactions of the order $10^{-4}$, and thus they are well described by a two-dimensional approximation. One-dimensional antiferromagnets are also well approximated by some fortuitous bonding in crystal structures. For example, $KCuF_3$ is an excellent example of a one-dimensional chain with the bonds being strongly directional, leading to a large overlap along one axis, with negligible interactions in the other directions[4.5].

The following chapters present studies of two antiferromagnets. The first, CuO, has strong magnetic interactions along one particular crystallographic direction, and so is a one-dimensional system. It orders at finite temperatures due to ferromagnetic coupling between the antiferromagnetic chains, with the Néel temperature being $T_N$=230 K. The other system examined, $KFeF_4$, is an excellent example of a two-dimensional antiferromagnet, with predominantly Heisenberg-like nearest-neighbour interactions. It has a finite transition temperature, $T_N$=137 K, because of small Ising-like anisotropy effects. These will be discussed in more detail in the relevant chapters.

## 4.2 Magnetic Excitations

Having given some details of how antiferromagnetic structures can be approximated in real crystals, the nature of the excitations in these systems will now be discussed. The theory involves an approximation known as linear spin-wave theory. This is built upon an approximate ground state, called the Néel state, as discussed in section 4.2.1. The theory also assumes that the magnetic ions have no orbital angular momentum in the ground state. Despite the approximations made in linear spin-wave theory, it is found to be in excellent agreement with the experimental results.

### 4.2.1 The Néel State and Spin Waves

Figure 4.1a shows the classical ground state of an antiferromagnet which is known as the Néel state. The Néel state is an approximation upon which linear spin-wave theory is

developed, and provides a description for non-interacting spin-wave excitations which is in good agreement with those observed experimentally. In the Néel state at T=0 K, spins on the *A* sublattice are fully aligned along the +*z* direction, such that $S^z_A=S$, where *S* is the total spin of the magnetic ion. Conversely, the spins on the *B* sublattice are fully aligned along the -*z* direction and thus $S^z_B=-S$. The Néel state is an approximation because it ignores zero-point spin fluctuations, which are most important for low spins and the Néel state is not an eigenfunction of the Heisenberg Hamiltonian[4.9]. In real antiferromagnets it is found that anisotropies stabilise the ground state, leading to smaller fluctuations from the Néel state than those predicted by the theories. These anisotropies can be due to crystal field effects, or dipole-dipole interactions, and are dealt with in chapter 6. The ground state is not a problem in ferromagnetic systems, where the fully aligned ground state is exact.

A spin excitation is a deviation of a spin from the fully aligned Néel state to a state which, for the *A* sublattice results in a reduction of the spin along the *z*-direction such that $S_A^z= S-1$. Such a quantised deviation is known as a magnon. These spin deviations can be represented as a set of travelling sinusoidal waves, known as spin waves, and are analogous to phonons in nuclear displacements. Figure 4.1b shows a representation of spin waves in an antiferromagnetic system. In an antiferromagnet there are two types of spin wave present, those associated with the *A* sublattice and those on the *B* sublattice. In the absence of an applied magnetic field the spin-wave dispersion relations for the A and B sublattice are degenerate. A neutron can be used to create or annihilate a spin deviation. When this happens the neutron loses or gains energy. Thus, by knowing the momentum transferred and the change in energy a dispersion relation of the spin-wave excitations can be built up using neutron scattering techniques (see section 4.2.3).

## 4.2.2 One-Magnon Processes and Linear Spin-Wave Theory

The dispersion relation for the spin-wave excitations in an antiferromagnet can be developed from the general Hamiltonian of a system with the following form

$$H=-2\sum_{(l,m)} J_{lm}S_l.S_m-2\sum_{(m,m')} J_{mm'}S_m.S_{m'}-2\sum_{(l,l')} J_{ll'}S_l.S_{l'} \\ -g\mu_b H_A(\sum_l S_l^z-\sum_m S_m^z). \qquad (4.2)$$

This general Hamiltonian[4.9] allows for exchange interactions between spins, $S$, on the two sublattices $A$ and $B$ via the exchange term $J_{lm}$, and also for those on the same sublattice with exchange energies, $J_{mm'}$ and $J_{ll'}$. Here the summation are over pairs of ions, with $l$ and $m$ referring to spins on the $A$ and $B$ sublattices respectively. $H_A$ is the effective anisotropy field, which assumes that the easy axis of the antiferromagnet is the $z$-direction. Anisotropy effects, and how they arise will be discussed in more detail in chapter 6. The $H_A$ term can also be used to include a term due to an externally applied field- this will not be considered here. The method used to develop the spin-wave dispersion relation from equation 4.2, is due to Holstein and Primakoff[4.9]. It involves a Fourier transformation of the spin variables, $\mathbf{S}_l$, and assumes that the magnons are non-interacting. This assumption is valid at low temperatures. The transformation method is fully detailed in many standard texts including Keffer[4.9], and Kittel[4.10], with important steps being outlined here.

Firstly, the spin operators are replaced by creation and annihilation operators, which represent the creation and annihilation of a deviation from the fully aligned Néel state. These are introduced separately for deviations on each of the magnetic sublattices A and B, representing the fact that two species of spin wave are present in an antiferromagnetic system:

$$
\begin{aligned}
S_l^{\pm} &= S_l^{x} \pm i S_l^{y}, & S_m^{\pm} &= S_m^{x} \pm i S_m^{y}, \\
S_l^{+} &= (2S_a)^{1/2} f_l a_l^{-}, & S_m^{+} &= (2S_b)^{1/2} b_m^{+} f_m, \\
S_l^{-} &= (2S_a)^{1/2} a_l^{+} f_l, & S_m^{-} &= (2S_b)^{1/2} f_m b_m^{-}, \\
S_l^{Z} &= S_a - a_l^{+} a_l^{-}, & S_m^{Z} &= -S_b + b_m^{+} b_m^{-}, \\
f_l &= [1 - a_l^{+} a_l^{-}/2S]^{1/2}, & f_m &= [1 - b_m^{+} b_m^{-}/2S]^{1/2}.
\end{aligned}
\qquad \textbf{(4.3)}
$$

The creation and annihilation operators satisfy the commutation relations for Bose operators. In the Holstein-Primakoff approximation, $f_l$ is taken as 1. This is equivalent to neglecting the interaction between spin waves.

Fourier transforms of these variables are then performed, introducing variables that represent the deviations as sinusoidal waves, i.e. spin waves with wavevector $\mathbf{q}$. These variables are related to each other by the following equation

$$a_l^{\pm}=\frac{1}{N^{1/2}}\sum_q a_q^{\pm}e^{\mp iq.r_l}, \tag{4.4}$$

and similarly for the B sublattice operators. This leads to a Hamiltonian of the form

$$H=const+\sum_q A_q(a_q^+a_q^-+b_q^+b_q^-)+B_q(a_q^+b_q^-+a_q^-b_q^-). \tag{4.5}$$

In this equation only the quadratic terms have been included and $A_q$ and $B_q$ are defined in equation 4.9.

Making a suitable canonical transformation of the spin-wave operators removes cross terms involving spin-wave variables from the two different sublattices. The appropriate transformation is

$$\begin{aligned} a_q^+&=u_q\alpha_q^+-v_q\beta_q^-, & b_q^+&=v_q\alpha_q^-+u_q\beta_q^+, \\ a_q^-&=u_q\alpha_q^--v_q\beta_q^+, & b_q^-&=v_q\alpha_q^+-u_q\beta_q^-. \end{aligned} \tag{4.6}$$

where

$$u_q^2-v_q^2=1. \tag{4.7}$$

Equation 4.7 arises from the commutation relations for Bose operators. These transformations lead to an excitation Hamiltonian of the following form

$$H=\sum_q E_\alpha(q)(\alpha^+\alpha^-+\frac{1}{2})+E_\beta(q)(\beta^+\beta^-+\frac{1}{2}). \tag{4.8}$$

The resultant Hamiltonian is thus the sum of two independent spin-wave modes corresponding to the two sets of operators $\alpha$ and $\beta$. The operator-independent terms have been neglected in this expression. The final transformation results in the restrictions on the allowed energies of the spin waves for a given wavevector and thus defines the dispersion relation. When there is no applied magnetic field the dispersion relations for the spin waves on the two sublattices are degenerate and have the following form

$$E(q)=[A_q^2-B_q^2]^{1/2}=[(g\mu_b H_A+J_0^{aa}-J_0^{ab}-J_q^{aa})^2-(J_q^{ab})^2]^{1/2}, \tag{4.9}$$

with

$$J_q^{aa}=2S\sum_l J_{ll'}e^{(iq.r_{ll'})}. \tag{4.10}$$

and

$$J_q^{ab}=2S\sum_m J_{lm}e^{(iq.r_{lm})}. \tag{4.11}$$

In equations 4.10 and 4.11, $\mathbf{r}_{ll'}$ represents the vector distance between spins on the same sublattice, while $\mathbf{r}_{lm}$ is the vector distance between spins on opposite sublattices. Equation 4.9 can be used to calculate the dispersion relation for an antiferromagnetic system if the magnetic structure is known. This has been done in chapter 5 for CuO and chapter 6 for $KFeF_4$.

### 4.2.3 Neutron Scattering And Spin Waves

The notation developed for the dispersion relation in section 4.2.2 can be used to evaluate the neutron scattering cross section for antiferromagnets. This is fully described in Marshall and Lovesey[4.11]. It is found that the scattering from the $\langle S^zS^z\rangle$ terms in the scattering function are time-independent in the linear spin-wave approximation, and thus do not contribute to the inelastic scattering cross section. Evaluating the remaining terms in the scattering function equation (2.22), leads to the following form

$$S(\boldsymbol{Q},\omega)=\frac{(2\pi)^3}{N\nu_0}\sum_{a=\alpha,\beta}\sum_q (n_{q,a}+\frac{1}{2}\pm\frac{1}{2})\delta(E_a(q)\mp\hbar\omega)\delta(\boldsymbol{Q}\mp\boldsymbol{q}-\tau)I(\tau). \tag{4.12}$$

The ± represents the creation (+) or annihilation (-) of a spin wave with wavevector **q**. The term $n_q$ is the Bose occupation factor, $n_q=[exp(\hbar\omega(q)/kT)-1]^{-1}$, and determines the probability of a transition to a spin-wave energy $\hbar\omega(q)$. There are two summations in this equation. The first is over the two modes of spin waves, the second is over the wavevector **q** of the spin wave. The delta terms represent the conservation of energy and momentum, as discussed in

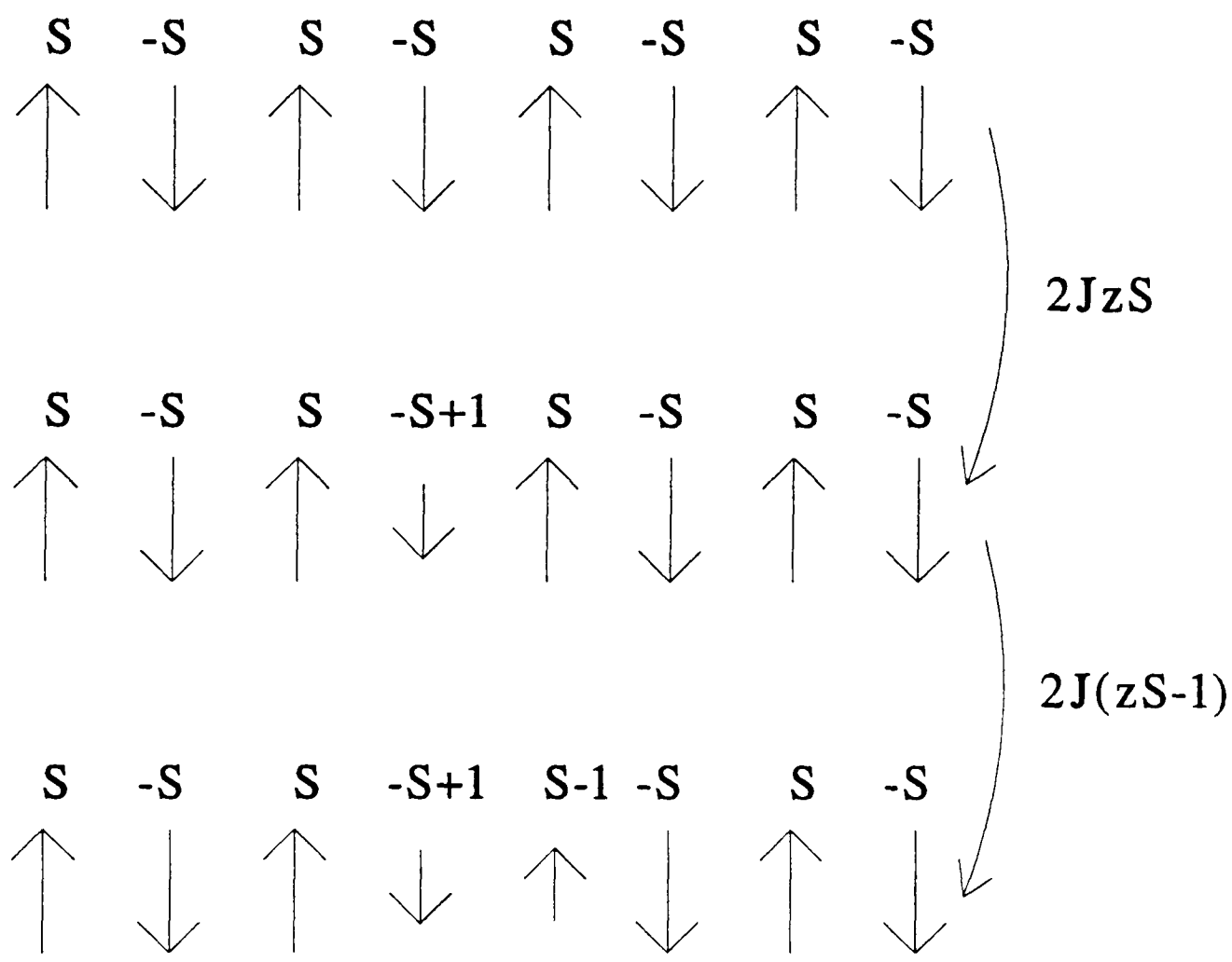


Figure 4.2: Successive steps in making a double spin flip on adjacent ions.

chapter 2. The $I(\tau)$ term is given by

$$I(\tau)=u_q+v_q+2u_qv_q\cos(\rho.\tau), \tag{4.13}$$

where the coefficients $u_q$ and $v_q$ arise from the canonical transformation of the spin wave variables, equation 4.7. $\rho$ is the vector separation of spins on opposite sublattices, and $\tau$ is the reciprocal lattice vector of the magnetic structure. The $I(\tau)$ term determines where the magnetic scattering will be strongest. For example, in a body-centred cubic lattice the magnetic scattering which coincides with the nuclear reflections will be weak, while the other magnetic reflections will be stronger. It should be recalled that the partial differential cross section, equation 2.20, is proportional to the magnetic form factor, which also affects the magnetic intensity measured at a particular reciprocal lattice point.

### 4.2.4 Two-Magnon Raman Scattering

Having shown how the one-magnon dispersion relation is calculated and measured using neutron scattering techniques, the theory for two-magnon Raman scattering is now discussed as a complementary technique. In two-magnon Raman scattering the wavevector transfer to the system, **Q**, is of order zero, and thus for two magnons to be created they must have wavevectors that sum to zero. It is found that the scattering is dominated by two-magnon processes where two magnons are created with equal and opposite wavevectors. Another necessary requirement for the Raman scattering is that the total *z*-component of the spin system must be conserved, and thus magnons must be created on opposite sublattices[4.12]. If the spin excitations were non-interacting the energy cost would be twice that of creating a single excitation. However as shown in figure 4.2, if the excitations occur for nearest-neighbour spins the energy cost is less by $2J_{NN}$, and this shifts the peak in the two-magnon density of states away from the classical limit of twice the one-magnon zone-boundary energy. This simple argument has been extended by Elliot and Thorpe[4.13], who have calculated how the magnon-magnon interactions affect the two-magnon density of states. The intensity of the two-magnon Raman scattering is proportional to this density of states. The theory has been applied to many systems and the results are in excellent agreement with the experimental data[4.13], [4.14].

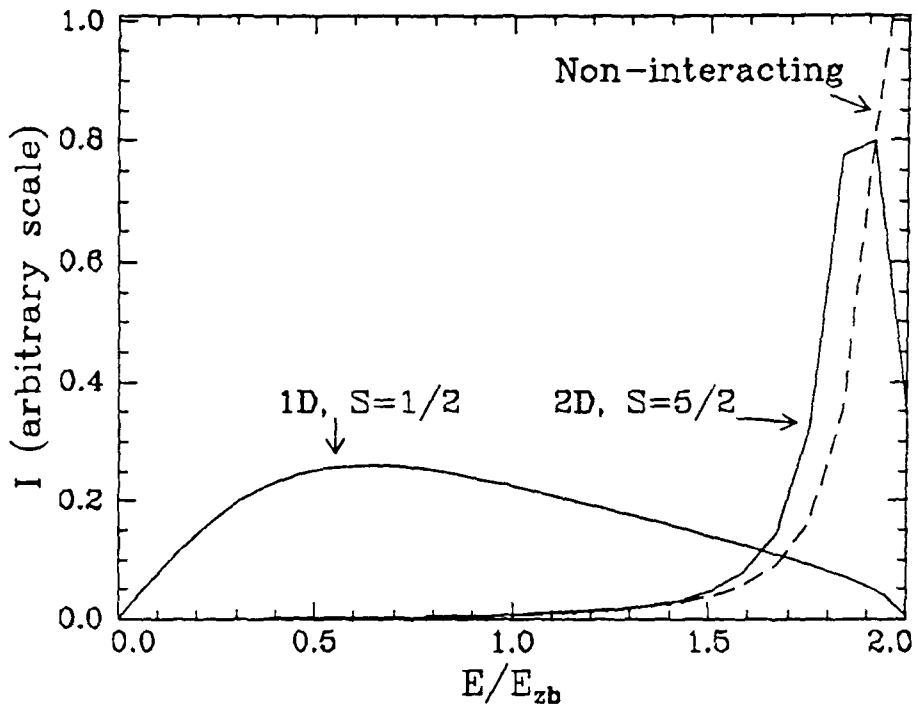


**Figure 4.3: The predicted two-magnon Raman scattering for the interacting and non-interacting theory.**

For a two-dimensional antiferromagnet the non-interacting density of states is given by the imaginary part of the following function

$$H_{2D}=\frac{1}{N}\sum_{q}\frac{(\cos q_x a-\cos q_y b)^2}{E^2-4E(q)^2}, \tag{4.14}$$

putting

$$E=E_R+i\varepsilon \qquad \varepsilon\rightarrow 0,$$

where $E$ is the energy of the Raman light, and $E$(q) is the appropriate dispersion relation for the system in question. The density of states has a peak at twice the zone-boundary energy of the dispersion relation. This is renormalised by the interaction terms such that the scattering is given by the imaginary part of the following function

$$G_{2D}=\frac{4NS^2}{\pi}\frac{(2E_{zb}-2J_{NN})H_{2D}}{1+(2J_{NN}(4E_{zb}-2J_{NN})H_{2D}}. \tag{4.15}$$

$E_{zb}$ represents the zone boundary energy of the one-magnon dispersion relation, and $J_{NN}$ is the nearest- neighbour interaction. This renormalisation is due to the magnon interactions and moves the peak of the scattering for a two-dimensional, S=5/2 antiferromagnet such as $KFeF_4$, by ~5% as shown in figure 4.3.

For a one-dimensional system, such as CuO, the non-interacting scattering has the form shown in equation 4.16.

$$H_{1D}=\frac{1}{N}\sum_{q}\frac{2\cos^2 qa}{E^2-4E(q)^2}. \tag{4.16}$$

this is changed by the magnon-magnon interactions to

$$G_{1D}=\frac{4NS^2}{\pi}\frac{(2E_{zb}-2J_{NN})H_{1D}}{(1+2J_{NN}(2E_{zb}-2J_{NN}))H_{1D}}. \tag{4.17}$$

This moves the peak of the scattering by 70%, as shown in figure 4.3. This calculation has

been performed using the dispersion relation for the one-dimensional S=1/2 CuO. Notice the larger effect the interactions have in the lower-dimensional system as expected from the simple Ising model of interactions. These spectra will be compared to experimental data in the following chapters.

## References


[4.1].P.W.Anderson: "Theory of Exchange Interactions in Insulators and Semiconductors" (Rado and Suhl, Magnetism I, 1963).

[4.2].P.W.Anderson: Phys. Rev. 79 350 (1950).

[4.3].P.C.Hohenberg: Phys. Rev. 158 383 (1967).
N.D.Mermin, H,Wagner: Phys. Rev Letts. 17 1133 (1966).

[4.4].M.Steiner, J.Villain, C.G.Windsor: Adv. Phys. 25 87 (1976).

[4.5].L.J.DeJongh, A.R.Meidema: Adv. Phys. 23 1 (1974).

[4.6].K.P.Sinha, N.Kumar: "Interactions in Magnetically Ordered Solids" ((Oxford University Press, 1980).

[4.7].H.W.deWijn, L.R.Walker, R.E.Walstedt: Phys. Rev. B8 285 (1973).

[4.8].M.T.Hutchings, H.Ikeda, E.Janke: Phys. Rev. Lett. 49 386 (1982).

[4.9].F.Keffer: Handbuch Der Physik 18II 1 (1966).

[4.10].C.Kittel: "Quantum Theory of Solids" (Wiley, New York, 1971).

[4.11].W.Marshall, S.W.Lovesey: "Theory of Thermal Neutron Scattering" (Oxford University Press, 1971).

[4.12].W.Hayes, R.Loudon: "Scattering of Light by Crystals" (John Wiley & Sons, 1978).

[4.13].R.J.Elliot, M.F.Thorpe: J. Phys. C: Solid St. Phys 2 1630 (1969).

[4.14].J.B.Parkinson: J.Phys. C: Solid St. Phys. 2 2012 (1969).

# Chapter 5

# Copper Oxide: A One-Dimensional Quantum Antiferromagnet ?

The work outlined in this chapter is a preliminary study of the spin-wave dispersion relation in copper oxide (CuO), performed using neutron scattering techniques at a reactor source. This was done to characterise the sample before using the high-energy neutrons available at a spallation source. Unfortunately, it has not yet been possible to carry out the high-energy neutron study due to scheduling problems at ISIS. Instead a Raman scattering study is reported, which tried to use light scattering techniques to probe the high-energy excitations via the two-magnon interactions. The chapter is set out as follows. There is a summary of the known properties of the antiferromagnet CuO given in section 5.1. Then the theory for a spin 1/2 one-dimensional antiferromagnet chain is discussed in section 5.2. Prior to the experimental sections, there is a synopsis of the samples used in section 5.3. Section 5.4 gives full details of the triple-axis spectrometer, HB3, and its configuration for this experiment. The neutron scattering results are presented in section 5.5, and section 5.6 gives a brief report of a Raman scattering study.

## 5.1 Introduction

There are many reasons related to recent developments in solid state physics for studying the magnetism in CuO. Most important is its relevance to both the field of high temperature superconductors and to quantum one-dimensional magnetism. Both are fields which have attracted much attention recently.

In the study of high temperature superconductors, it is widely believed that the magnetic coupling between $Cu^{2+}$ (S=1/2, L=2) ions via the $O^{-}$ ligand ion may be important

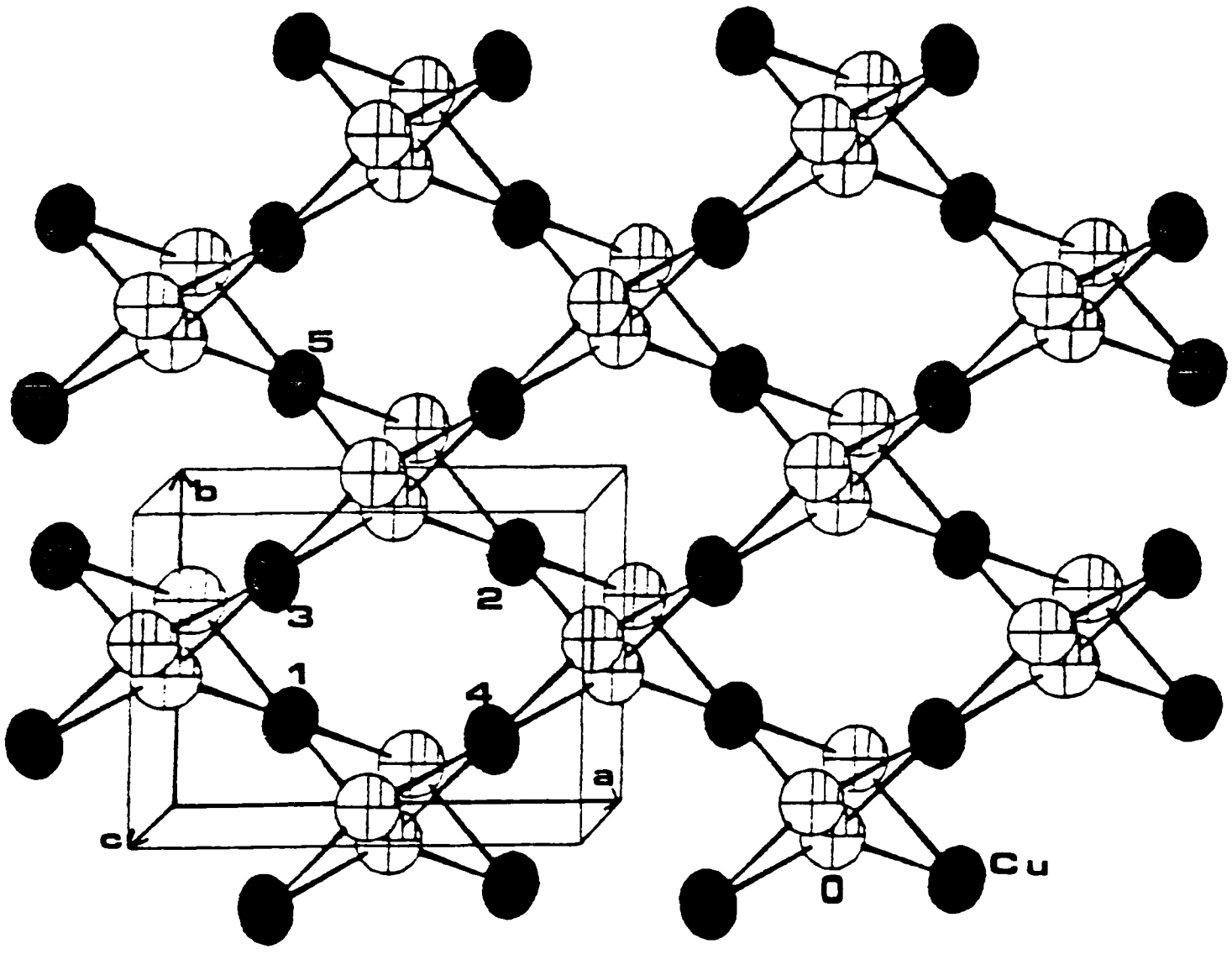


Figure 5.1a: The crystal structure of CuO.

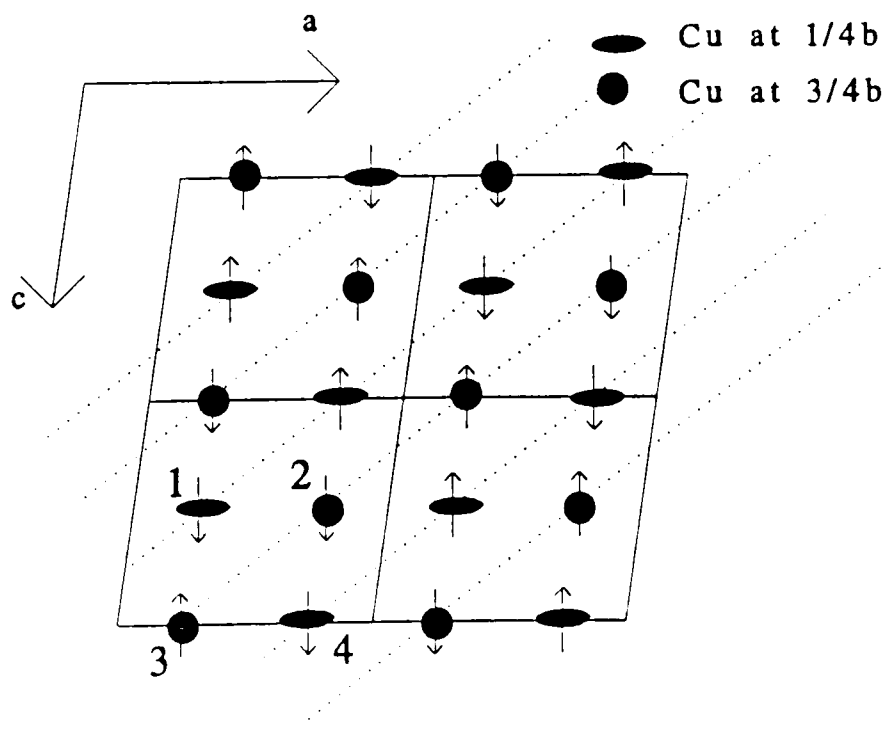


Figure 5.1b: Positions of copper ions projected on the (010) plane.

to the mechanism of the high temperature superconductivity[5.1]. Strong two-dimensional interactions have been found in the copper-oxygen planes in the cuprate superconductors leading to a renewed interest in two-dimensional magnetism, and also a need to study simple reference systems. CuO, with its $Cu^{2+}$ ions surrounded by a square planar arrangement of oxygens is thus an obvious candidate. Unlike the cuprate superconductors however, CuO does not have two-dimensional layers. Instead the square planar copper and oxygens form ribbons which run parallel to the [1 1 0] and the [1 -1 0] directions (figure 5.1).

The fact that $Cu^{2+}$ has S=1/2, also makes CuO an important system to study. Low-spin systems have behaviour which deviates from the classical predictions of linear spin-wave theory and recently there has been much interest in low-spin chains. For example, the discovery of a quantum continuum of states above the spin-wave dispersion relation in S=1/2 $KCuF_3$[5.2] has sparked a lot of interest in the field of quantum one-dimensional magnetism. CuO is similar in many ways to $KCuF_3$, and it is interesting to note that in this system too, the low dimensionality of the interactions, and the S=1/2 may lead to quantum fluctuation effects. These deviations from the classical dispersion relation are discussed in more detail in section 5.2.

The one-dimensionality in CuO has been predicted by the bonding of the magnetic $Cu^{2+}$ ions via the intervening $O^-$ ions. It is known that distorting the bond angle between the magnetic ions connected via a ligand ion from an angle of 180°, reduces the superexchange interaction along the direction of the distortion. This is a well known result[5.3] and plays an important role in the magnetic behaviour of CuO. The bond angles in this structure have been determined using x-ray diffraction techniques[5.4], and table 5.1 gives the values measured. The ions are labelled in figure 5.1.

**Table 5.1 Bond Angles in CuO.**

| Bond | $Cu_2$-O-$Cu_3$ | $Cu_1$-O-$Cu_4$ | $Cu_2$-O-$Cu_4$ | $Cu_2$-O-$Cu_5$ |
|---|---|---|---|---|
| Angle | 145.82° | 108.85° | 104.03° | 95.72° |

The results in table 5.1 suggest that the $Cu_2$-O-$Cu_3$ coupling should be the strongest, due to the fact that it is closest to 180°. The chain formed by the $Cu_2$-O-$Cu_3$ lies along the [1 0 -1] direction, and from the spin-wave dispersion relation measurements by Ain et al[5.5], this has been confirmed as the direction of strongest interaction. The exchange interaction along the [1 0 -1] direction was found to be twenty times larger than the exchange interactions along the [1 0 1] and [0 1 0] directions, suggesting this system might be a candidate for one-dimensional magnetism.

The earliest studies performed on CuO showed that at 230K there is an anomaly in the specific heat measurements[5.6] which coincides with the three-dimensional Néel transition temperature from an antiferromagnetic phase to a paramagnetic phase[5.7]. Since these initial studies on powdered samples, more detailed experiments have been carried out. Experiments which have been performed include susceptibility measurements[5.8], [5.9], specific heat[5.10] and neutron scattering work[5.11], [5.12], [5.13]. The bulk techniques have shown that the behaviour above $T_N$ is in agreement with models for low-dimensional systems rather than having classical paramagnetic behaviour[5.14]. The susceptibility in CuO for example, shows no large change at $T_N$ as expected classically, and is found to peak at around 500K. Using the Fisher-Bonner[5.15] prediction to model the susceptibility of a one-dimensional antiferromagnet, leads to an exchange interaction of 34meV in CuO, which is half that obtained from the neutron scattering studies. The Fisher-Burford model predicts that the exchange interaction is related to the peak in the susceptibility curve by the following equation

$$\frac{kT_{max}}{J} \approx 1.282. \qquad \textbf{(5.1)}$$

The specific heat measurements can also be fitted to low-dimensional models in the region above $T_N$. At and below this temperature, detailed specific heat measurements show evidence of two phase transitions one at $T_N$=230K, which is of second order, and one at 213K, which is first order[5.10]. Neutron powder work has shown that these temperatures correspond to changes in the magnetic structure. Between 230K and 213K an incommensurate antiferromagnetic magnetic phase is found with a wavevector (0.505, 0, -0.483), which locks

into the (1/2, 0, -1/2) structure at 213K[5.11]. (See chapter 9 for a discussion of incommensurate phases.) The low temperature structure has $Cu^{2+}$ magnetic moments of $0.55\mu_B$ lying parallel and antiparallel to the *b*-axis. This value of the magnetic moment is lower than expected for a $Cu^{2+}$ ion with a completely quenched orbital moment. In this case, with S=1/2 and g=2, the moment, $\mu=gS\mu_B$, would be expected to be approximately $1\mu_B$. This lowering of the moment could be due to zero-point fluctuations, which are important in low-dimensional magnetism.

In more recent years, the growth techniques for CuO samples have improved and it is now possible to grow large single crystals. This has made inelastic neutron scattering studies possible allowing the measurement of the spin-wave dispersion relation[5.5], [5.16]. As has already been discussed, Ain et al have measured the spin-wave dispersion relation along the chain direction [1 0 -1] and perpendicular to it. They obtained a value for the slope of the spin-wave dispersion relation along the chain direction of 550meVÅ. This was achieved by measuring the dispersion relation for energy transfers between 0 and 80meV. The slope of the dispersion relation is also known as the spin-wave velocity, *v*, and is related to the exchange constant in linear spin-wave theory (see equation 5.3) by

$$v=2Jd, \tag{5.2}$$

where *d* is the nearest neighbour separation in Å. For CuO along the chain direction d=3.74Å, and equation 5.2 thus gives the exchange constant as approximately J=80meV in the [1 0 -1] direction. In the perpendicular directions, slopes of 135meVÅ along the [010] direction, and 170meVÅ along the [101] direction were found. The value obtained for the slope of the dispersion relation along the chain direction [1 0 -1] is twice that of a previous study carried out by Yang et al[5.16], who predicted a spin-wave velocity of 250±75meVÅ (J=35meV). In that study the spin-wave branches could not be resolved due to the steepness of the dispersion relation, and only scans below an energy transfer of 8meV were measured. This lower value of spin-wave stiffness is however in agreement with the exchange constant obtained from susceptibility measurements.

Despite the strong suggestion from the susceptibility, specific heat and the dispersion relation studies that CuO should behave like a one-dimensional antiferromagnet, the neutron

scattering studies show that above the three-dimensional Néel temperature, $T_N$=230K, well defined spins waves are no longer observed. This is in contradiction to what is expected for a one-dimensional system which should not be affected by the three-dimensional ordering temperature but, should continue to have well defined excitations up to temperatures comparable with the exchange interaction energy- which for CuO would be about 800K.

In this chapter, the preliminary work carried out on the new CuO samples grown at the Clarendon is discussed. The aim of this study was to characterise the samples grown and to compare the results with the previous studies. The final objective, which has not yet been reached, is to measure the zone-boundary excitation along the chain direction. Since CuO is perhaps a one-dimensional, S=1/2 antiferromagnet, there is the possibility that a quantum continuum of states may be seen at these energies rather than a well defined cut-off. The reasoning behind this will be touched on in section 5.2. Instead, a Raman scattering study has been examined to look for the zone-boundary energy (see section 5.5). Time has also been allocated to perform such an experiment using spallation source neutron techniques on the HET instrument at the Rutherford Appleton Laboratory, but unfortunately it has not yet been performed.

## 5.2 Magnetic Excitations in One-Dimensional Spin 1/2 Chains

In this section results derived for one-dimensional S=1/2 chains are discussed. Principally, the underlying excitations in quantum chains are fundamentally different from the classical Bose excitations from a Néel state, and have fermion characteristics[5.17]. This leads to excitations which only occur in pairs, and these are often referred to as "spinons"[5.1]. In integer-spin systems binding of the spinons leads to a Haldane gap in the dispersion relation and the excitations are spin waves[5.18]. In the odd-half-integer systems these spinons are unbound and this changes the dynamical correlation function $S(\mathbf{Q},\omega)$, leading to a continuum of states[5.21]. For more details of the experiments performed and the theory developed see references [5.19], [5.20], [5.21].

The linear spin-wave theory introduced in chapter 4 is applicable to classical Heisenberg antiferromagnets. In CuO, S=1/2 and if it is also considered as being essentially

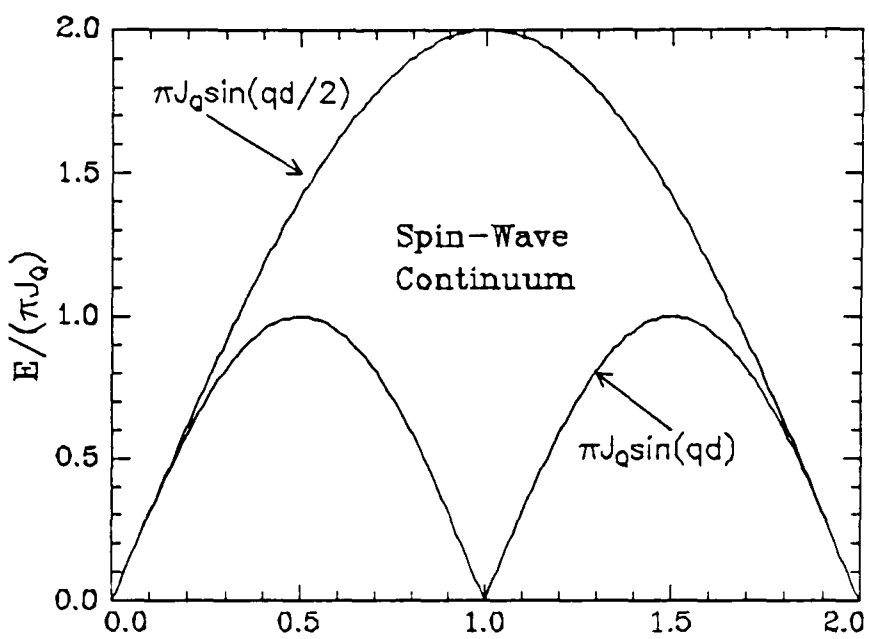


**Figure 5.2: The spin-wave continuum spectrum of the S=1/2 Heisenberg antiferromagnetic chain.**

one-dimensional, then classical linear spin-wave theory gives the dispersion relation as

$$E^{cl}(q)=2J_{cl}\sin(qd). \tag{5.3}$$

In equation 5.3, $J_{cl}$ is the nearest-neighbour exchange interaction along the chain direction, with q representing the reduced wavevector transfer in reciprocal lattice units, and d representing the nearest neighbour spacing along the chain direction. In the quantum regime the dispersion relation becomes

$$E^{Q}(q)=\pi J_{Q}\sin(qd). \tag{5.4}$$

This relationship was calculated by Des Cloizeaux and Pearson[5.22] and is qualitatively similar to the classical result (equation 5.3) except for the change in the coefficient from 2 to $\pi$. This renormalisation of the energy scale is due to quantum effects and is difficult to establish experimentally.

It has recently emerged that a better way to distinguish between the classical and quantum descriptions of one-dimensional Heisenberg chains is to study the lifetime of the excitations. When measuring the line shapes of excitations using neutron scattering techniques, these lifetime effects lead to asymmetric high-energy tails. These are thought to arise from purely quantum effects. Calculations have suggested that the Des Cloizeaux Pearson dispersion relation (equation 5.4) is in fact a lower bound for these quantum effects, with an upper bound given by

$$E^{U}=2\pi J_{Q}\sin\left(\frac{qd}{2}\right). \tag{5.5}$$

This leads to a dispersion relation as shown in figure 5.2. Between the lower and upper bound a spin-wave continuum of states is predicted.

A continuum of states has been measured in $KCuF_3$, which is a good example of a S=1/2 Heisenberg antiferromagnetic chain. In this system the chains are created by a large overlap of bonds along the chain direction, leading to a ratio of interchain to intrachain exchange interactions of 0.01. This is five times smaller than the ratio in CuO. In $KCuF_3$, at

$T>T_N$, well defined spin waves are still seen along the chain direction[5.27], even though the dispersion in the perpendicular directions becomes negligible, this is characteristic of a one-dimensional system. Also above the three-dimensional Néel temperature in $KCuF_3$, the one-dimensional quantum effects have been seen- with a continuum of states being detected at energies above the classical spin-wave branches. This continuum has also been measured well below the Néel temperature. In this low-temperature regime, the quantum fluctuations only become important at energies higher than the zone boundary of the dispersion perpendicular to the chain, which for $KCuF_3$ is of the order 10meV.

In CuO the dispersion perpendicular to the chains has a zone boundary energy of the order 80meV. Below the Néel temperature in CuO, 80meV is the lower bound for quantum effects. Detection of these quantum effects in CuO would confirm its description as a quantum one-dimensional antiferromagnet.

## 5.3 Sample Details

CuO has a monoclinic structure with the space group C2/c. The lattice constants at room temperature have been determined using x-ray powder techniques[5.4] and are shown in table 5.2.

**Table 5.2 Lattice Constants for CuO at Room Temperature.**

| a | b | c | β |
|---|---|---|---|
| 4.6837Å | 3.4226Å | 5.1288Å | 99.54° |

Here β is the monoclinic angle between the a and c axes.

All the CuO samples studied in this chapter are from the same batch grown at the Clarendon Laboratory. New growth techniques are being tested. This interest has been sparked by the desire to grow large superconducting samples. The method used involves a flux of BaO-CuO and produces crystals of both $BaCuO_2$ and CuO. A full description of the growth is given in reference [5.23]. The crystal chosen for the neutron scattering experiments

was the largest of the batch weighing 17.8g, with dimensions of 25x25x10mm. This was found to have a mosaic spread of 0.9°. The crystal was shiny black in appearance, but during the course of the studies was seen to deteriorate on the surface. Raman scattering studies (section 5.6) have shown that the surface contamination is due to the formation of the more stable $Cu_2O$. This surface contamination did not affect the neutron scattering measurements, but as is seen in section 5.6, it greatly hindered experiments using light scattering techniques.

## 5.4 The Neutron Scattering Experiment

The preliminary neutron scattering measurements on the CuO samples have been carried out using the triple-axis spectrometer, HB3, at the Oak Ridge National Laboratory. This spectrometer is located on a thermal neutron source which has a moderator temperature of 345K, giving a peak in the Maxwellian distribution of neutrons at E=30meV. This leads to a limited number of neutrons in the region above about 130meV resulting in difficulties in the measurement of the spin-wave dispersion relation at high-energy transfers. The dispersion relation was predicted by Ain et al to have a stiffness of 550meVÅ along the chain direction giving a zone-boundary energy using the classical approach (equation 5.3) of 160meV.

The sample was lined up with the **b**-direction perpendicular to the scattering plane in order that scans along the chain direction [1 0 -1] could be carried out. The sample was placed in a closed-cycle refrigerator unit with the purpose of performing temperature controlled experiments above and below the Néel temperature.

CuO has a steep dispersion relation along the chain direction and this means that the resolution[5.24] of the triple-axis spectrometer becomes a crucial factor in determining whether the spin-wave branches can be distinguished or not. When carrying out this experiment good resolution was essential, but a compromise had to be made against very tight resolution and neutron flux. This conflict arises especially at high energies where reactor sources have a low flux of fast neutrons.

A schematic diagram of a TAS instrument is shown in figure 2.2. This is the basis for the set-up at HB3, where the monochromator used was a beryllium crystal reflecting from the

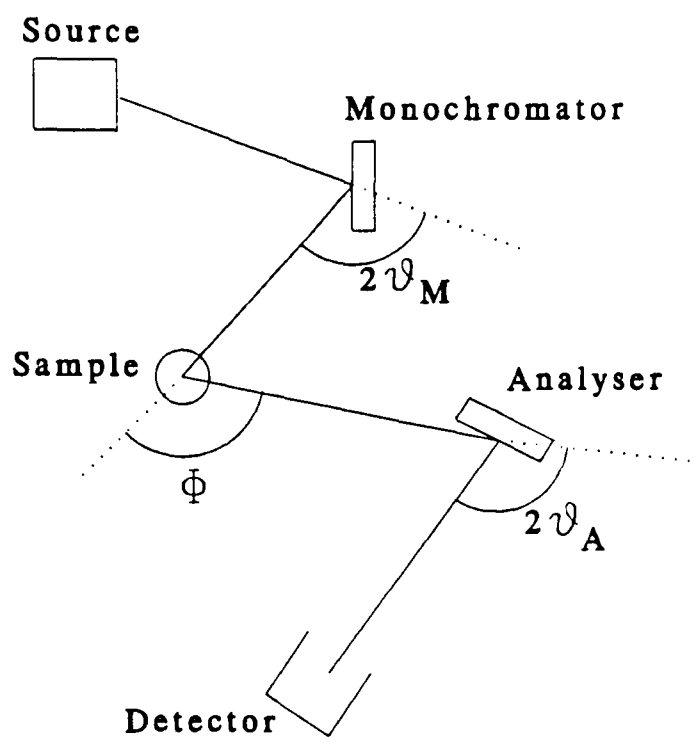


Figure 5.3a: Schematic diagram of a triple-axis spectrometer in the "w" configuration.

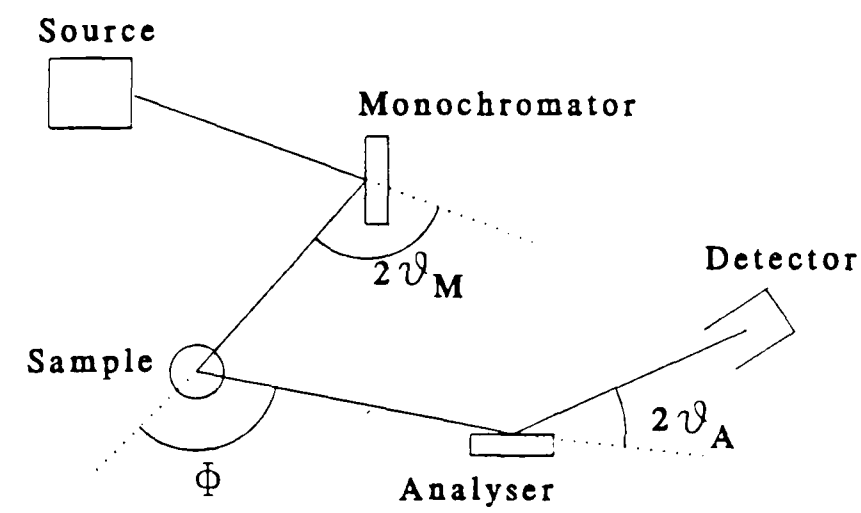


Figure 5.3b: Schematic diagram of a triple-axis spectrometer in the "u" configuration.

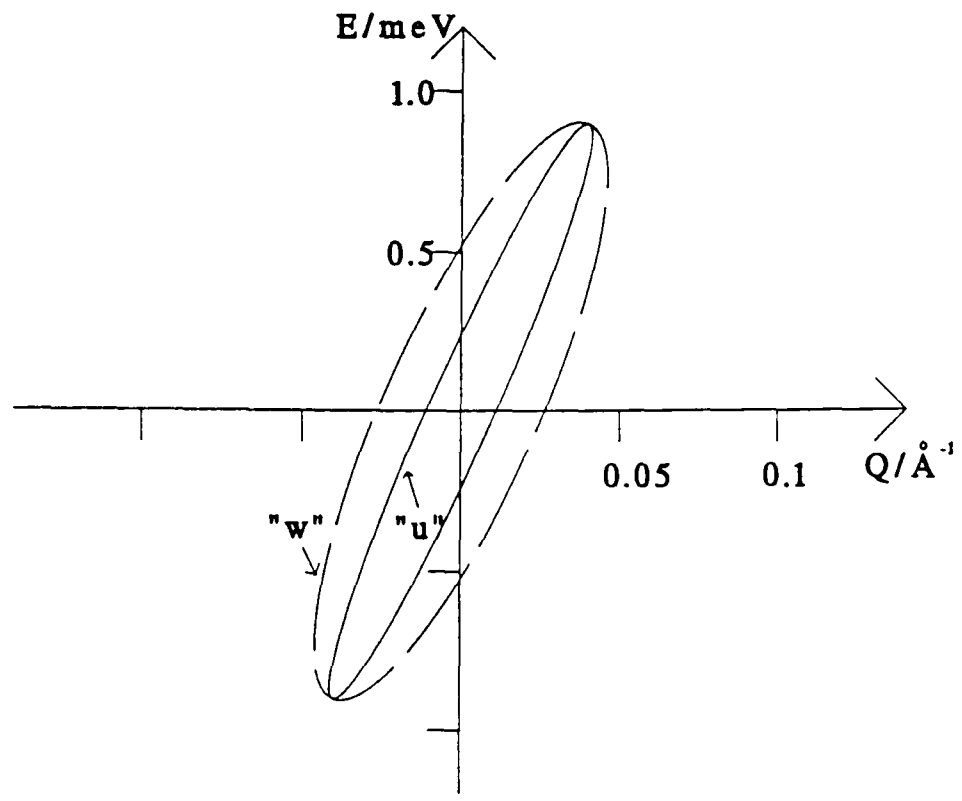


Figure 5.4a: The resolution ellipsoids for the "u" and "w" configurations of HB3.

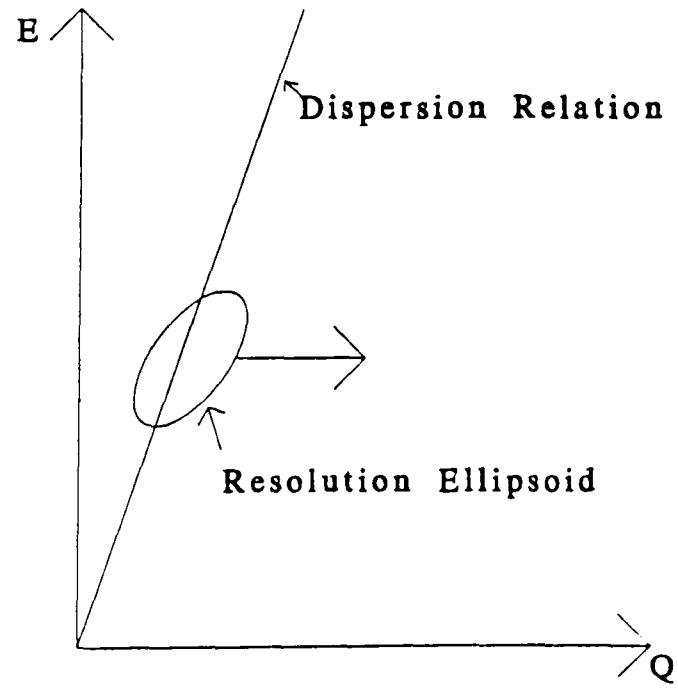


Figure 5.4b: Performing a Q scan through a dispersion relation.

(002)-plane, while the analyser crystal was the pyrolytic graphite (002)-plane. The horizontal collimation settings chosen at each energy transfer measured are shown in table 5.3.

**Table 5.3 Collimation and Scans Performed at HB3.**

| Energy Transfer (meV) | Final Energy (meV) | $Q_{centre}$ | Horizontal Collimation $H_1$-$H_2$-$H_3$-$H_4$ |
|---|---|---|---|
| 35 | 14.78 | (-1.5, 0, 1.5) | 40′-20′-40′-60′ |
| 50 | 25 | (2.5, 0, -2.5) | 40′-20′-50′-120′ |
| 55 | 27 | (2.5, 0, -2.5) | 40′-20′-50′-120′ |
| 80 | 37 | (2.5, 0, -2.5) | 40′-20′-50′-120′ |

Notice from table 5.3 that the collimation was increased for increasing energies. This was done to reduce the counting times by increasing the volume of the resolution ellipsoid and thus worsened the resolution. In fact the resolution is already deteriorated by measuring at large energy transfers. Thus in this situation resolution is lost on two counts. Even so, it was still possible to see resolved spin waves at an energy transfer of 80meV.

The HB3 instrument was found to be optimised for this dispersion relation in the "u" configuration shown in figure 5.3b, with figure 5.3a showing the "w" configuration. Using the standard resolution calculation program for triple-axis spectrometers RESCAL, this was found to give a narrower width in reciprocal space along the chain direction ($0.015Å^{-1}$ at 35meV settings) than the more conventional "w" set up ($0.034Å^{-1}$), see figure 5.4a. All the scans were taken using the "u" configuration. Figure 5.4b shows how the resolution ellipsoid cuts through a dispersion relation when performing a Q scan.

To collect the data to measure the spin-wave dispersion relation, the energy transfer was fixed for each scan and the wavevector transfer was varied along the direction of the one-dimensional chains [1 0 -1]. This was done because it gives better resolved spin waves than constant-Q scans, and is the preferred mode of operation for a steep dispersion relation. Here the final energy and initial energies were held constant, and thus no corrections are necessary

to take into account the energy dependence of the analyser crystal or for the detector efficiency. The fixed final energies for each scan are also shown in table 5.3.

It is desirable when carrying out neutron scattering experiments to use filters to reduce effects from second order scattering allowed by the monochromator. This is normally done using either a pyrolytic graphite or a beryllium filter as discussed in section 2.5. In this experiment a pyrolytic graphite filter was chosen for the lower energy transfers of E=25meV with the final energy fixed at $E_f$=14.78meV. At higher energies it was decided not to use the filter. This was so that $E_f$ could be fixed at a value roughly half of the energy transfer, E. Choosing the energies in these ratios helps to reduce background effects due to thermal diffuse scattering, which increases with increasing scattering angle[5.25]. Thus with no filter, higher energies were chosen being careful to avoid spurious counts due to second order effects. Also when choosing the energy transfers to study, care was taken to avoid energies close to phonon branches in CuO- as measured using inelastic neutron scattering techniques by W.Reichart et al[5.26].

A final point to note is the choice of reciprocal lattice vector that the dispersion relation was measured around. The magnetic form factor which arises in the scattering cross section (equation 2.20) has an approximate form which decays exponentially with the scattered wave vector as shown in equation 5.6.

$$|F(Q)|^2 \propto \exp -Q^2. \tag{5.6}$$

This means that it is desirable to measure wavevector transfers as close as possible to the origin to reduce the effects from the form factor, but so that the scattering triangle still closes. The wavevector transfers at the centre of the scans are shown in table 5.3 for a particular energy transfer.

By optimising all of the above conditions it is possible to measure well resolved spin waves in CuO with energies up to 80meV in a reasonable amount of time. The scans collected at 11K are shown in figure 5.5. This is the lowest temperature possible using the closed cycle refrigerator. Scans were also taken at 150K and two temperatures above the three-dimensional Néel temperature, $T_N$=230K. These are shown in figures 5.6-5.8. In the next

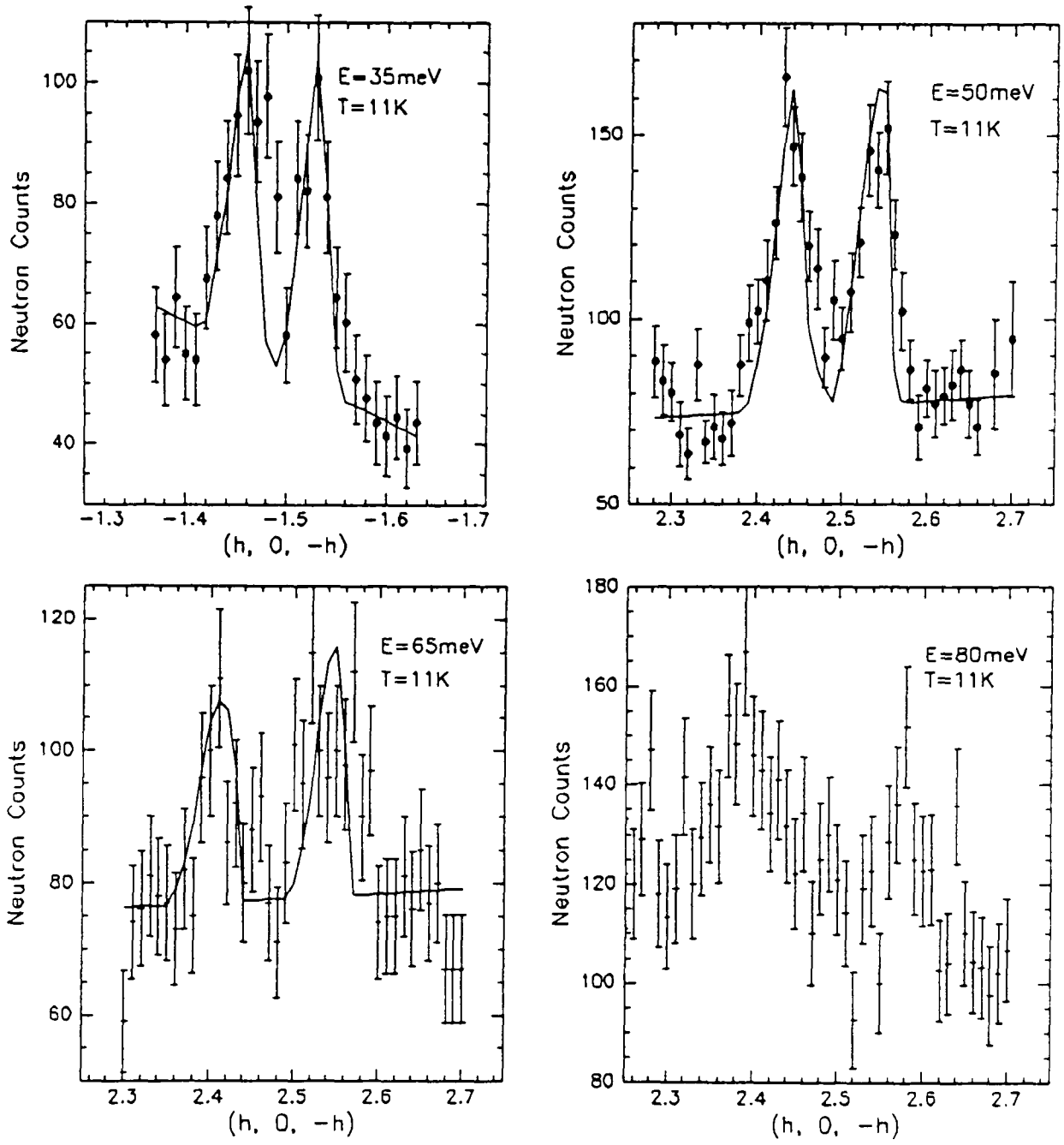


**Figure 5.5: The neutron scattering data collected using HB3 at 11K. The solid line represents the fits from RES90.**

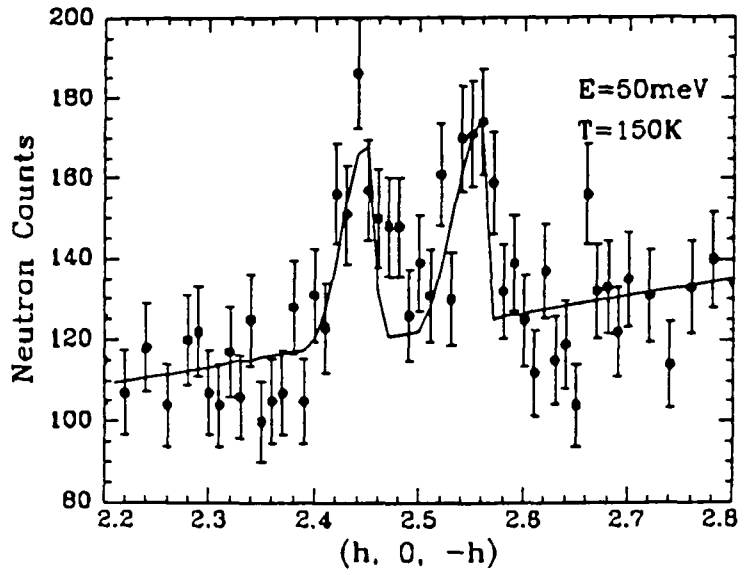


Figure 5.6: Spin waves in CuO at 150K. The solid line represents a fit using RES90.

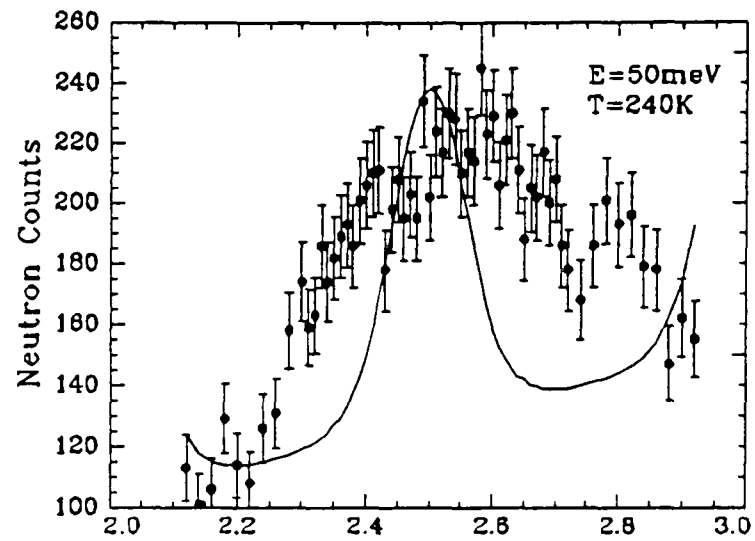


Figure 5.7: The spin waves in CuO above $T_N$. Notice they are no longer well defined. The solid line is the S=1/2 Heisenberg chain model.

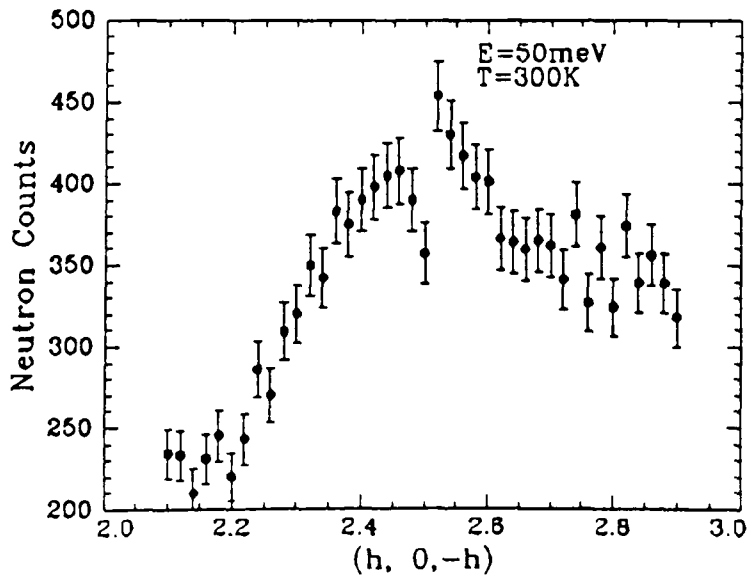


Figure 5.8: The spin waves in CuO at 300K.

section the analysis involved in fitting these scans is discussed.

## 5.5 Neutron Scattering Analysis

The data collected from the triple-axis spectrometer HB3 are shown in figures 5.5-5.8. To compare the data with a model dispersion relation (equation 5.7), a program based on the resolution calculations by Cooper and Nathans[5.24] was used. This program is called RES90 and was developed by R.Lloyd. The program requires the instrument parameters for each instrument setting to be input: ie horizontal collimation, vertical collimation, mosaic spreads and lattice constants. It then uses these parameters to calculate the resolution ellipsoid of the triple-axis spectrometer numerically and convolves this with a given dispersion relation, see figure 5.4b. The parameters common to all the scans are given in table 5.4

**Table 5.4 Fixed Parameters For Resolution Calculation**

| Vertical Divergence $V_1$-$V_2$-$V_3$-$V_4$ | Analyser Mosaic Spread | Monochromator Mosaic Spread | Sample Mosaic Spread |
|---|---|---|---|
| 0.73°-1.27°-2.2°-4.45° | 0.4° | 0.4° | 0.9° |

The dispersion relation for CuO using the notation developed in chapter 4 has the following form

$$E(q)^2=[2\{J_{101}+J_{010}-J_{10\bar{1}}\}-2\{J_{101}\cos\frac{1}{2}(q_a a+q_c c)+J_{010}\cos(q_b b)\}]^2 \\ -[2J_{10\bar{1}}\cos\frac{1}{2}(q_a a-q_c c)]^2. \qquad (5.7)$$

In equation 5.7, $J_{uvw}$ represents the exchange constants along the [uvw]-direction. Notice that in this equation $J_{101}$ and $J_{010}$ are positive because the exchange interactions between chains is ferromagnetic, while $J_{10\text{-}1}$ is negative due to the antiferromagnetic interactions along [1 0 -1]. Also note that the periodicity in q is such that the zone boundary of the antiferromagnetic dispersion relation is at (1/4, 0, -1/4), using the lattice constants as defined by the crystal structure (table 5.2). In the ferromagnetic directions the zone boundaries are at (1/2, 0, 1/2)

and (0, 1/2, 0). The exchange constants in the perpendicular directions were held fixed at the values calculated by Ain et al ($J_{101}$=5meV, $J_{010}$=3meV). The program assumes that there is no broadening of the spin waves due to damping.

The fits using the RES90 program at 11K and 150K are shown in figures 5.5 and 5.6, and the results of the fits are shown in table 5.5.

**Table 5.5 Results of the Fits to the Dispersion Relation.**

| T (K) | Energy Transfer (meV) | $J_{10\text{-}1}$ (meV) |
|---|---|---|
| 11 | 35 | -75±1 |
| 11 | 50 | -77±1 |
| 11 | 55 | -77±1 |
| 150 | 50 | -73±1 |

The average exchange energy obtained at 11K is -76.3±0.6meV and gives an average spin-wave stiffness constant of about 530meVÅ (using equation 5.2). This is in good agreement with the results of Ain et al who obtained a spin-wave stiffness constant along the chain direction of 550meVÅ ($J_{10\text{-}1}$=-80meV) at 40K. Notice that at 150K the spin-wave stiffness constant has softened as expected.

From figure 5.5 it is seen that the spin waves at 11K are still reasonably well resolved at 55meV, while at 80meV resolution effects have broadened the peaks. Above the Néel temperature, $T_N$=230K, figures 5.7 and 5.8 show what has happened to the spin-wave branches at 240K and 300K. Notice that there is no longer well defined spin-wave branches, and the remaining intensity is much broader than the original spin-wave branches. This is in contradiction to what was measured in the one-dimensional antiferromagnet $KCuF_3$ where in the region above $T_N$, the intensity remained at approximately the same width, with intensity filling in between the peaks due to quantum fluctuations as the three-dimensional ordering became less important. This theory has been compared to the CuO peaks in figure 5.7 using a program developed by D.A.Tennant[5.27] for $KCuF_3$, and showed that the quantum

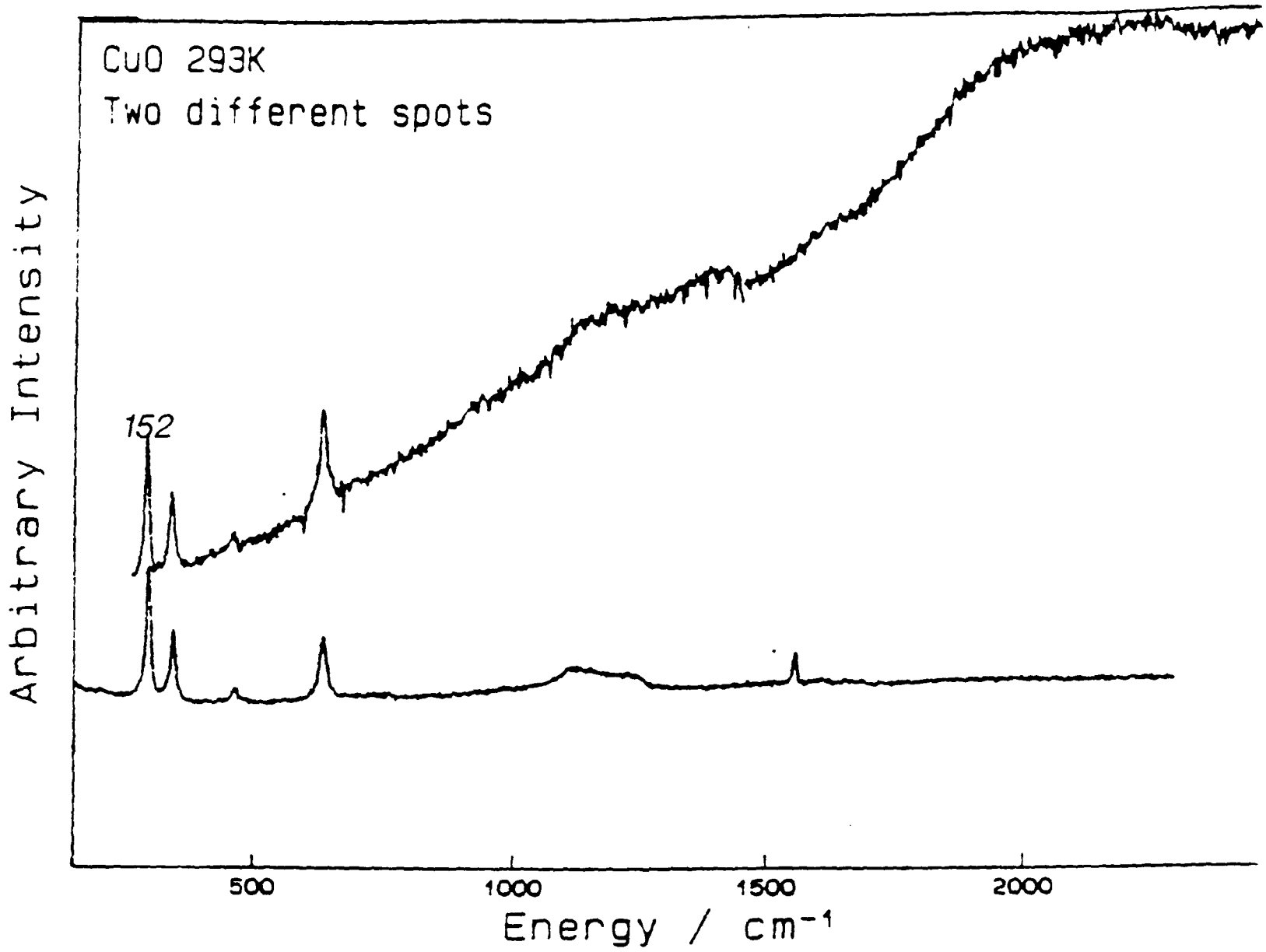


Figure 5.9: The Raman scattering from CuO at 293K. The two scans represent scattering from the same crystal at different positions.

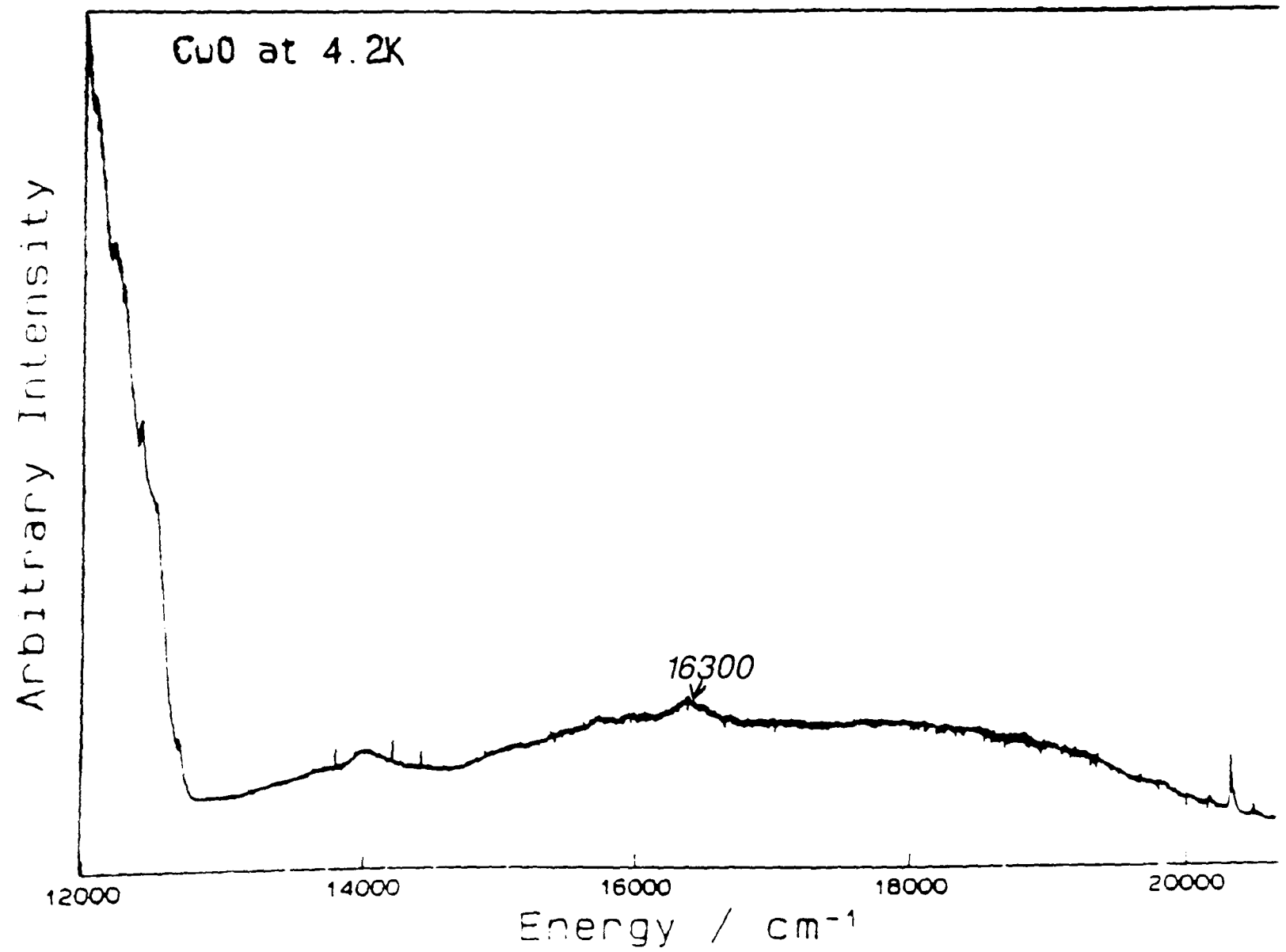


Figure 5.10: The Raman scattering from CuO at 4.2K. This shows broad contamination scattering. Notice the different scale from figure 5.9, this graph has not had the energy of the laser light removed. The energy is 21,042cm$^{-1}$ for the 476.5nm wavelength

model for one-dimensional chains is clearly inappropriate for CuO at $T>T_N$ for energy transfers of 50meV. These results are however in agreement with the previous neutron scattering experiments on CuO. It is possible that some of the increase in width is related to the incommensurate phase. This effect has been seen in rare-earth systems[5.28], and in CuO more careful measurements of the spin waves are required in this region.

## 5.6 Raman Scattering

In the absence of high-energy neutrons, Raman scattering has been attempted on CuO to measure the high-energy excitations. As discussed in chapter 4, Raman scattering can be used to measure two-magnon processes. The predicted two-magnon spectrum has been calculated for CuO using the theory developed by Elliot and Thorpe[5.29], and the result was shown in figure 4.3. Notice the difference between this spectrum and that calculated for $KFeF_4$ in section 4.2.4. In that case, magnon interactions moved the peak from twice the zone-boundary energy of the one-magnon dispersion, to a value of order 95% of this classical cut-off. In CuO, due to the small spin and the reduced number of nearest neighbours, the peak in the two-magnon spectra is much lower than the non-interacting prediction, and is in fact of the order 30%. Notice that the even though the peak may have shifted from the non-interacting prediction, there will be no scattering from two-magnon processes above that limit. In this case, the limit of the two-magnon scattering is at about 320meV ($4J_{cl}$), using the value of exchange constant extracted from a classical fit to the dispersion relation.

A Raman scattering experiment was thus performed on CuO in order to test this classical prediction for a one-dimensional antiferromagnet. The experiment was carried out in collaboration with another group at the Clarendon Laboratory using their Raman spectrometer. This is a triple-grating spectrometer using an argon ion laser (488nm and 514nm) to excite the sample, and a CCD camera to detect the scattering. The experiments were carried out in standard reflection geometry using unpolarised light. The samples were mounted in a continuous flow cryostat. These were cleaved immediately before placing them in the sample holder, to reduce deterioration time. However, it was found that the samples were contaminated with $Cu_2O$ which caused structural peaks at low energies, and had a large luminescence peak at high energies. For example, the first peak in figure 5.9 at 152cm$^{-1}$

corresponds to a phonon peak for $Cu_20$ as predicted by Reimann et al[5.30], while the luminescence peak for $Cu_2O$ at 16,300$cm^{-1}$ is marked in figure 5.10. This luminescence peak was more clearly seen in some of the room temperature scans. Also if the laser spot was moved across the sample impurity scattering was found, which caused a large increase in the background scattering. These effects are shown for the room temperature scans in figure 5.9. The problems of deterioration of the samples and of contamination have been seen by many other groups performing light scattering experiments on CuO. One group who carried out photoluminescence studies showed the single crystal samples deteriorating after 5 hours[5.31]. Due to the difficulties in lining up the sample and collecting data over such a large energy range, the Raman scattering experiments carried out at the Clarendon were taking at least 12 hours. Thurler et al[5.32] noted the presence of $Cu_2O$ in their data, when performing photoemission studies on oxidised-copper foil.

With all these problems the only available scan below the Néel temperature is shown in figure 5.10. Notice in this scan the effective zero is at 21,042$cm^{-1}$ i.e. the energy of the laser light. If the broad scattering feature evident in this scan was due to the two-magnon scattering predicted in figure 4.3 it would be expected to cut off at energies around 18,500$cm^{-1}$. This is clearly not the case, and it is therefore concluded that this broad feature is due to surface contamination. Unless there is some way to produce purer samples of CuO, and an effective way is found to stop the surface becoming $Cu_2O$, a Raman scattering study to predict the cut-off in two magnon processes seems almost impossible.

Irwin et al have performed a Raman scattering experiment on a CuO powder sample, in which they found well defined scattering between 1500$cm^{-1}$-2800$cm^{-1}$, with a peak at around 2100$cm^{-1}$ (250meV). This feature was seen at 15K, but not at room temperature. This could possibly be due to two magnon scattering, although it is at energies twice that predicted in section 4.2.4, which suggested a peak around 96meV (ie 30% of 320meV). A possible explanation for this larger than expected value of the peak in the Raman data is that instead of two excitations occurring on the same chain, perhaps the magnon-magnon interactions are occurring on neighbouring chains.

## 5.7 Conclusions

Using inelastic neutron scattering techniques, spin waves along the [1 0 -1] direction in CuO have been measured. Spin waves with energy transfers between 35 and 80meV have been studied, and these give a slope of the dispersion relation in the chain direction as 530meVÅ. This is in good agreement with previous studies. Above the Néel temperature well defined spin waves are no longer apparent, suggesting that CuO is paramagnetic in this region. This is in contradiction to what one would expect for a one-dimensional antiferromagnet. No evidence has been seen for the quantum fluctuation effects which have been found in $KCuF_3$.

Raman scattering has been attempted on these samples of CuO to try to study the high energy excitations which could not be reached using thermal neutrons. It was found that sample deterioration and contamination from $Cu_2O$ made these measurements very difficult, and thus it has not been possible to study the zone boundary excitations in CuO.

## 5.8 Further Work

More work is planned for CuO using spallation neutron techniques. These will not be affected by surface contamination, as was the case for Raman scattering. On the HET instrument at the Rutherford Appleton Laboratory, where the time is scheduled, it should be possible to reach the energy transfers required to measure the zone-boundary energy in CuO, predicted at 160meV. By using energy transfers larger than the energies of the perpendicular dispersions, it will be possible to determine whether CuO does in fact behave like a quantum one-dimensional antiferromagnet, or whether the interchain interactions are so large that the system behaves like a three-dimensional system.

## References

[5.1].P.W.Anderson: Science 235 1196 (1987).

[5.2].S.E.Nagler, D.A.Tennant, R.A.Cowley, T.G.Perring, S.K.Satija: Phys. Rev B44 12361 (1991).

[5.3].P.W.Anderson: Phys. Rev. 79 350 (1950).

[5.4].S.Asbrink, L.J. Norrby, Acta Cryst. B26 8 (1970).

[5.5].M.Ain, W.Reichard, B.Hennion, G.Pepy, B.M.Wanklyn: Physica C162-164 1279 (1989).

[5.6].H.Jih-Heng, H.L.Johnston: J.Amer.Chem.Soc: 75 2417 (1953).

[5.7].B.N.Brockhouse: Phys Rev 94 781 (1954).

[5.8].M.O'Keefe, F.Stone: J.Phys.Chem.Solids 23 261 (1962).

[5.9].C.B.Azzoni, A.Paleari, G.B.Parravicini: J.Phys: Condes. Matt. 4 1359 (1992).

[5.10].J.W.Loram, K.A.Mirza, C.P.Joyce, A.J.Osborne: Europhys. Letts. 8 263 (1989).

[5.11].J.B.Forsyth, P.J.Brown, B.M.Wanklyn: J.Phys.C: Solid State Phys. 21 2917 (1988).

[5.12].P.J.Brown, T.Chattopadhyay, J.B.Forsyth, V.Nunez, F.Tasset: J.Phys.: Condens. Matt 3 4281 (1991).

[5.13].M.Ain, A.Menelle, B.M.Wanklyn, E.F.Bertaut: J.Phys: Condens. Matt. 4 5327 (1992).

[5.14].L.J. de Jongh, A.R.Miedema: Adv. Phys. 23 1 (1973).

[5.15].J.C.Bonner, M.E.Fisher: Phys. Rev A135 640 (1964).

[5.16].B.X.Yang, T.R.Thurston, J.M.Tranquada, G.Shirane: Phys. Rev. B39 4343 (1989).

[5.17].A.M.Tsvelik: Phys. Rev. B45, 486, (1992).

[5.18].I.Affleck: J.Phys. Cond. Matt. : 1 3047 (1989).

[5.19].D.A.Tennant, T.G.Perring, R.A.Cowley: Phys. Rev. Lett 70, 4003 (1993).

[5.20].L.D.Faddeev, L.A.Takhtajan: Phys. Lett.85A 375 (1981).

[5.21].H.J.Schulz: Phys. Rev B34 6372 (1986).

[5.22].J.Des Cloizeaux, J.J.Pearson: Phys. Rev 128 2131 (1962).

[5.23].C.Changkang, H.Yingle, B.M.Wanklyn, J.W.Hodby: Jnl. Cryst. Growth 129 239 (1993).

[5.24].M.J.Cooper, R.Nathans: Acta Cryst. 23 357 (1967).

[5.25].G.E.Bacon: Neutron Diffraction (Oxford University Press, 1955).

[5.26].W.Reichart, F.Gompf, M.Ain, B.M.Wanklyn: Z.Phys. B- Condens. Matt. 81 19 (1990).

[5.27].D.A.Tennant: D.Phil Thesis, Oxford University (1994).

[5.28].J.Jensen, A.R.MacKintosh: "Rare Earth Magnetism, Structures and Excitations" (Oxford University Press, 1991).

[5.29].R.J.Elliot, M.F.Thorpe: J.Phys. C: Solid State Phys 2 1630 (1969).

[5.30].K.Reimann, K.Syassen: Phys. Rev. B39 11113 (1989).

[5.31].Z.X.Shen, R.S.List, D.S.Dessau, F.Parmigiani, A.J.Arko, R.Bartlett, B.O.Wells, I.Lindau, W.E.Spicer: Phys. Rev. B42 8081 (1990).

[5.32].M.R.Thuler, R.L.Benbow, Z.Hurych: Phys. Rev B26 669 (1982).

# Chapter 6

# Spin Waves in the Two-Dimensional Antiferromagnet $KFeF_4$

This chapter describes the first of three studies on the layered structure $KFeF_4$, and deals with the measurement of the spin-wave dispersion relation using neutron scattering techniques. The spin-wave dispersion relation has been studied to characterise fully the magnetic interactions below the Néel temperature. Section 6.1 explains why there is an interest in two-dimensional magnetism. This is followed in section 6.2 by details of the structure and magnetism of $KFeF_4$. The application of linear spin-wave theory to $KFeF_4$ is outlined in section 6.3. The experimental details are discussed in section 6.4, while the results are presented in section 6.5. These results are then used to calculate the form of the two-magnon Raman scattering and this is compared to experimental measurements. Section 6.6 investigates the temperature dependence of the zone-centre gap energy, and the results are compared to the temperature dependence of the staggered magnetisation.

## 6.1 Introduction

The magnetic behaviour of a system depends upon both the dimensionality and the nature of the magnetic interactions. Layered antiferromagnets with the $K_2MnF_4$ structure are excellent examples of two-dimensional systems with relatively simple magnetic interactions[6.1]. Linear spin-wave theory has proved to be a very successful model for the spin-wave dispersion relation. The model incorporates a Heisenberg exchange interaction between nearest neighbours within the planes and a small Ising anisotropy to simulate the effect of dipolar interactions or crystal-field effects. Close to the phase transition, the critical properties are dominated by the Ising behaviour with two-dimensional Ising-model exponents being obtained[6.2]. However, at higher temperatures this is not the case and the layered antiferromagnets are found to have crossed over from Ising behaviour to behaviour dominated

by the two-dimensional Heisenberg interactions[6.3]. The two-dimensional Heisenberg model has recently attracted considerable theoretical attention because it is found to be an appropriate model for the undoped cuprate systems. Chakravarty et al[6.4] have developed a theory for the two-dimensional quantum Heisenberg antiferromagnet (QHAF) based on a renormalisation of the classical model developed by Shenker and Tobochnik[6.5]. This QHAF has successfully described the experimental results from both $La_2CuO_4$ (S=1/2)[6.4] and $K_2NiF_4$ (S=1)[6.3].

All the studies in this chapter have been carried out below $T_N$: in chapter 8 the nature of the critical fluctuations above $T_N$ are described and compared with those predicted by the various two-dimensional models. The purpose of this study was to characterise the magnetic properties of the analogous system $KFeF_4$, which has S=5/2 and so approximates more closely the classical spin model. This was done by measuring the spin-wave dispersion relation at 50K and 100K, and comparing the measurements to linear spin-wave theory predictions, as introduced in chapter 4. Once the magnetic interactions have been examined a study of how these affect the critical behaviour has been undertaken. The bulk of the work carried out on the phase transition is described in chapter 8, although some preliminary work is mentioned here. A detailed temperature study has been performed on the gap at the zone centre of the dispersion relation. This gap arises from anisotropy effects, which in $KFeF_4$ are not fully accounted for. Section 6.6 compares these measurements of the temperature dependence of the spin-wave gap frequency to that of the sub-lattice magnetisation. They are both found to have the same temperature dependence and both are characteristic of two-dimensional Ising behaviour.

## 6.2 Structure and Magnetism of $KFeF_4$

$KFeF_4$ has a layered structure in which the $Fe^{3+}$ ions lie in the *ab*-planes and each $Fe^{3+}$ ion is surrounded by six $F^-$ ions forming an octahedra[6.6]. The ground state of the $Fe^{3+}$ ion has S=5/2 and L=0. The anisotropy effects confine the magnetic moments to lie parallel to the *c*-axis. The layers containing the $Fe^{3+}$-$F^-$ octahedra are separated from each other by a layer of non-magnetic $K^+$ ions, with each layer being staggered from the next along the *b*-axis by 1/4**b**, leading to weak magnetic interactions between nearest-neighbour layers[6.7].

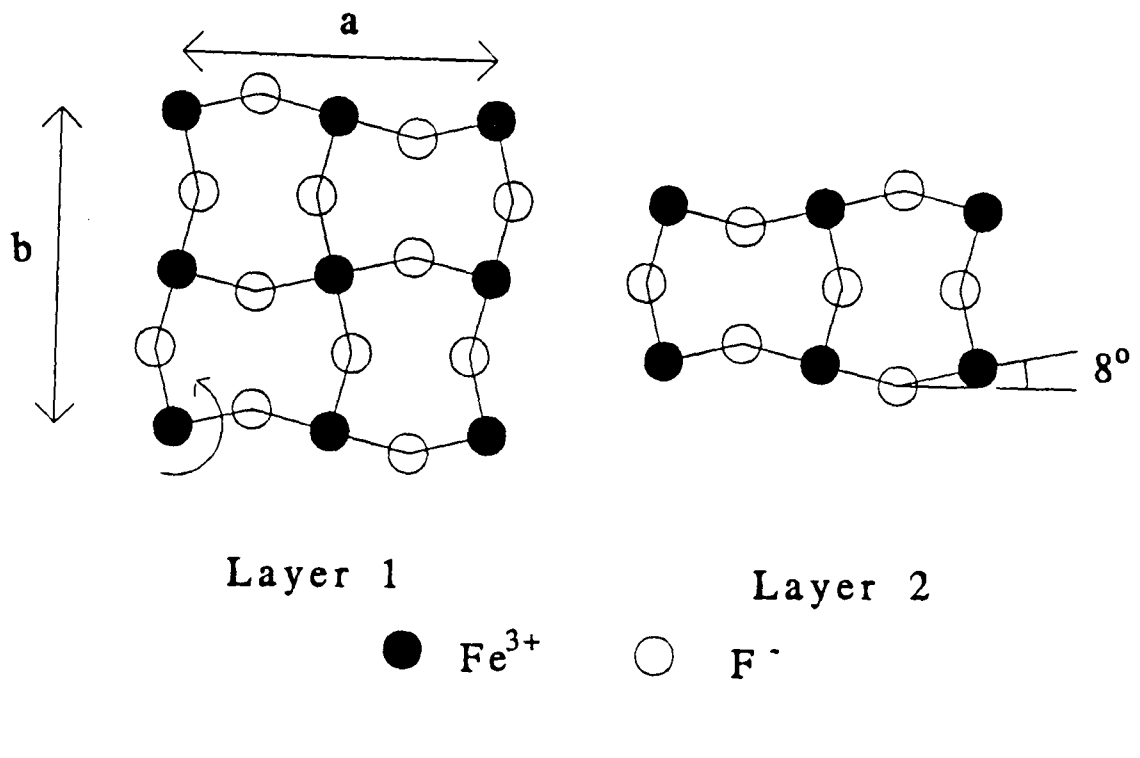


Figure 6.1: A diagram of the ab-plane in $KFeF_4$.

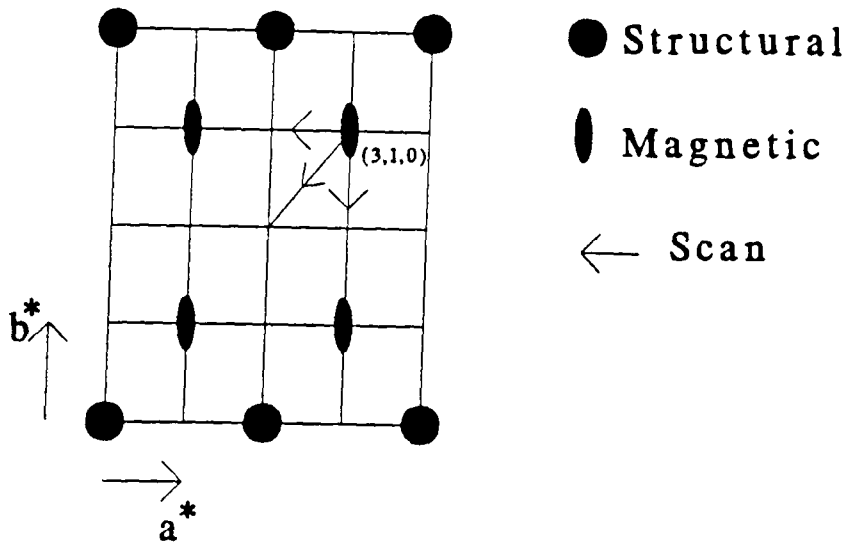


Figure 6.2: The (hk0) reciprocal lattice plane. The points shown are the strong structural and magnetic peaks.

The intralayer magnetic interactions are much smaller than the interlayer interactions, the ratio being of the order $10^{-4}$[6.7], and thus $KFeF_4$ can essentially be thought of as a two-dimensional antiferromagnet, similar to the $K_2MnF_4$ structures.

Whereas the $K_2MnF_4$ structures are tetragonal, $KFeF_4$ is orthorhombic, this is because the fluorine octahedra are tilted out of the plane along the **a** direction at an angle of 11.64° to the horizontal[6.6] as shown in figure 6.1. This tilting leads to a doubling of the of the unit cell along the *a*-axis. Below 400K there is a further distortion of the system caused by a rotation of the octahedra about the c-axis by 8° with the consequence of doubling the unit cell along the *b*-axis. This leads to a space group of *Pcmn* and lattice constants at 50K of $a$=7.564Å, $b$=7.750Å and $c$=12.27Å. The structural and magnetic lattice constants are identical in this system due to the distortion in the crystal structure. Figure 6.2 is a diagram of the reciprocal lattice for the *ab*-plane in $KFeF_4$. The details of the structure have been studied by x-ray scattering[6.8] and are consistent with Raman scattering measurements[6.9]. In chapter 9, there is a detailed study of the structural phase transition in $KFeF_4$ using x-ray techniques. It should be noted that the mechanism that drives the structural phase transition is independent of the magnetic phase transition.

## 6.3 Application of Linear Spin-Wave Theory

When modelling the spin-wave dispersion relation the distortion due to the octahedra rotation has been allowed for by having two different nearest-neighbour exchange energies: one along the **a** and the other along the **b**-direction. In order to align the spins in their preferred direction along the crystallographic *c*-axis an Ising anisotropy term has also been included in the Heisenberg Hamiltonian. Using the theory developed in chapter 4[6.10], the dispersion relation for a two-dimensional antiferromagnet with nearest-neighbour and next-nearest-neighbour interactions is

$$\begin{aligned} E_q^2=&[g\mu_b H_A-4S(J_1+J_2)+8SJ_3 \\ &-4SJ_3(\cos\frac{1}{2}(q_x a+q_y b)+\cos\frac{1}{2}(q_x a-q_y b)]^2 \\ &-[4S(J_1\cos\frac{1}{2}(q_x a)+J_2\cos\frac{1}{2}(q_y b))]^2. \end{aligned} \qquad \textbf{(6.1)}$$

Equation 6.1 represents the energies of the spin waves with wave vector **q**. $J_1$ and $J_2$ are the nearest-neighbour exchange interactions in the **a** and **b** directions respectively, and are the exchange interactions between spins on opposite sublattices. $J_3$ is the next-nearest neighbour interaction and occurs between spins on the same sublattice. Remember that the exchange energies have been defined such that J is negative if the interaction is antiferromagnetic, and positive for ferromagnetic interactions. The effective field due to the anisotropy effects is represented by $H_A$ and this acts along the crystallographic *c*-axis.

Previous studies on $KFeF_4$ have measured an anisotropy energy that was larger than predicted from dipole-dipole interactions alone. As discussed by de Wijn et al[6.15], the anisotropy due to dipole effects has the following form

$$H_{DD}=\frac{\mu_o}{4\pi}\frac{3}{2}g\mu_b S\left(\Sigma_{ll'}\frac{1}{R_{ll'}^{\ 3}}-\Sigma_{lm}\frac{1}{R_{lm}^{\ 3}}\right), \qquad \textbf{(6.2)}$$

where $R_{lm}$ is the separation of atoms on opposite sublattices, and $R_{ll'}$ is the separation of atoms on the same sublattice. This leads to a dipole-dipole anisotropy energy in $KFeF_4$ of $g\mu_b H_{DD}$=0.033meV. This is of order four times smaller than the anisotropy previously measured, see table 6.3. Thus other explanations must be thought of to account for this discrepancy. This is an anomalous result, since in the analogous $Rb_2MnF_4$ ($Mn^{2+}$, S=5/2, L=0) dipole-dipole calculations do fully account for the anisotropy found[6.15].

In certain structures extra anisotropy effects may result in a canting of the moments from the easy axis. These effects have been seen in $La_2CuO_4$[6.18], where the canting tilts the spins out of the basal plane. Canting effects can exist only in structures where the magnetic and structural unit cells are identical and where the magnetic moments are parallel at the lattice sites related by translational or inversion symmetry[6.10]. In such systems, weak ferromagnetism is found due to canting of the moments. These effects are normally small, and typically change the direction of the moments by only a few degrees. The distortion of the crystal structure by the rotation of the $F^-$-octahedra means that the above conditions are satisfied by $KFeF_4$. If the extra anisotropy in $KFeF_4$ results in canting effects, this would cause a splitting of the spin-wave branch. The theory predicts that this is splitting is largest

at the zone centre of the dispersion relation. Using the theory discussed in reference [6.18] for $La_2CuO_4$, the zone centre frequencies in $KFeF_4$ would become

$$E_1(0)=\sqrt{2g\mu_b H_{DD}4S(J_1+J_2)} \tag{6.3}$$

and

$$E_2(0)=\sqrt{(g\mu_b H_{CANT})^2+2g\mu_b H_A(4S(J_1+J_2))}\,. \tag{6.4}$$

Note that $E_1(0)$is similar to the zone-centre frequency obtained without canting effects, except that the general anisotropy field along the *c*-axis, $H_A$, is replaced by the dipole-dipole anisotropy field, $H_{DD}$. In $KFeF_4$, this leads to a zone-centre energy of 1.2meV. The extra effect of the canting arising from $H_{CANT}$ would lead to a higher energy zone-centre energy. There is currently no evidence for any splitting of the spin-wave branches in $KFeF_4$.

## 6.4 The Experimental Set Up

The $KFeF_4$ crystal was grown at the Clarendon Laboratory using the flux-growth method[6.11]. The crystal was a plate 11mmx7mmx2mm and contained two crystallites 2° apart. The mosaic spread in the *ab*-plane was found to be 0.5°. Figure 6.3 shows a rocking curve of the sample taken using neutron scattering techniques.

The neutron-scattering experiments were performed at the I.L.L. in Grenoble using the triple-axis crystal spectrometer IN3. The thermal neutron source has a moderator temperature of 300K, with a peak in the Maxwellian distribution at a neutron wavelength of 1.2Å, corresponding to an energy of 57meV. A copper monochromator was used to select the initial neutron energy, and a pyrolytic graphite analyser defined the scattered energy. Details of these crystals are given in table 6.1. The scattered neutron energy was held fixed at 14.7 meV and a pyrolytic graphite filter on the scattered side was used to reduce scattering by higher order neutrons. On IN3 the neutrons are detected using $^3$He detectors.

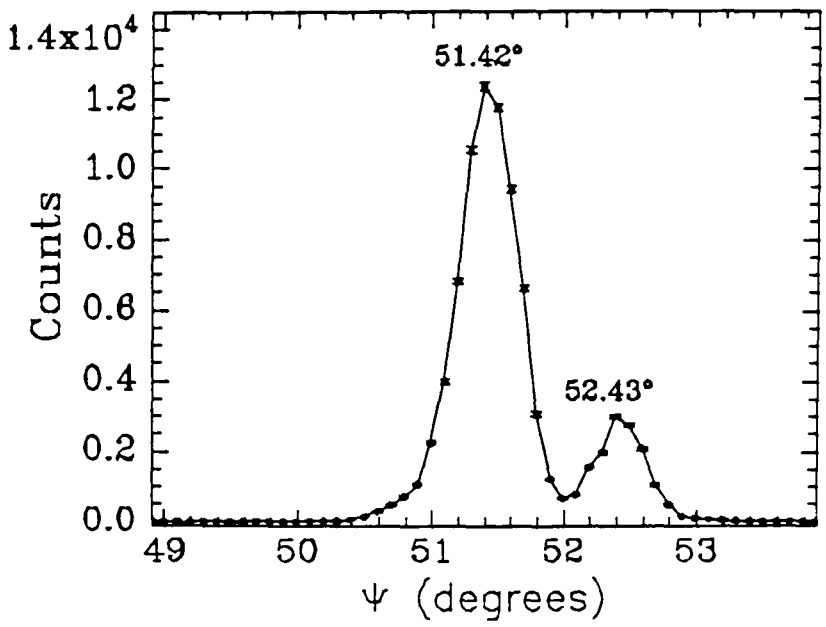


**Figure 6.3: The rocking curve for the (4,0,0) Bragg peak at 50K.**

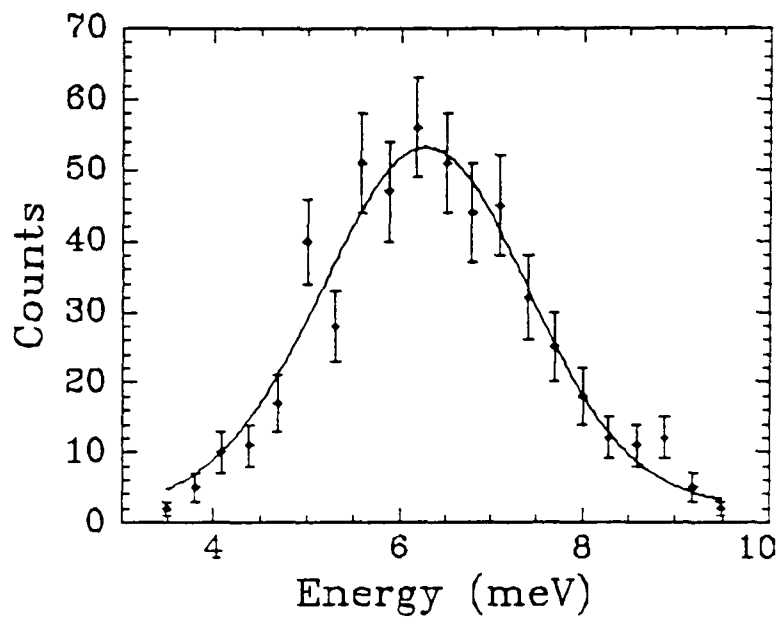


**Figure 6.4: Measuring the energy of the spin wave at a fixed wavevector transfer Q=(2.925,0.925,0), with q=(0.075, 0.075, 0). The line is a fit to a Gaussian.**

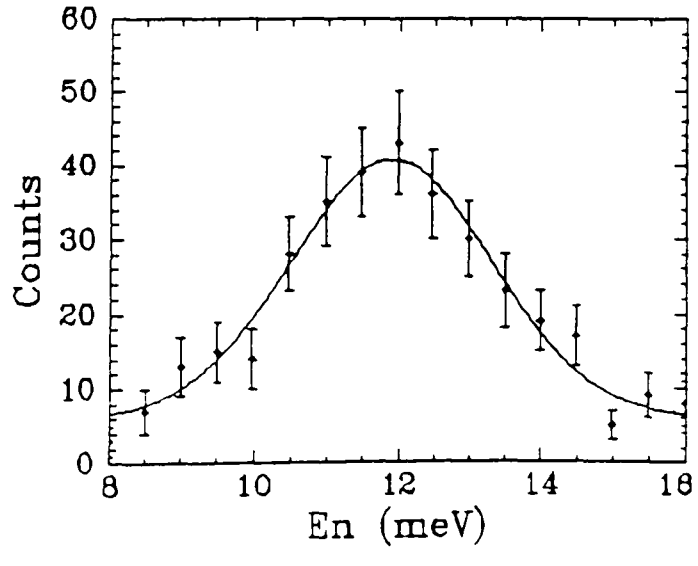


**Figure 6.5: Measuring the spin wave energy at a fixed wavevector transfer Q= (2.75, 1, 0), with q=(0.25,0,0). The solid line is a fit to a Gaussian.**

**Table 6.1 Monochromator and Analyser Crystal Parameters.**

| Crystal | d (Å) | Mosaic | Energy Range (meV) |
|---|---|---|---|
| Cu (111) | 2.088 | 0.33° | 5-50 |
| PG (002) | 3.355 | 0.59° | 2-20 |

The collimation of the instrument when measuring the dispersion relation was set at 20′ before the monochromator, 40′ between the monochromator and sample, 40′ between the sample and analyser and 40′ between the analyser and detector. This was changed to 20-′20′-20′-30′ to take the data for the temperature dependence of the anisotropy gap and the staggered magnetisation. It was possible to tighten the resolution for these measurements because of the large intensity of a magnetic Bragg peak. The crystal was placed in an orange cryostat in order that temperature control experiments could be performed to within an accuracy of ±0.01K. The crystal was aligned in the cryostat with the *c*-axis perpendicular to the beam so that spin waves propagating in the *ab*-plane could be examined.

## 6.5 Measuring the Spin-Wave Dispersion Relation

In the following sections are details of the spin-wave dispersion relation measured in $KFeF_4$ using neutron scattering techniques. Section 6.5.1 describes how the data to measure the dispersion relation was collected and analysed. Once the dispersion relation has been measured it is fitted to the predictions of linear spin-wave theory in section 6.5.2. Section 6.5.3 explains the relative magnitudes of the nearest-neighbour exchange constants extracted from the fits using simple arguments based on superexchange. Then in section 6.5.4, the magnitude of the anisotropy energy is compared with previous studies, and dipole-dipole calculations. Finally in section 6.5.5, the dispersion relation calculated from this neutron scattering data is used to evaluate the two-magnon Raman spectrum, and this is compared with some experimental data.

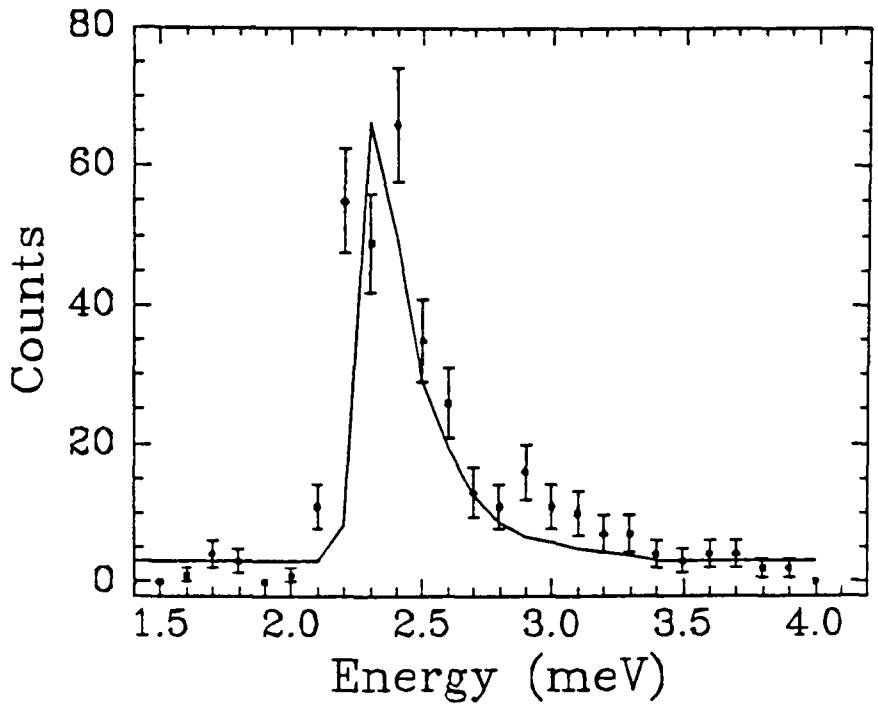


**Figure 6.6: Measuring the spin wave energy at the zone centre (1,1,0). The solid line is a fit from RES90.**

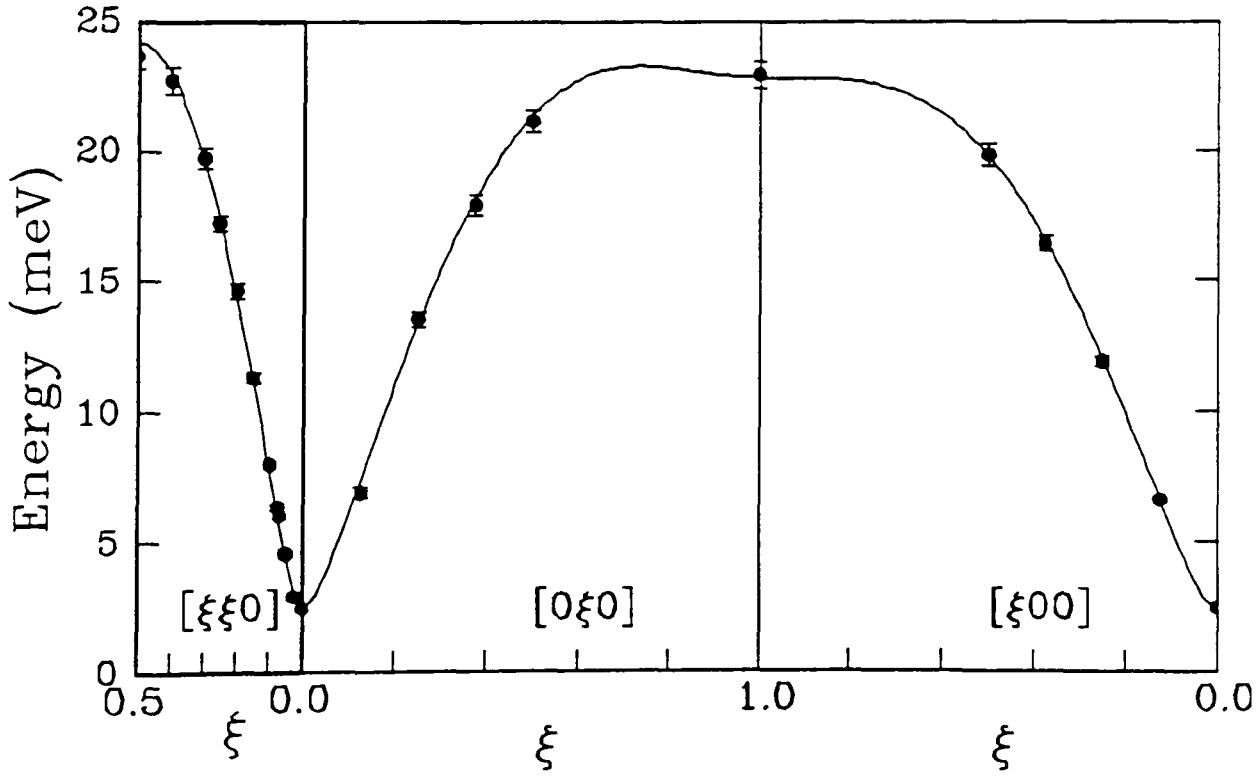


**Figure 6.7: The spin-wave dispersion relation in $KFeF_4$ at 50K. The line represents a fit to linear spin-wave theory, equation 6.1.**

## 6.5.1 Data Collection and Analysis

The spin-wave dispersion relation in $KFeF_4$ was determined using a neutron triple-axis spectrometer by performing a series of constant-Q scans i.e. fixing the wavevector transfer, **Q**, and scanning the energy transfer, E. The **q** vector of the spin wave used in equation 6.1 is related to the wavevector transfer by $\mathbf{q}=\mathbf{Q}-\tau$, where $\tau$ is the nearest reciprocal lattice vector. The scans were taken around the (3,1,0) magnetic reciprocal lattice points for the dispersion relation data. This lattice point was chosen as it is close to the origin, thus reducing form-factor effects which decrease the intensity of the spin-wave scattering. It was not possible to optimise this factor by taking scans around the (1,1,0) reciprocal lattice point: the energy transfers required to measure the full dispersion relation could not be reached using 14.7meV neutrons. The spin waves were determined for three propagation directions [$\xi$ $\xi$ 0], [$\xi$ 0 0 ] and [0 $\xi$ 0 ], at 50K, in order that the difference in exchange interactions in the **a** and **b** directions could be modelled. $\xi$ is the reduced wave vector, which for the **a** direction is given by $q_x a/2\pi$, and similarly for the **b**-direction, $q_y b/2\pi$. Data were also collected at 100K for the [$\xi$ $\xi$ 0]-direction only.

The spin-wave energies were determined by fitting the energy scans to Gaussians, examples of the data are shown in figures 6.4-6.6. Scans taken at the zone centre are not well described by a single Gaussian because resolution effects cause an asymmetric line shape, as shown in figure 6.6. These scans were initially fitted to a two-Gaussian model, with the results being confirmed with a more rigorous approach using the RES90 program as discussed in chapter 5. This program convolves the dispersion relation, equation 6.1, with the resolution function of the triple-axis spectrometer IN3. For the $KFeF_4$ data this full convolution to determine all the spin-wave energies was not considered necessary, because the spin-waves are well defined, and only the peak positions were required. This was not the case for CuO in chapter 5, because measuring well-defined spin waves was difficult.

## 6.5.2 The Resulting Dispersion Relation

The resulting dispersion relation is shown in figure 6.7 and the solid line represents the best fit to the experimental data given by equation 6.1. Two fits to the data at 50K were made, one

including only the nearest-neighbour interactions and the other allowing for nearest and next-nearest-neighbour interactions. Fits to the 100K data allowed only for nearest-neighbour interactions. Values for the exchange constants calculated from the fits are shown in table 6.2.

**Table 6.2 Results of the Fits to the Dispersion Relation.**

| T | $J_1$ (meV) | $J_2$ (meV) | $J_3$ (meV) | $g\mu_b H_A$ (meV) | $\chi^2$ |
|---|---|---|---|---|---|
| 50K | -1.05±0.01 | -1.34±0.02 | - | 0.123±0.003 | 1.94 |
| 50K | -1.13±0.04 | -1.39±0.03 | 0.06±0.02 | 0.116±0.004 | 1.72 |
| 100K | -1.20±0.03 | -1.20±0.03 | - | 0.01 (fixed) | 6.99 |

For the 100K data it was not possible to distinguish between $J_1$ and $J_2$ and thus both are equal with a value of -1.20meV. For the 50K data the differences were detectable due to the fact that the dispersion relation had been measure along more than one direction. Taking an average from the two 50K fits it is found that $J_1$ =-1.09±0.02meV, $J_2$=-1.37±0.02meV, with the next-nearest-neighbour interaction being of the order twenty times smaller. The magnitude of the anisotropy effect will be discussed in section 6.5.4. The results are in good agreement with previous studies as shown in table 6.3.

**Table 6.3 Results for Nearest-Neighbour Exchange Constants from Previous Studies.**

| Experiment | $J_1=J_2$ (meV) | $g\mu_b H_A$ (meV) |
|---|---|---|
| Neutron Data[6.12], 15 K | -1.22 | 0.11 |
| Two-Magnon Raman[6.16], 2 K | -1.16 | 0.1 |
| Susceptibility[6.13] | -1.15 | 0.11 |

Calculating the differences in the nearest-neighbour exchange constants in the **a** and **b**-directions were not possible from these studies. To explain the differences measured in this study of $KFeF_4$ simple arguments involving superexchange interactions have been employed.

### 6.5.3 Superexchange

The results from the fits to the dispersion relation at 50 K show a surprisingly large difference in nearest-neighbour exchange constants $J_1$ and $J_2$: it is thought that this arises because of the different superexchange paths in the **a** and **b**-directions due to the tilting of the fluorine ions out of the plane in the **a** direction[6.6]. This effect would make $J_1$ (along **a**) smaller than $J_2$ (along **b**), even though the lattice constant *a* is smaller than *b*. This result can be qualitatively understood by the superexchange theory of Anderson[6.14]. The superexchange interaction in $KFeF_4$ occurs through the p-electrons of the $F^-$ ligand, and the strongest coupling occurs when the magnetic ions are diametrically opposite. By using simple geometric arguments and considering only the change in the overlap of the wavefunctions as the bond angle between the magnetic ions changes, relations between the undistorted exchange path in the **b**-direction, $J_2$, and $J_1$ in the distorted **a**-direction have the form

$$J_1 = J_2 \cos^4\theta, \tag{6.5}$$

or possibly

$$J_1 = J_2 \cos^2(2\theta), \tag{6.6}$$

where $\theta$=11.64°, and is the angle of tilt from the horizontal. This results suggest that if $J_2$ is equal to -1.37meV, $J_1$ would be -1.25meV (equation 6.5) or -1.15meV (equation 6.6) instead of the measured -1.09meV. These simple geometric arguments do not fully account for the exact difference in the exchange energies, but do explain why there is a reduction of an appropriate order of magnitude.

### 6.5.4 Anisotropy

The experimental value for the anisotropy energy $g\mu_b H_A$=0.12meV, obtained from the fits to the dispersion relation, is approximately four times larger than expected from dipolar interactions (0.033meV)[6.15]. This is in excellent agreement with other studies done on $KFeF_4$ (table 6.3), and thus there must be other contributions that should be taken into account when calculating $H_A$, which are not important in the analogous $Rb_2MnF_4$ with S=5/2

ions[6.15]. At present there is no convincing explanation for this difference. It has been suggested by Abdalian et al[6.16] and by Desert[6.12] that the additional anisotropy may be related to residual $Fe^{2+}$ ions present in the crystal. However, all the studies using different samples have found similar values for the extra anisotropy. Also, in $K_2FeF_4$[6.17] the preferred orientation for the $Fe^{2+}$ (S=2, L=2) spins within a fluorine octahedra environment is along the [110] axis, i.e. in the plane, which would tend to lower the anisotropy trying to align the spins along the *c*-axis not increase it. Another possibility is that the distorted tetragonal structure of $KFeF_4$ gives rise to anisotropic exchange interactions of the Dzialoshinski form as found in $LaCuO_4$[6.18]. As discussed in section 6.3 such interactions would give rise to a splitting of the spin-wave energies. Careful high-resolution measurements were performed to search for such splitting, which from equations 6.3 and 6.4 would be of the order 1meV. The measurements were performed with a configuration described in section 6.4. The results are shown in figure 6.6 together with a simulation of the expected profile for a dispersion relation without canting effects. This was done using the resolution convolution program RES90. Clearly the data contains no evidence for any splitting, in agreement with a similar study carried on the same crystal by Desert et al[6.12]. It is thus not understood why $H_A$ is larger than would be expected for dipolar interactions. In section 6.6 there is a study of the temperature dependence of the anisotropy effect.

### 6.5.5 Comparison with the Two-Magnon Raman Scattering

In the two-magnon Raman scattering study carried out at 2K by A.T.Abdalian et al[6.16] it was noted that the exchange constant extracted from the Raman profile was 4% smaller than the exchange constant obtained from the same sample using neutron scattering techniques at 15K[6.12]. In that neutron scattering study the dispersion relation was only measured in one direction [110], and thus the different exchange interactions in the **a** and **b** directions were not seen. The simulations of the Raman profile[6.19], [6.20] have been repeated using the exchange constants obtained from this neutron scattering experiment at 50K, which gave different exchange constants along the **a** and **b** directions, in order to see if this accounted for the discrepancy. The details of the calculation are given in chapter 4. A comparison of the simulation with data is shown in figure 6.8. It is clearly seen that taking

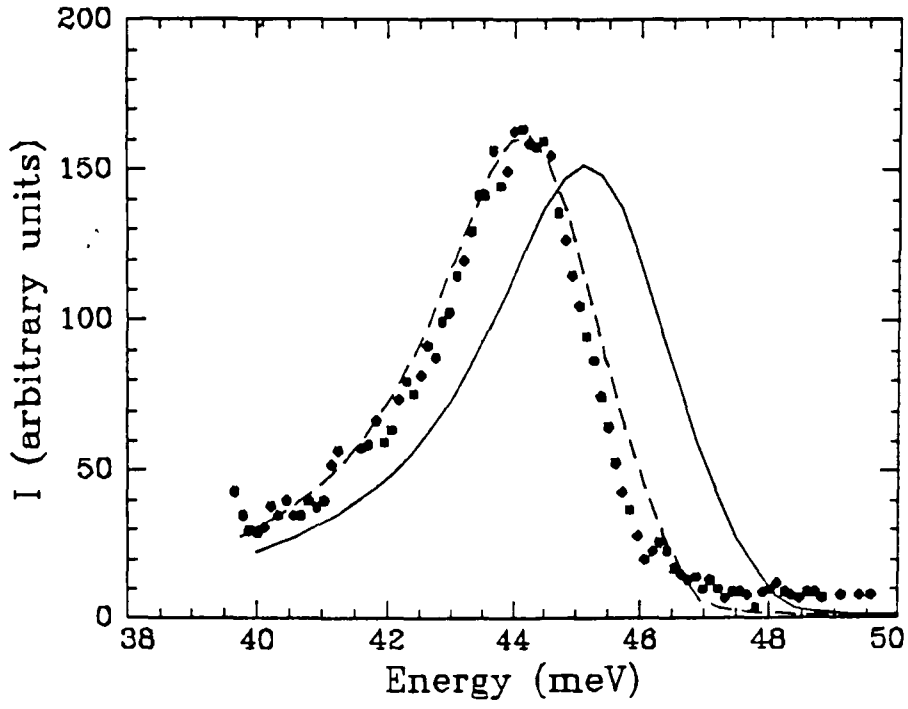


Figure 6.8: Comparing Raman data with theory using the dispersion relation measured here (solid line). The dashed line represents the original fit by Abdalian et al.

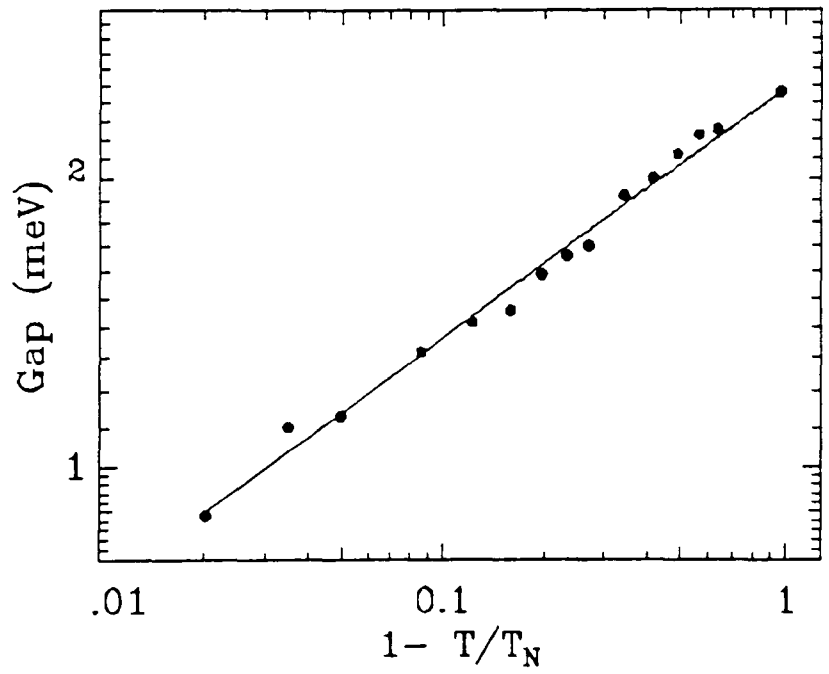


Figure 6.9: The temperature dependence of the anisotropy gap. The solid line is a fit to power law behaviour, equation 6.7.

into account the different exchange constants in the **a** and **b**-directions does not account for the 4% discrepancy in the value of the exchange constant extracted from the Raman data, and thus it is not clear why this difference arises.

## 6.6 Temperature Dependence of the Anisotropy and the Staggered Magnetisation Below $T_N$

The temperature dependence of the anisotropy effect that causes the gap in the dispersion relation at the magnetic zone centre was measured using the experimental set up described in section 6.4. It is thought that an understanding of how the anisotropy changes with temperature will help in determining the origin of the extra anisotropy. The data was collected keeping the wavevector transfer Q fixed at the zone centre (1,1,0) and scanning the energy transferred to the system, keeping the final energy fixed by the analyser at 14.7meV. The peak energy of the spin waves at the zone centre were extracted form the data by fitting the data to Gaussians, as discussed in section 6.5.1. The results are shown in figure 6.9 along with power-law fits to the data, using equation 6.7 where

$$Y = B\left(\frac{T_N - T}{T_N}\right)^C . \qquad (6.7)$$

The parameters extracted from these fits are shown in table 6.4.

**Table 6.4 The Results of the fits to Power-Law Behaviour**

| | c | $T_N$(K) | $\chi^2$ |
|---|---|---|---|
| anisotropy gap | 0.26±0.01 | 137.0±0.5 | 2.8 |
| (1,1,0) integrated intensity | 0.26±0.01 | 137.0±0.3 | 2.3 |

Measurements of the integrated Bragg intensity of the magnetic reflections were also collected at various temperatures below $T_N$ in order that the temperature dependence of the

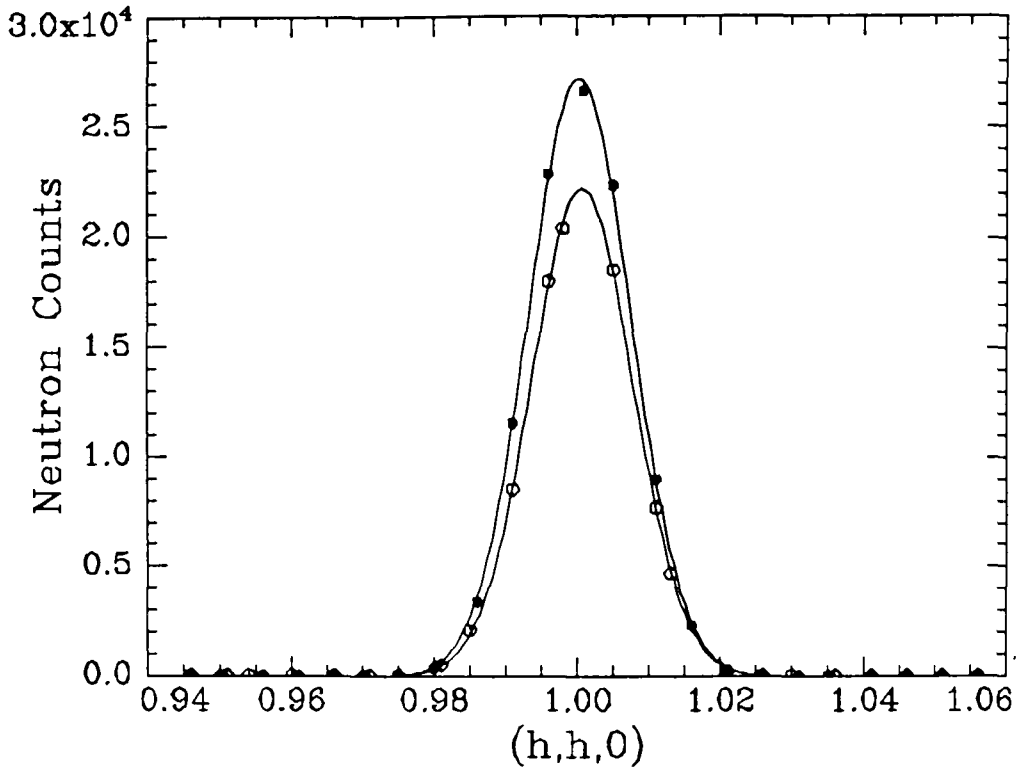


**Figure 6.10: Measuring the integrated intensity of the (1,1,0) magnetic Bragg peak at T=60K (filled circles) and T=105K (open circles).**

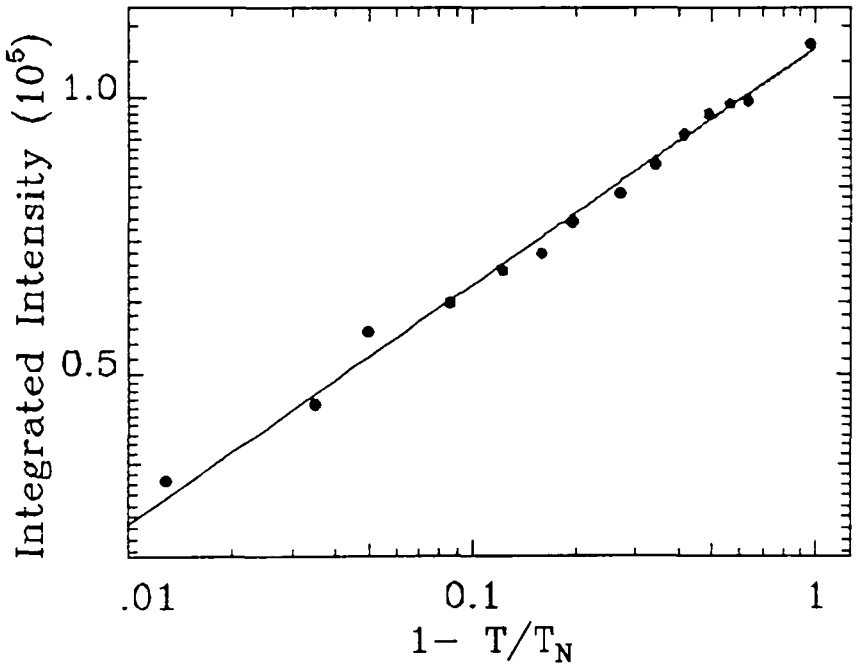


**Figure 6.11: The temperature dependence of the integrated intensity of the (1,1,0) magnetic Bragg peak. The solid line is a fit to equation 6.7.**

magnetic order parameter could be examined. The integrated intensity of the magnetic Bragg peaks is proportional to the square of the staggered magnetisation, which is predicted to have power-law behaviour with a critical exponent $2\beta$ (see chapters 7 and 8 for more details). To measure the integrated intensity, the Bragg reflections were scanned in wavevector transfer along [110] as shown in figure 6.10. Note, each scan was taken using the same incident monitor count (M=20, corresponding to ~15s), thus reducing fluctuation effects from the source. The results of the integrated intensity temperature dependence are shown in figure 6.11 along with a fit to the power-law behaviour given by equation 6.7.

A comparison of the results from the two fits is given in table 6.4. It is seen that the anisotropy gap varies in the same way as the integrated intensity of the (1,1,0) magnetic Bragg peak, which has $c=2\beta$. $\beta$, the critical exponent arising from the staggered magnetization temperature dependence, is 0.125 for a two-dimensional Ising system[6.21]. Similar behaviour is also found in the analogous layered systems $Rb_2MnF_4$[6.15] and $K_2NiF_4$[6.22] ($Ni^{2+}$, S=1, L=3). However, in $K_2NiF_4$ dipole-dipole effects do not fully account for the anisotropy, and crystal-field effects had to be considered. These are not important in $KFeF_4$ because the $Fe^{3+}$ ions have a L=0 ground state, and so this mechanism cannot be used to explain the extra anisotropy in this situation.

## 6.7 Conclusions

The spin-wave excitations in $KFeF_4$ are well described by a two-dimensional spin Hamiltonian incorporating nearest-neighbour and next-nearest-neighbour exchange interactions, and an anisotropy term. The different superexchange paths along **a** and **b** directions produce a nearest-neighbour exchange $J_1$=-1.09±0.02meV along **a**, that is smaller than $J_2$=-1.37±0.02meV along **b**. These values of the exchange constants cannot account for the discrepancies found in the Raman scattering studies. In agreement with other studies on KFeF4, the dipole-dipole interactions are insufficient to explain the anisotropy energy measured, $g\mu_b H_A$=0.12meV at 50K. The anisotropy gap varies in the same way as the square of the staggered magnetisation and the temperature dependence of the magnetisation shows strong two-dimensional behaviour, with the data below $T_N$ predicting $\beta$ of the order of the two-dimensional Ising model.

## References


[6.1].R.J.Birgeneau, H.J.Guggenheim, G.Shirane: Phys. Rev B8 304 (1973).

[6.2].R.J.Birgeneau, J.Als-Nielsen, G.Shirane: Phys.Rev B16 280 (1977).

[6.3].R.J.Birgeneau: Phys.Rev B41 2514 (1990).

[6.4].S.Chakravarty, B.I.Halperin, D.R.Nelson: Phys.Rev B39 2344 (1989).

[6.5].S.H.Shenker, J.Tobochnik: Phys.Rev B22 4469 (1980).

[6.6].G.Heger, R.Geller: Solid State Comm. 9 335 (1971).

[6.7].L.J.deJongh, A.R.Meidema: Adv.Phys. 23 1 (1974).

[6.8].P.Sciau, D.Grebille: Phys.Rev B39 11982 (1989).

[6.9].A.Desert, A.Bulou, J.Nouet: J.Phys: Conds. Matt. 4 1023 (1992).

[6.10].F.Keffer: Handbuch Der Physik 18II 103 (1966).

[6.11].B.M.Wanklyn: Jnl. Mat. Scn. 10 1487 (1975).

[6.12].A.Desert, A.Bulou, J.Noet: Solid State Comm 83 505 (1992).

[6.13].M.Eibschutz, G.R.Davidson, H.J.Guggenheim: AIP Conf. Proc 5 670 (1972).

[6.14].P.W.Anderson: Phys.Rev. 79 350 (1950).

[6.15].H.W.deWijn, L.R.Walker,R.E.Walsted: Phys.Rev.B 8 285 (1973).

[6.16].A.T.Abdalian, A.Desert, C.Dugaulier, A.Bulou, P.Moch, J.Nouet: J.Mgn.Mgn.Mat. 104-107 1047 (1992).

[6.17].M.P.H.Thurlings, E.Frikkee, H.W.deWijn: J.Mgn.Mgn.Mat. 15-18 369 (1980).

[6.18].C.J.Peters, R.J.Birgeneau, M.A.Kastner, H.Yoshizawa, Y.Endoh, J.Tranquanda, G.Shirane, Y.Hidaka, M.Oda, M.Suzuki, T.Murakami: Phys Rev B37 9761 (1988).

[6.19].R.J.Elliot, M.F.Thorpe: J.Phys. C2 1630 (1960).

[6.20].J.B.Parkinson: J.Phys C2 2012 (1969).

[6.21].M.Collins: "Magnetic Critical Scattering" (Oxford University Press 1989).

[6.22].R.J.Birgeneau, F. De Rosa, H.J.Guggenheim: Sol.State Comm. 8 13 (1970).

# Phase Transitions

# Chapter 7

# Phase Transitions and Critical Phenomena

In the remaining chapters of this thesis the emphasis shall focus on phase transitions. Two experiments have been performed which fall into this category, and both have been carried out on $KFeF_4$. The first continues the study of the magnetic properties of this low-dimensional antiferromagnet, and concentrates on studying the nature of the magnetic phase transition in the region above the Néel temperature, $T_N$=137K. To perform this experiment neutron scattering techniques were employed. The second experiment looks at another aspect of $KFeF_4$- structural phase transitions. The structural phase transitions in $KFeF_4$ occur at much higher temperatures than the magnetic phase transition. The lowest temperature structural phase transition which has been detected appears at $T_c$=400K. When studying this phase transition x-ray scattering techniques were utilised. By studying two completely different types of phase transitions- one due to magnetic interactions, the other due to structural distortions- the striking similarity of the nature of all phase transitions shall be touched upon.

In this chapter there is a brief overview of the vast field of phase transitions, with some of the theory necessary to understand phase transition experiments being outlined. In section 7.1, there is a brief introduction to the terminology of phase transitions. The simple theory of phase transitions, known as Landau theory, is described in section 7.2, before a theory which accounts for some of the short-comings of the mean-field approach is discussed in section 7.3. Finally in section 7.4, there are details of the scattering from phase transitions.

## 7.1 Introduction

The field of phase transitions encompasses many areas of solid state physics, including magnetism and crystallography. It is found that many of the phase transitions in these systems can be described by essentially the same models, which ignore the microscopic details of a system. This phenomenon is known as universality, and plays an important part in the study

of phase transitions[7.1].

Solid state systems can undergo changes from a high symmetry phase to a lower symmetry phase via two main types of transition - an order-disorder or a displacive transition. An order-disorder transition results from the ordering of atoms or molecular groups during a structural phase transition, and in a magnetic phase transition arises from the ordering of spins in a system. A displacive phase transition, as the name suggests, is a result of small displacements in the lattice positions of atoms or molecular groups. The behaviour of these transitions can be further classified by the order of the transition[7.2]. The order of a phase transition depends upon how the thermodynamic properties of the system change at the transition temperature, $T_c$. If a system undergoes a discontinuous change involving a latent heat, then this is indicative of a first-order phase transition. This means that although the free energy is the same for each of the two phases at $T_c$, the partial derivatives of the free energy are discontinuous for the first-order transition. In a second-order transition these discontinuities in the first derivatives are not seen. Historically it was thought that there would be discontinuities in the second derivatives. This was not found to be appropriate because the free energy was found to be non-analytical in this situation. The transitions are therefore more correctly known as critical phase transitions. The study of critical phase transitions began more than one hundred years ago with the discovery of critical opalescence in carbon dioxide. This opalescence is caused by droplets of fluid forming in the vapour as the critical temperature is approached. In all critical phase transitions, regions of one phase exists in the other phase as the transition is approached. This gives rise to the phenomenon known as critical scattering, which can be measured using neutron and x-ray diffraction techniques.

A whole field has grown up around the study of critical fluctuations. These fluctuations account for the failure of a mean-field approach in the study of critical phase transitions. The mean-field approach, generally known as Landau theory, is appropriate for phase transitions with long-range interactions and shall be discussed in the next section before the introduction of the theory describing critical transitions.

## 7.2 Landau Theory

The simplest approach to understanding the theory of phase transitions is by using the mean field approach employed by Landau theory[7.3]. This approach was first used in the study of continuous phase transitions, but can also be used for first-order and tricritical transitions[7.4]. In a continuous phase transition, symmetry is broken during the phase transition and this symmetry is represented by the order parameter, $\eta$. In a structural phase transition the order parameter is a measure of the relative distortion of the low symmetry structure with respect to the high symmetry phase. Generally, in structural phase transitions the low symmetry structure is the lower temperature phase. In antiferromagnetic systems the order parameter is the staggered magnetisation. In all systems the order parameter is a function of temperature and is assumed to be zero in the high symmetry phase.

Landau theory assumes that the order parameter, $\eta$, in the region of the phase transition is small, and that the free energy, $G(T,\eta)$, of the macroscopic system can be expanded in terms of the order parameter in the vicinity of the transition. At a given temperature the system will be in equilibrium when the free energy is minimised, such that

$$\begin{aligned} \frac{\delta G}{\delta \eta} &= 0, \\ \frac{\delta^2 G}{\delta \eta^2} &> 0. \end{aligned} \tag{7.1}$$

In most cases the free energy $G(\eta)=G(-\eta)$, this means that in the power series expansion of the free energy near the critical temperature only even terms are allowed. Thus in general the expansion can be written

$$G(T,\eta)=G_0+\frac{1}{2}r\eta^2+\frac{1}{4}u\eta^4+\frac{1}{6}h\eta^6+.... \tag{7.2}$$

It is often assumed that in the critical region the only coefficient in the expansion which is temperature dependent is $r$, such that

$$r=\alpha_o(T-T_o). \tag{7.3}$$

This is because when minimising the free energy it is found that $r$ must change sign at $T_o$, being positive above, and negative below $T_o$, and $\alpha_o$ is a positive constant.

Equation 7.2 is representative of a continuous phase transition if $u$ is positive, and can be used to describe a first-order transition if $u$ is negative. Using the minimisation conditions given in equation 7.1, the temperature dependence of the order parameter can be predicted. Thus for a continuous phase transition, neglecting the $\eta^6$ term, Landau theory states that the order parameter has the following temperature dependence when $T<T_o$

$$\eta=[\frac{\alpha_o}{2u}(T_o-T)]^{\frac{1}{2}}, \tag{7.4}$$

and is zero above $T_o$.

For a first-order phase transition, Landau theory predicts that the order parameter has the following temperature dependence

$$\eta^2=\frac{2}{3}\eta_1^2\{1+\left[1-\frac{3}{4}\left(\frac{T-T_0}{T_1-T_0}\right)\right]^{\frac{1}{2}}\}. \tag{7.5}$$

when $\alpha_o>0$, $u<0$, and $h>0$. This is true below $T_1$, where $T_1=T_o+(3u^2/16\alpha_0 h)$ and $\eta_1=\eta(T_1)$. $T_o$ defines the lower limit of the metastability of the high temperature phase and $T_1$ is the transition temperature. In this type of phase transition the order parameter changes discontinuously at $T_1$. Above this temperature the free energy has minima at non-zero values of the order parameter, and this can lead to hysteresis if the systems remains in one of the local minimums.

In the situation where $u=0$, the phase transition is known as tricritical. This is the point where a system crosses over from the region where a first-order transition exists to a region where the transition has critical behaviour. Tricritical transitions are relatively common in

nature, and are continuous with an order parameter that has the following temperature dependence

$$\eta = \left( \frac{\alpha_0 (T_0 - T)}{h} \right)^{\frac{1}{4}}. \qquad (7.6)$$

Notice that the exponent here is 1/4, while for a second-order transition it was 1/2.

Equations 7.4 to 7.6 describe the temperature dependence of the order parameter for a classical system. This theory breaks down when critical fluctuations play an important part in the phase transition, as is the case for systems where the interactions are short range. The following section discusses the models developed to account for deficiencies in the Landau theory.

## 7.3 Universality, Scaling and Renormalisation Group Theory

In critical phase transitions, short-lived microregions of one phase or the other are found, and as the transition is approached the size of these regions becomes infinitely large. The size of the correlated regions is denoted by $\xi$ and is known as the correlation length. The short range fluctuations of these microregions close to the critical phase transition temperature, $T_c$, give rise to short comings in the Landau theory. This theory is a mean field approximation and holds for long range interactions and cannot account for this critical behaviour.

The failure of Landau theory led to the search for new theories of phase transitions. Experimentally it was found that the correlations in systems could be described by equations with a form known as power law behaviour[7.5]. For example, the correlation length was found to have the following temperature dependence

$$\xi = \left( \frac{T - T_c}{T_c} \right)^{-\nu} = t^{-\nu}. \qquad (7.7)$$

In equation 7.7, t is known as the reduced temperature, $T_c$ is the critical phase transition

temperature and $\upsilon$ is the critical exponent of the correlation length. Other static critical properties which have this type of behaviour are the order parameter $\eta$, which has a critical exponent $\beta$, and the isothermal susceptibility which has an exponent denoted by $\gamma$. Table 7.1 gives a summary of the power-law relationships which shall be used in this work.

**Table 7.1 Power-Law Relationships**

| Property | Critical Exponent | Power Law | Condition |
|---|---|---|---|
| Susceptibility, $\chi$ | $\gamma$ | $t^{-\gamma}$ | $T>T_c$ |
| Correlation length, $\xi$ | $\upsilon$ | $t^{-\upsilon}$ | $T>T_c$ |
| Order Parameter, $\eta$ | $\beta$ | $(-t)^{-\beta}$ | $T<T_c$ |

A very interesting phenomenon appeared when analysing data using this method. Trends were noticed in the values of the critical exponents obtained, and this developed into the hypothesis of universality[7.1]. This hypothesis states that the static critical behaviour of a system depends only on the following:

1) The dimensionality of the system, d.
2) The symmetry of the order parameter, D.
3) Whether the forces are of long- or short-range order.

These conditions mean that the nature of the microscopic interactions are irrelevant, and that many different types of phase transitions have the same critical exponent behaviour. For example, this means that a solid-to-liquid transition can have the same exponents as a ferromagnetic-to-paramagnetic transition.

To calculate the magnitude of these critical exponents for different classes of system the lessons learned from universality are incorporated into a technique known as renormalisation group theory[7.6]. This takes the simplest model in a universality class, and if it can be solved, then this model can be used to describe the behaviour of all systems

in that class. In many cases the simplest models are found to be magnetic, and this is the reason for the huge interest in the area of magnetic phase transitions.

The renormalisation group approach relates the physical properties of a system close to its critical point with the properties of a similar system which is far from criticality. It does this by scaling the system, i.e. by taking the correlated domains in the critical region which have dimensions of the order $\xi$, and dividing them into cells containing L lattice sites. Each cell has a Hamiltonian that expresses its interactions with the neighbouring cell. The assumption of the theory is that the form of the Hamiltonian does not vary as the cell size is changed. By scaling the lengths in the system until a point is reached where a further transformation leaves the Hamiltonian unchanged the model has reached a fixed point. Establishing the properties of the system at this point determines the behaviour at the transition.

These techniques have been successfully applied to various simple systems. Of interest here is the two-dimensional Ising model (d=2, D=1) which has an exact solution such that $\beta$=0.125, $\nu$=1 and $\gamma$=1.75. The exponents obtained for the classical model are $\beta$=0.5, $\upsilon$=0.5, $\gamma$=1.0. Other models such as the two-dimensional Heisenberg model (d=2, D=3) cannot be solved analytically and numerical methods have been developed to solve the model. This shall be discussed further in chapter 8.

The above discussion has focused on the static behaviour of a critical phase transition. This behaviour is independent of time and gives a measure of how the length scales in the problem change as the transition temperature is approached. If a measure of the frequency of the fluctuations is required, this involves studying the dynamics of a system. It is found that as the critical point is approached, the response time of the system tends to infinity. This is known as critical slowing down. The problems of the dynamics of phase transitions are harder to solve than the static problems, and no exact solutions exist. Also, the three conditions for universality of the static properties are not enough to account for the behaviour of the dynamics of systems and further restrictions are required involving the conservation laws of a system[7.5].

## 7.4 Studying a Phase Transition

Having outlined the general features of the behaviour of a system as a phase transition is approached, it is useful to describe how scattering techniques can be used to measure the static and dynamic properties[7.7].

### 7.4.1 The Order Parameter

Measuring the temperature dependence of the order parameter is important when trying to classify whether a phase transition is continuous (second-order) or discontinuous (first-order). This is the basis of the study on the structural phase transition of $KFeF_4$ described in chapter 9.

In many structural and magnetic phase transitions new Bragg reflections appear in the low-symmetry structures due to "distortions". The loss of symmetry from one phase to the other is accounted for by the order parameter and it is found that these new reflections have an intensity which is proportional to the square of the order parameter, $\eta$. This was discussed for magnetic scattering in section 2.4 by examination of the Van Hove scattering function. It was shown there that the scattering function could be split into two parts, one being the infinitely long time component corresponding to the Bragg peaks, the other being the inelastic part. By looking at the infinitely long time part of the correlation function it can be shown that the scattering from the new Bragg reflections has the following form[7.7]

$$S(\boldsymbol{Q}) = \langle \eta \rangle^2 \delta(\boldsymbol{Q} - \boldsymbol{q}_s - \tau). \qquad (7.8)$$

Where $\mathbf{Q}$ is the scattered wavevector, $\mathbf{q}_s$ is the normal mode causing the distortion, and $\tau$ is the nearest reciprocal lattice vector. This is true for both magnetic and structural phase transitions and means that the temperature dependence of the order parameter can be determined by measuring the intensity of the new Bragg reflections allowed in the low symmetry phase.

## 7.4.2 The Critical Scattering

The inelastic part which arises from the short-time correlations between the fluctuations can be written in terms of the susceptibility of the system. The scattering function for the critical scattering is found to have the following form[7.7]

$$S_D(\mathbf{Q},\omega)=\chi(\mathbf{Q})F(\mathbf{Q},\omega). \tag{7.9}$$

In this equation $\chi(\mathbf{Q})$ represents the static susceptibility, while $F(\mathbf{Q},\omega)$ is known as the spectral weight function. The details specific to the scattering mechanisms have been omitted for simplicity. For x-ray experiments and for neutron scattering experiments which integrate over energy, the measured scattering function determines the static susceptibility, since

$$\int S_D(\mathbf{Q},\omega)d\omega=S(\mathbf{Q})=\chi(\mathbf{Q}). \tag{7.10}$$

Above $T_c$ it is found that the Ornstein-Zernike form describes the static susceptibility well[7.8]. This form is Lorentzian in shape, such that

$$\chi(\mathbf{Q})=\frac{A}{(q^2+\kappa^2)}. \tag{7.11}$$

In equation 7.11, $\kappa$ is the inverse correlation length, $1/\xi$, and $\mathbf{q}=\mathbf{Q}-\tau$ (see chapter 2). By doing an experiment where energy integration is performed, it is possible to extract values for the inverse correlation length of a system and the static susceptibility to compare with the theoretical models discussed in sections 7.2 and 7.3.

Using neutron scattering techniques, it is also possible to perform energy scans keeping the scattered vector, $\mathbf{Q}$, constant, in order that the spectral weight function, $F(\mathbf{Q},\omega)$, can be determined. It is found that the form of the spectral weight function, for small q and high temperatures, can also be represented by a Lorentzian distribution[7.7]. In this case it has the form

$$F(\mathbf{Q},\omega)=\frac{1}{\pi}\frac{\Gamma_Q}{\omega^2+\Gamma_Q^{\,2}}. \tag{7.12}$$

$\Gamma_Q$ represents the width of the spectral weight function. An experiment of this sort has been carried out on the magnetic critical scattering in $KFeF_4$, and is discussed in chapter 8.

The above discussion explains how scattering techniques can be used to measure the order parameter and critical scattering of a phase transition. The following two chapters use the theory described here to study a magnetic critical phase transition, and a structural phase transition.

## References


[7.1].R.B Griffith: Phys. Rev. Lett. 24 1479 (1970).
R.B.Griffith, J.C.Wheeler: Phys Rev A2 1047 (1970).

[7.2].H.E.Stanley: "Introduction to Phase Transitions and Critical Phenomena" (Oxford University Press, 1971).

[7.3].L.D.Landau, E.M.Lifshitz: "Statistical Physics" (London: Pergamon, 1959).

[7.4].R.A.Cowley: Advances in Physics 29 1 (1980).

[7.5].M.F.Collins: "Magnetic Critical Scattering" (Oxford University Press, 1989).

[7.6].A.D.Bruce: Advances in Physics 29 111 (1980).

[7.7].S.W.Lovesey: "Theory of Neutron Scattering From Condensed Matter" (Oxford University Press, 1984).

[7.8].R.A.Cowley, M.Hagen, D.P.Belanger: J.Phys. C:Solid State Physics 17 3763 (1984).

# Chapter 8

# Static and Dynamic Critical Behaviour of the Two-Dimensional Heisenberg Antiferromagnet $KFeF_4$

$KFeF_4$ is a well-characterised planar antiferromagnet with S=5/2. It is thought that above $T_N$ there will be a crossover from the Ising-like behaviour, found in chapter 6, to a two-dimensional Heisenberg antiferromagnet. Using neutron scattering techniques, a study of the static and dynamic critical behaviour above the Néel temperature has been undertaken to look for any changes in the critical behaviour. The results from this experiment have been compared to the theory for both a two-dimensional Ising system and the models for a Heisenberg antiferromagnet in order to study the crossover behaviour. The renewed interest in two-dimensional Heisenberg systems is discussed in section 8.1, with section 8.2 summarising the theoretical results for these models. Section 8.3 deals with the sample details and experimental set-up. A discussion of the analysis required is then given in section 8.4, before a comparison of the data with the models in section 8.5.

## 8.1 Introduction

Scaling theory states that the phase transition of a system depends upon the dimensionality of the system, d, and on the dimensionality of the order parameter, D. In $KFeF_4$, the planar magnetic layers lead to the dimensionality of the system being d=2. It is the nature of the order parameter that is in question. By studying the nature of the phase transition in the critical region above $T_N$, it is hoped that this question can be answered. This has been done by measuring the magnetic correlation functions using neutron scattering techniques and comparing the results to models for two-dimensional antiferromagnets.

The renormalisation group theory, discussed in chapter 7, has analytical solutions for some systems, but not for others. The two-dimensional Ising model (d=2,D=1) is found to be described by power-law behaviour, but for a system with isotropic interactions in two-dimensions (ie, a two-dimensional Heisenberg model:d=2, D=3) scaling theory provides no exact solutions.

With the discovery of the cuprate superconductors[8.1] has come a renewed interest in two-dimensional Heisenberg antiferromagnets[8.2]. In the undoped phase these cuprates are not superconducting but are found to order antiferromagnetically[8.3] and it is believed that the magnetism plays an important part in the processes which lead to the superconducting state[8.4]. This impetus has renewed interest in the theory of the critical behaviour of two-dimensional systems, and descriptions have now been developed for the two-dimensional quantum Heisenberg antiferromagnets (QHAF)[8.5]. This theory is a renormalisation of the classical lattice rotator model[8.6] (CLRM) and has been successfully used to describe the S=1/2 $La_2CuO_4$[8.5] and the S=1 system $K_2NiF_4$[8.7].

Many experiments were performed on the two-dimensional antiferromagnets with the $K_2NiF_4$ structure in the 1970's[8.8], [8.9]. In these systems the low temperature behaviour is dominated by small Ising-like anisotropy terms, leading to two-dimensional Ising critical behaviour below $T_N$. For $K_2NiF_4$ it is found that the Ising behaviour persists above $T_N$ until a crossover to a Heisenberg region is reached. Birgeneau[8.8] has fitted the static correlation length of $K_2NiF_4$ to the two-dimensional Ising model between $T_N$ and $1.05T_N$, and above this has shown[8.7] that the system is in excellent agreement with the two-dimensional isotropic QHAF theory developed by Chakravarty, Halperin, and Nelson (CHN)[8.5]. Like the $K_2NiF_4$ materials, $KFeF_4$ has magnetic planes separated from each other by sheets of non-magnetic ions leading to weak interplanar interactions. In $KFeF_4$ this leads to a ratio of the order $10^{-4}$ between interplanar and intraplanar interactions, giving rise to the two-dimensional nature of the system. It also has a weak Ising like anisotropy term which aligns the spins along the crystallographic *c*-axis

$KFeF_4$[8.10] is a S=5/2 system and thus is likely to behave more classically than the systems already studied. Table 8.1 gives a comparison of some of the physical parameters

of the systems already studied by the QHAF model with $KFeF_4$. In this table, the average nearest-neighbour spacing between spins is represented by $a_{NN}$. $J_{NN}$ is the nearest-neighbour exchange constant between spins, and $h_A$ is the ratio between the anisotropy energy and the nearest-neighbour exchange constants[8.8]. Notice this has similar magnitudes for all three systems, and is the important factor in determining whether the systems behaviour is Ising or Heisenberg-like.

**Table 8.1 Comparing the properties of some two-dimensional antiferromagnets.**

| | $a_{NN}$/Å$^{-1}$ | $J_{NN}$/K | S | $T_N$/K | $h_A$ |
|---|---|---|---|---|---|
| $La_2CuO_4$ | 3.8 | 600 | 1/2 | 195 | 0.006 |
| $K_2NiF_4$ | 2.82 | 52 | 1 | 97.2 | 0.0021 |
| $KFeF_4$ | 3.86 | 14.25 | 5/2 | 136.75 | 0.005 |

Having characterised the strength and nature of the interactions in $KFeF_4$ by measuring the dispersion relation (chapter 6), it was found that the Heisenberg exchange interactions were by far the largest ones. Experiments have been performed to study how these interactions affect the nature of the magnetic phase transition. Firstly, in $KFeF_4$ the small Ising term is found to dominate the critical behaviour below $T_N$. Previous work, as discussed in chapter 6, has shown that the staggered magnetisation has power-law temperature dependence with $\beta$=0.13, close to that predicted by theory for a two-dimensional Ising system ($\beta$=0.125)[8.11]. This was measured by studying the temperature dependence of the integrated intensity of a magnetic Bragg peak, and is in agreement with studies performed on $KFeF_4$ using Mossbauer techniques[8.12].

In this chapter, neutron scattering studies are described which look at whether this Ising term will affect the critical region above $T_N$. Both the static and dynamic magnetic critical behaviour have been studied. Measuring the magnetic static susceptibility gives a measure of the correlation lengths between spins in the system, and shows how these decay with temperature. The dynamic susceptibility is a measure of the temporal correlations in the system. By measuring these quantities and comparing them to various theoretical models for

two-dimensional systems, it should be possible to determine how the phase transition behaviour depends on the competing Heisenberg and Ising exchange interactions.

## 8.2 Theory

Two-dimensional Heisenberg antiferromagnets have no long-range order above T=0K[8.13]. This result was proved by Hohenberg, Mermin and Wagner for one- and two-dimensiónal systems, and shows that no spontaneous magnetisation can occur for these Heisenberg systems with finite range interactions at non-zero temperatures. It is the weak anisotropies in real systems which lead to long-range order at finite temperatures. In the theories described below it is assumed that the ground-state with conventional antiferromagnetic order is at T=0K and the correlation functions for the long-range order decay are described from this point rather than from a finite Néel temperature as in real systems.

The CLRM[8.6] is a model describing the behaviour of a classical two-dimensional Heisenberg antiferromagnet. When calculating the correlations between spins it assumes that short-wavelength fluctuations can be neglected, and that the T=0K state has long-range order with a fully aligned Néel state. It then uses the renormalisation group method to calculate the Hamiltonian of the system. The calculations involved in this task cannot be done analytically, and numerical techniques using Monte Carlo methods are used to calculate the thermodynamic quantities. Using these methods the CLRM predicts that the correlation length in a classical Heisenberg antiferromagnet is given by[1]

$$\frac{\xi}{a_{NN}} = B_{\xi} \frac{\exp(4\pi\rho_s / k_b T)}{4\pi\rho_s / k_b T + 1}, \qquad \textbf{(8.1)}$$

where $B_{\xi}$=0.01, $a_{NN}$ is the nearest neighbour separation and $\rho_s$ is the classical value of the spin-wave stiffness constant without the spin fluctuation terms (see equation 8.3).

---

[1] This equation has $4\pi\rho_s$ and not $2\pi\rho_s$ as written in reference [8.5] due to the different definition of the exchange constants in this work.

CHN have taken the classical model for a two-dimensional Heisenberg antiferromagnet and have renormalised the results to take into account quantum fluctuations. They also introduce the thermal de Broglie wavelength, $\hbar c/k_b T$, as a short-wavelength cut-off instead of a constant times the lattice spacing $a_{NN}$, which is used as a length scale in the classical problem. Using this method they have produced a model for the quantum Heisenberg antiferromagnet (QHAF) to describe the instantaneous correlations and it is found that their model is in reasonable agreement with the available experimental data[8.5], [8.7]. The CHN theory predicts that the correlation length is given by

$$\frac{\xi}{a_{NN}} = C_\xi \frac{\exp(4\pi\rho_s/k_b T)}{1+k_b T/4\pi\rho_s}. \qquad \textbf{(8.2)}$$

The difference in the denominators in equations 8.1 and 8.2 arises from the use of the thermal cut-off in the QHAF, instead of a constant times the lattice spacing as used in the CLRM. In equation 8.2, $\rho_s$ is the spin-wave stiffness constant defined such that

$$4\pi\rho_s = 4\pi J_{NN} S^2 Z_c(S)^2 Z_x(S), \qquad \textbf{(8.3)}$$

$$Z_c = 1 + 0.158/2S + O(1/2S)^2, \qquad \textbf{(8.4)}$$

$$Z_x = 1 - 0.552/2S + O(1/2S)^2, \qquad \textbf{(8.5)}$$

with $J_{NN}$ being the nearest-neighbour exchange constant and $S$ the spin of a magnetic ion. The $Z_c$ and $Z_x$ terms are correction factors to take into account quantum fluctuations. In a spin 5/2 system these terms are small and only change the spin-wave stiffness constant by 5% of its classical value. The quantum fluctuation terms become more important the lower the spin. In the case of S=1/2, the spin-wave stiffness constant is altered by 40% by the Oguchi fluctuation terms[8.14]. For $KFeF_4$, S=5/2 and $J_{NN}$=1.223meV. The nearest-neighbour exchange has been taken as the average from the fits to dispersion relation in chapter 6. CHN theory predicts that the constant $C_\xi$ in equation 8.2, has the following form

$$C_\xi = \frac{\sqrt{32}\, e^{\frac{\pi}{2}} B_\xi}{C_{\rho_s}}, \tag{8.6}$$

with

$$C_{\rho_s} = \frac{2\pi S Z_x Z_c}{\sqrt{8}}, \tag{8.7}$$

which for S=5/2 gives $C_\xi \approx 0.06$ to within 30%, this is almost twice as large as the value predicted by Manousakis and Salvador[8.15] using Monte Carlo simulations. The uncertainty in the CHN theory arises from the uncertainty in $B_\xi$, the value calculated for the classical model scaling factor. Hasenfratz et al[8.16] have predicted the exact prefactor as

$$C_\xi = \frac{e}{8 C_{\rho_s}}. \tag{8.8}$$

This gives $C_\xi \approx 0.07$ for S=5/2. It is clear from this discussion of the scaling constant $C_\xi$, that it is not a well defined parameter.

The structure factor for both the CLRM and the QHAF models depends upon the correlation length in the following way

$$S(0) = \frac{C_s \xi^2}{[(4\pi \rho_s / k_b T) + 1]^2}, \tag{8.9}$$

where

$$S(0) = \int S(q_{x,y}=0, \omega) d\omega. \tag{8.10}$$

The equation for $\xi$ being either equation 8.1 for the CLRM, or equation 8.2 for the QHAF. Equations 8.1-8.9 define the temperature dependence of the static critical behaviour for both

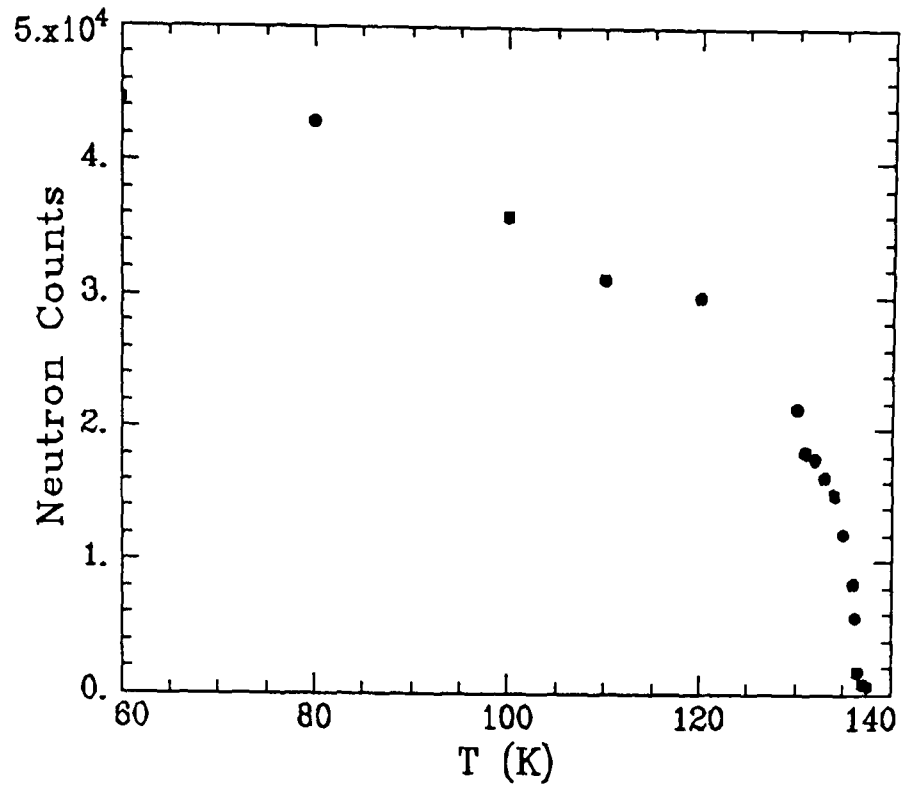


Figure 8.1a: Temperature dependence of the (1,1,0) magnetic Bragg reflection.

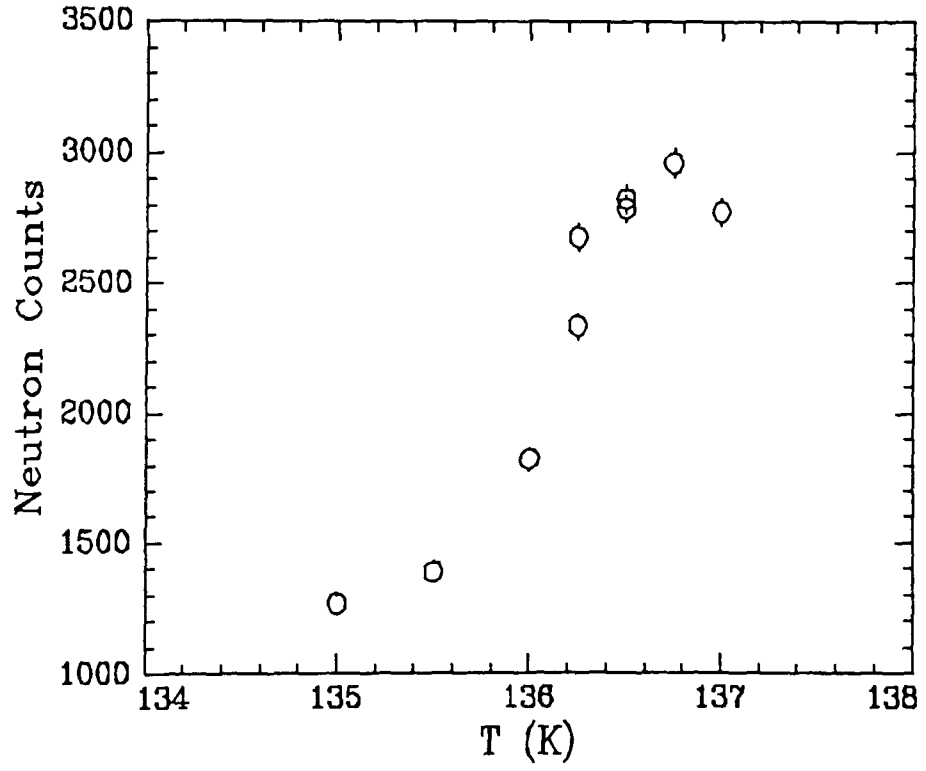


Figure 8.1b: Temperature dependence of the two-dimensional susceptibility.

the CLRM and the QHAF.

The dynamics of the two-dimensional Heisenberg system have been studied by Tyc et al[8.17]. The energy width of the order-parameter correlation function $S(Q,\omega)$ at $q_{x,y}=0$, has a FWHM given by

$$\Gamma=\gamma\varpi_o=\gamma c\xi^{-1}(T/4\pi\rho_S)^{\frac{1}{2}}, \tag{8.11}$$

where $c$ is the spin-wave velocity in meVÅ, when the width is in meV and $\gamma\approx0.85\pm0.15$ is a constant[8.18]. For $KFeF_4$, $c$ has been determined from the dispersion relation as 70mevÅ.

The data was also fitted to the power-law behaviour (as discussed in chapter 7), which characterises the temperature dependence of the two-dimensional Ising model[8.19], [8.20]. For example the correlation length is given by

$$\frac{\xi}{a_{NN}}=\frac{1}{\kappa a_{NN}}=K_o t^{-\upsilon}. \tag{8.12}$$

Here $\kappa$ is known as the inverse correlation length. For a two-dimensional Ising system $\upsilon=1$ and $K_o$ is a scaling constant which for a two-dimensional square lattice has the value 1.763[8.19] Comparing the data to all the models will help in understanding the nature of the magnetic phase transition.

## 8.3 Sample and Experimental Preliminaries

The $KFeF_4$ single crystal was prepared at the Univeristé du Maine using the Bridgeman Stockbarger technique in a platinum crucible. The crystal was a small plate of dimensions 4mmx3mmx15mm. At room temperature $KFeF_4$ has an orthorhombic structure, with $a$=7.63Å, $b$=7.80Å, $c$=12.33Å (for more details see chapter 9). This crystal has been used in a previous neutron scattering study[8.10], and it was found that in the (h,h,l) plane the mosaicity was 0.09°. From the low temperature studies (on a different sample) it is found that $J_{NN}$=1.223meV

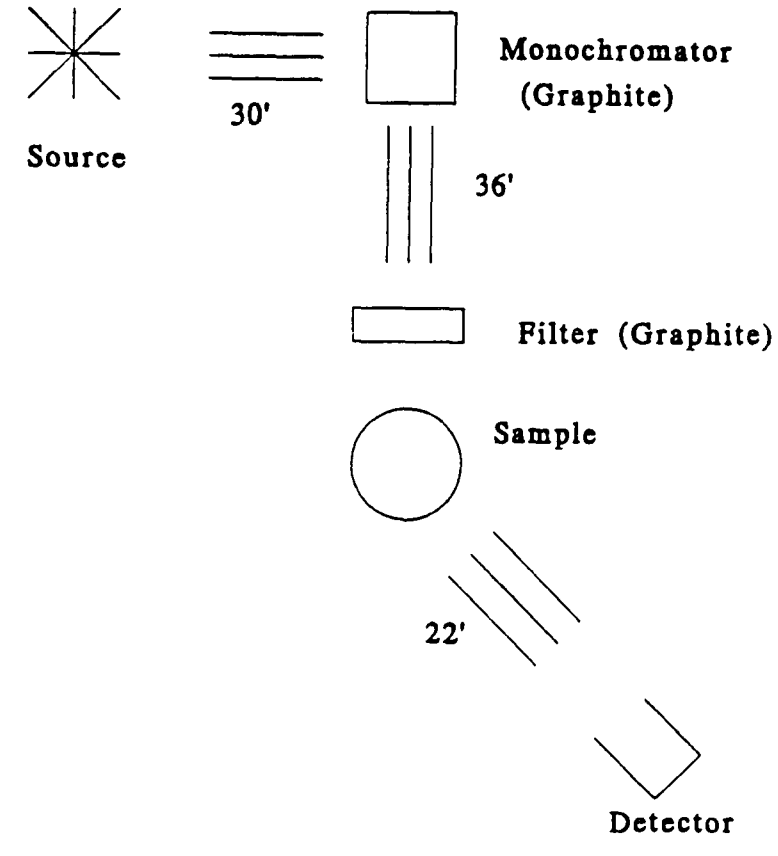


Figure 8.2a: TAS6 set-up for static critical scattering.




Figure 8.2b: TAS6 set-up for dynamic critical scattering.

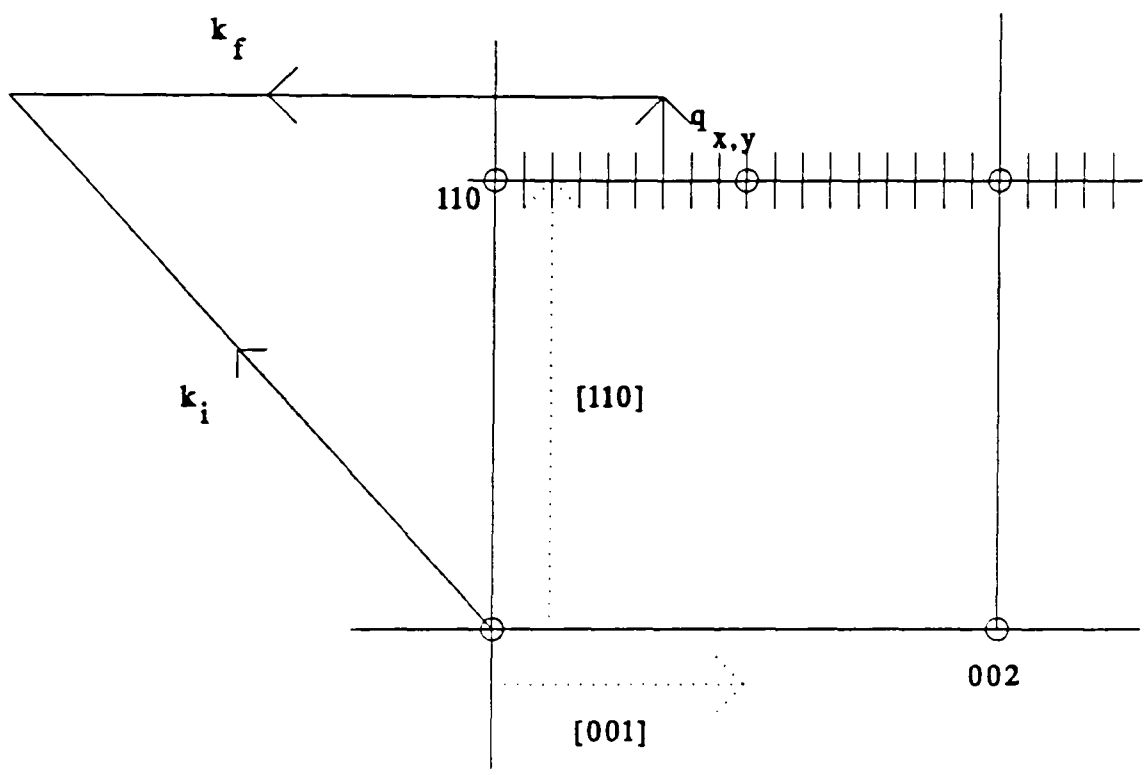


Figure 8.3: The scattering set-up to collect the static critical scattering. This arrangement minimises errors from the experimental energy integration.

(see chapter 6). This is estimated by taking an average of the exchange interactions in the **a** and **b** directions.

The crystal was mounted with the (h,h,l)-plane in the scattering plane and was placed in a variable temperature, closed cycle cryostat in order that a temperature controlled experiment could be performed, with a stable temperature of ±0.01K. The transition temperature, $T_N$, of $KFeF_4$ was determined by measuring the temperature dependence of the (1,1,0) magnetic Bragg peak, which measures the extent of the three-dimensional ordering, and by the temperature dependence of the scattering from a wavevector transfer of (1,1,0.53), which is determined by the two-dimensional susceptibility. The susceptibility is expected to diverge at $T_N$, while the order parameter goes to zero. The results are shown in figure 8.1 and give a transition temperature $T_N$=136.75±0.25K, in good agreement with previous studies on $KFeF_4$[8.21], [8.12].

To collect the static critical scattering data, the TAS6 instrument at the Risø facility was used in the two-axis mode- the energy analyser having been removed in order that the energy integrated intensity could be measured (see figure 8.2a). The critical scattering was measured by scanning along the line (ζ,ζ,0.53) in reciprocal space. This point was chosen so that the scattered wavevector was parallel to the *c*-axis where the scattering is only slowly varying. Any inelasticity changing the magnitude of $k_f$ will not affect the magnitude of the in-plane wavevector, $q_{x,y}$, and thus the energy integration is expected to be good (see figure 8.3)[8.22]. A pyrolytic graphite monochromator was used to produce a monochromatic beam of neutrons with a wavevector $k_i$=2.51Å$^{-1}$, and a pyrolytic graphite filter was placed between the monochromator and sample to suppress higher order neutrons. The collimation used was 30′ before the monochromator, 36′ between the monochromator and sample and 22′ between the sample and detector. The resolution function was measured at 9K using the (1,1,0) Bragg reflection and was found to have a width (FWHM) along (ζ,ζ,0) of 0.027Å$^{-1}$ and vertically of 0.113Å$^{-1}$. Note that in a similar experiment performed on $K_2NiF_4$[8.8], the resolution along the scan direction was only 0.016Å$^{-1}$.

The dynamic scattering was measured using TAS6 in the three-axis mode by placing a pyrolytic graphite analyser between the sample and detector. This mode of the instrument

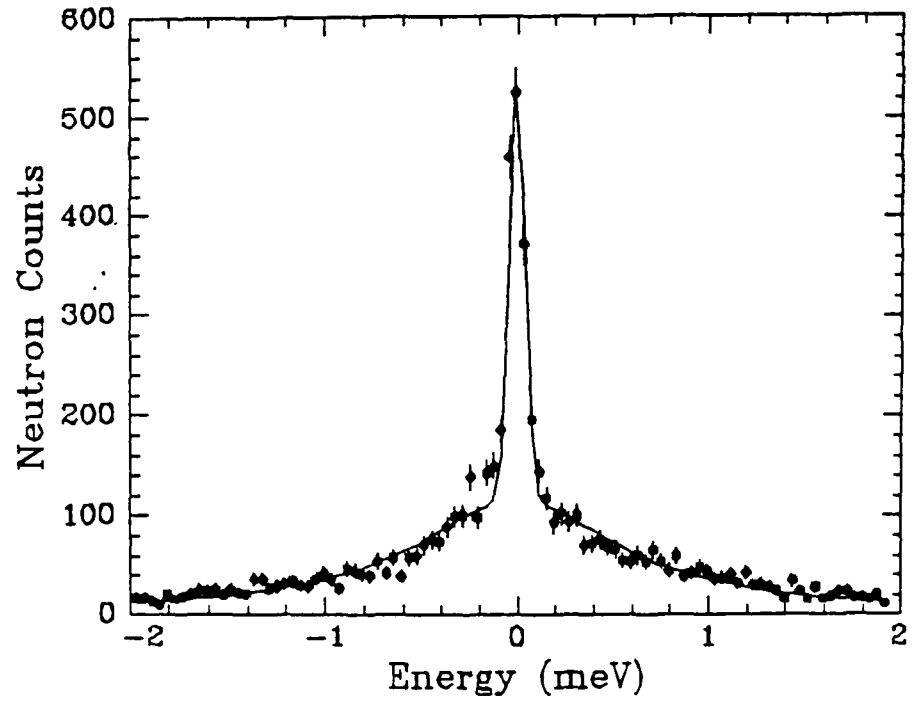


Figure 8.4: The dynamic scattering measured at the I.L.L. at 155K. Notice the sharp structural feature on top of the broad dynamic scattering.

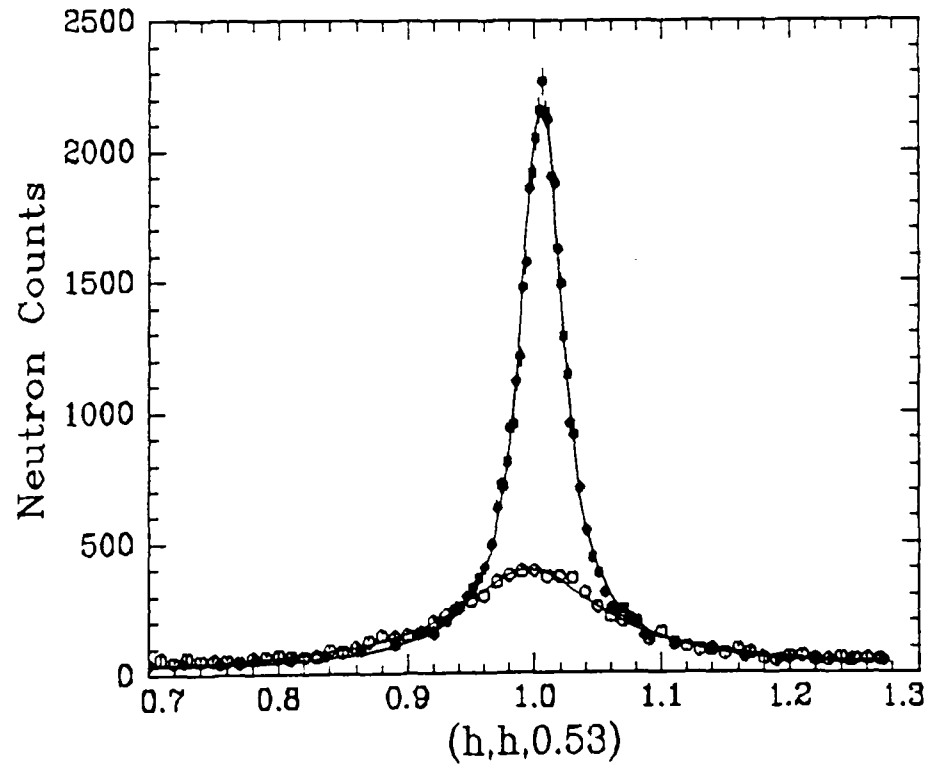


Figure 8.5: The static critical scattering from $KFeF_4$ at T=147K (filled circles) and T=180K (unfilled circles).

is shown in figure 8.2b. The energy resolution was measured using the isotropic incoherent scatterer vanadium, and was found to be 1.012meV (FWHM). The scans to measure the order-parameter correlation function as a function of energy were taken keeping Q fixed at (1,1,0.53). This was point was chosen as it was far away from the Bragg peaks and thus structural effects can be neglected when analyzing the data.

A preliminary study of the dynamic scattering has already been carried out at the I.L.L. on the IN3 instrument. The set-up was similar to that described in chapter 6. There the crystal was lined up with the ab-plane as the scattering plane, and the energy scans were done keeping q fixed at (1,1,0). This caused problems as there was a weak structural peak present which made it difficult to analyze data above 170K (see figure 8.4). A comparison of the results extracted from both sets of data will be made in sections 8.4 and 8.5.

## 8.4 Experimental Results and Analysis

The details of the data analysis for the static and dynamic scattering are given in sections 8.4.1 and 8.4.2 respectively. The tabulated results of the fits to the theories for two-dimensional Heisenberg models are given in section 8.5.

### 8.4.1 The Staggered Static Susceptibility

The static critical scattering was measured at 27 temperatures between $T_N$ and 240K. As was expected, qualitatively the results show that as the temperature is increased the intensity decreases and the width increases, this is shown in figure 8.5. For a Heisenberg system one would expect the susceptibility to be isotropic, i.e. the susceptibility parallel and perpendicular to the spin direction to be the same. For an Ising system the parallel and perpendicular susceptibilities are highly anisotropic, with only the susceptibility parallel to the spin direction being critical at $T_N$. When modelling the susceptibility, the differences between the Heisenberg and the Ising-like systems have been taken into account.

In order to compare the data with the Heisenberg models, a single Lorentzian profile was fitted with the following form

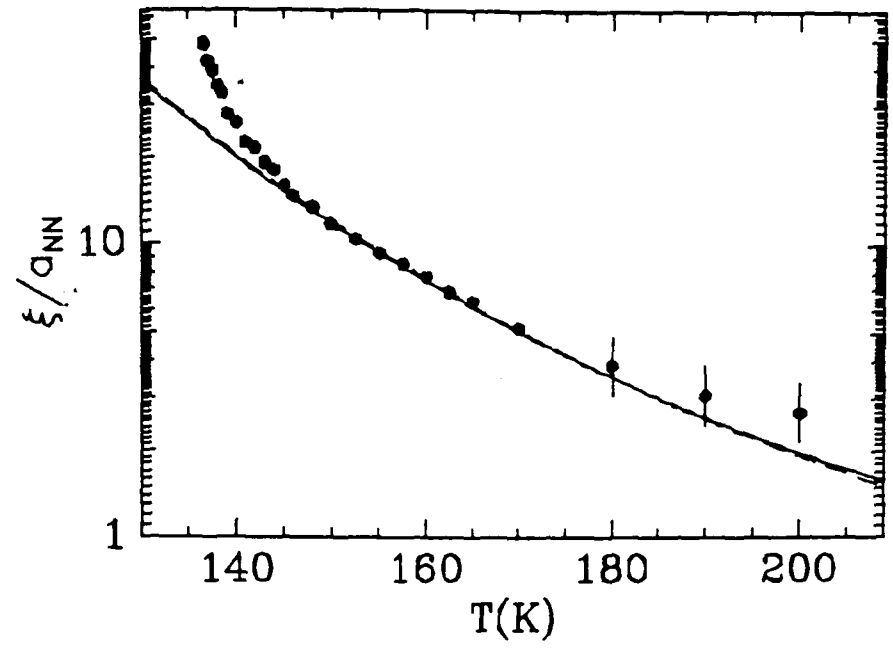


**Figure 8.6: Temperature dependence of the static correlation length compared with the CLRM (solid line) and the QHAF (dashed line).**

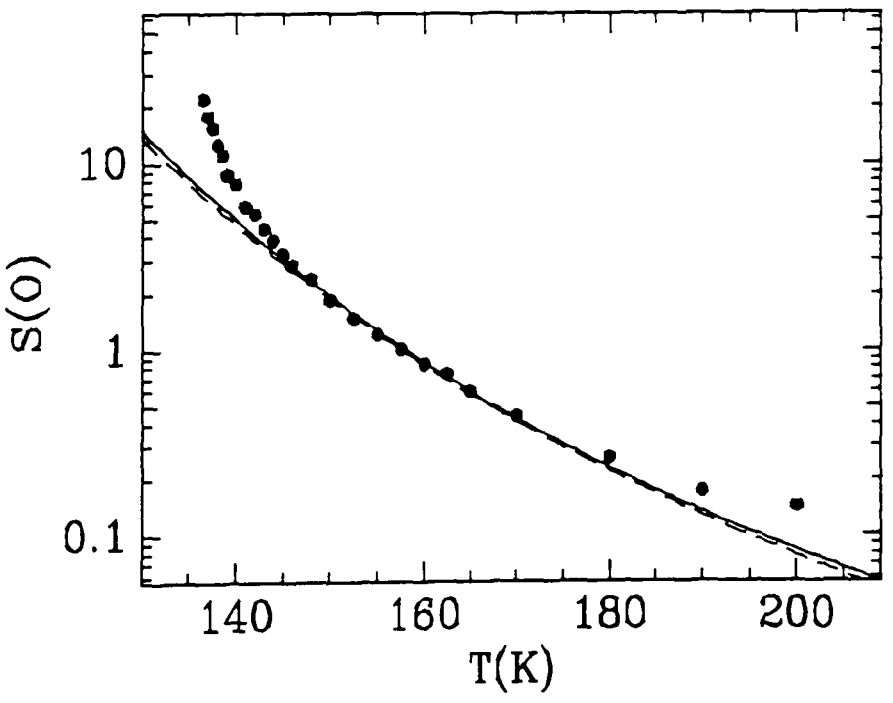


**Figure 8.7: The temperature dependence of the structure factor in $KFeF_4$. The solid line represents the CLRM, the dashed line is a fit to the QHAF model.**

$$S(q)=\frac{A}{q_x^{\,2}+q_y^{\,2}+\xi^{-2}}, \qquad \textbf{(8.13)}$$

This was convolved with a triangular vertical resolution function, and with a Gaussian form along the $(\zeta,\zeta,0)$ direction[8.22]. In addition the background was held fixed at 18 counts for a monitor of 50000 (this corresponds to approximately 25 seconds). The results from these fits have been compared to the theories for the two-dimensional Heisenberg models (equations 8.1 and 8.2, for the correlation lengths, and equation 8.9 for the structure factor) and are shown in figures 8.6 and 8.7. The data appear to fit well to both the theories in the region $1.04T_N<T<1.4T_N$. In the fits the spin-wave stiffness was held constant and only the scaling prefactor was allowed to vary. A comparison of the prefactors obtained from the fits with the theoretical predictions are shown in section 8.5 in tables 8.2 and 8.3 and shall be discussed in more detail in that section. From the fits to the correlation length, $\xi$, the tables show that both the CLRM and the QHAF give similar goodness of fits, $\chi^2$, and thus both models seem to fit the data equally well, in the same temperature region. This was also found to be true for the structure factor fits, although the prefactors from these fits cannot be directly compared with the theory.

To analyze the data in terms of the Ising model, the separate contributions from the parallel and perpendicular susceptibilities were taken into account[8.8] and a two-Lorentzian model was used. The data near $T_N$ was thus fitted to

$$S(q)=\frac{A_{\parallel}}{q_x^{\,2}+q_y^{\,2}+\xi_{\parallel}^{-2}}+\frac{A_{\perp}}{q_x^{\,2}+q_y^{\,2}+\xi_{\perp}^{-2}}, \qquad \textbf{(8.14)}$$

with the perpendicular susceptibility modelled such that $A_\perp$ was held at its $T_N$ value and with $\xi_\perp$ assumed to follow the same power law as $\xi_\parallel$, but with a shifted $T_N$, see figure 8.8. To fix the width of the perpendicular component of the susceptibility, fits to the data in the region $T\leq 0.95T_N$ were done, assuming that at these temperatures only the perpendicular component is significant. It was found, as expected that the widths of the peaks at these temperatures is constant. A typical scan is shown in figure 8.9, along with a fit to a single Lorentzian. Using this to fix the width of the perpendicular component at $T_N$, and allowing it to have the same

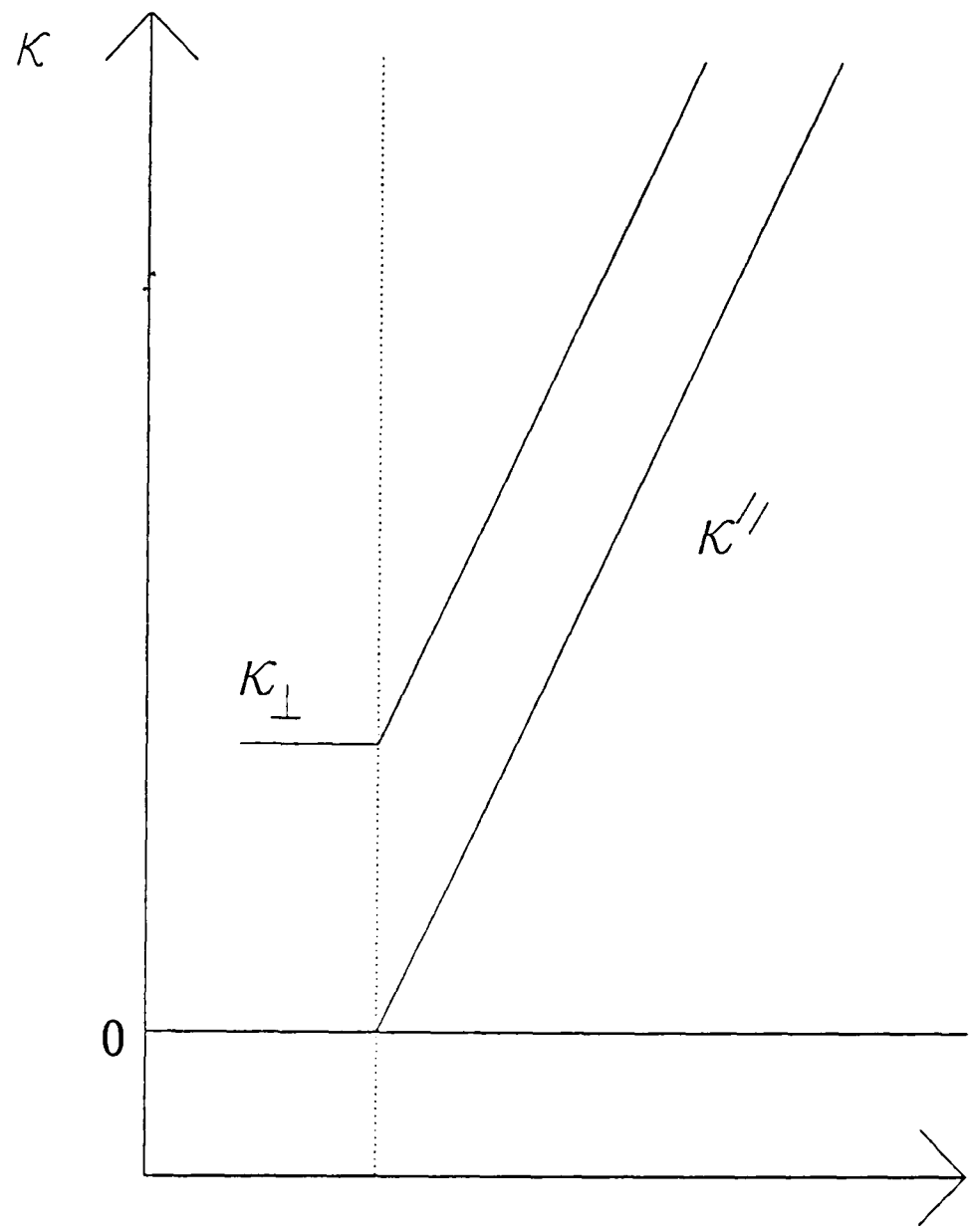


Figure 8.8: The temperature variation of the perpendicular and parallel inverse correlation lengths of an Ising antiferromagnet.

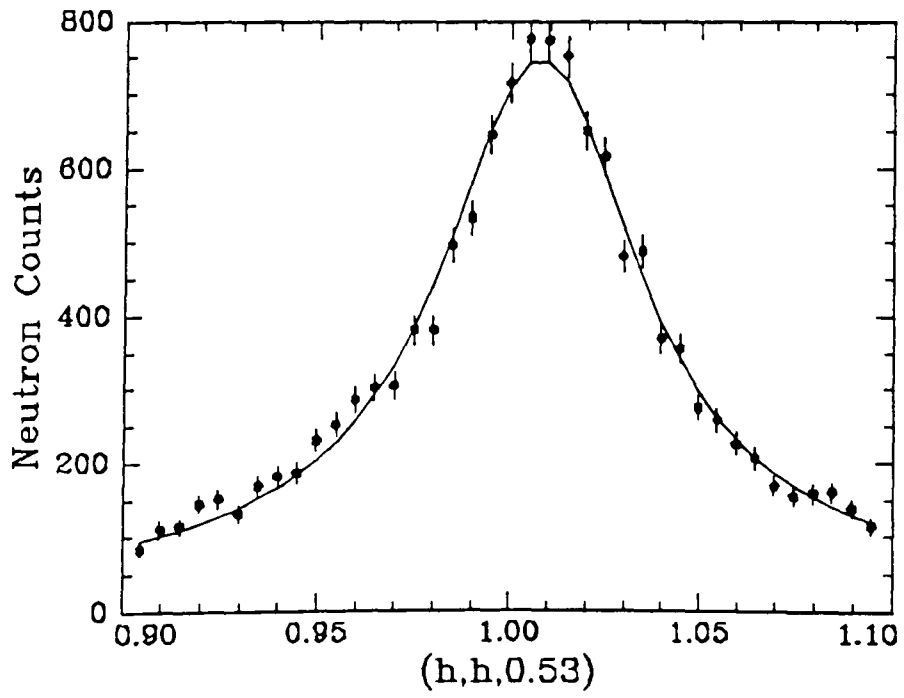


Figure 8.9: Measuring the perpendicular susceptibility of $KFeF_4$ at 128K.

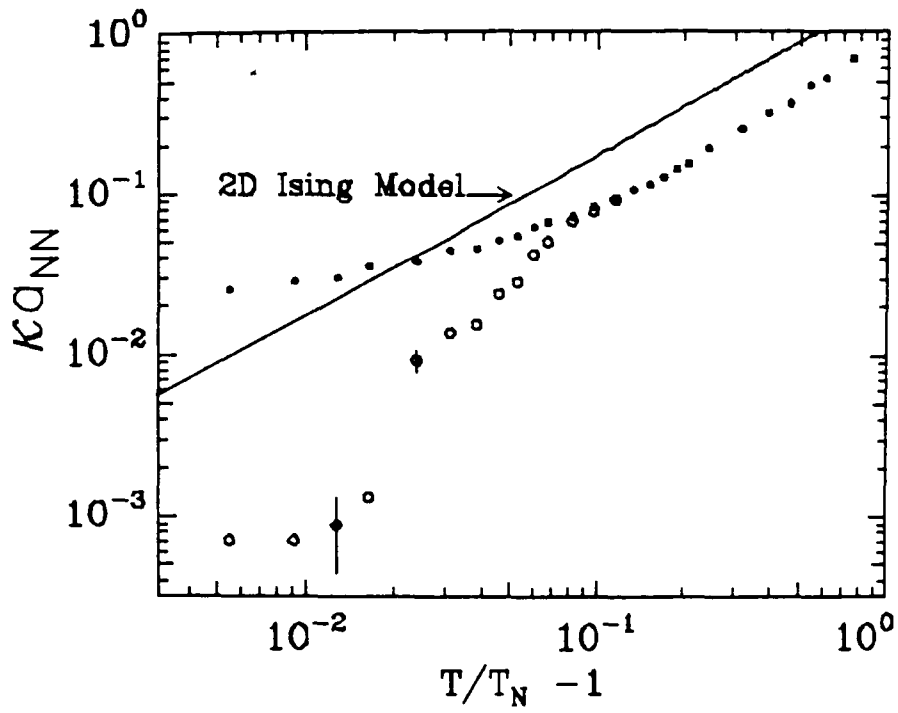


**Figure 8.10: The inverse correlation lengths extracted from the fits to equation (8.13) (filled circles), and to equation (8.14) (unfilled). The line is a simulation of the 2D Ising model.**

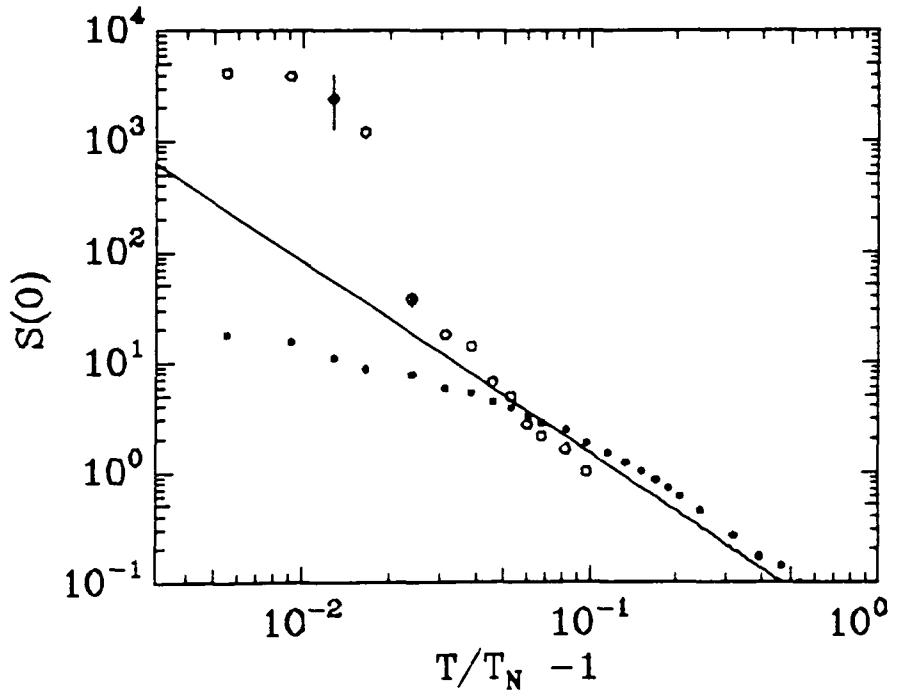


**Figure 8.11: The structure factor extracted from fits to equation (8.13) (filled circles), and to equation (8.14) (unfilled). The line is a simulation of the 2D Ising model.**

temperature dependence as the parallel component, gives the results shown in figure 8.10. This also shows a comparison with the theory for the two-dimensional Ising model. Fits keeping $\xi_\perp$ at the transition value were also done and within the experimental accuracies this did not change the widths extracted for the parallel susceptibility, in agreement with fits done on $K_2NiF_4$[8.8].

In figure 8.10, the two sets of data points represent the fits from the both the single (equation 8.13) and two-Lorentzian models (equation 8.14). These have been displayed as the inverse correlation length, $\kappa a_{NN}$, as defined in equation 8.11. The graph shows that the analysis for the two component Lorentzian model fails close to $T_N$ due to the narrow width in reciprocal space of the susceptibility peak. The resolution function and the fixed component of the perpendicular width make accurate measurement of the parallel contribution very difficult. Fitting the structure factor obtained from the fits to the Lorentzians gives similar results (see figure 8.11). The straight line represents a simulation of the two-dimensional Ising model which is expected to model the data asymptotically close to $T_N$. As is seen this is clearly not the case for this data. This is in contradiction with the results for $K_2NiF_4$. It is thought that this failure to fit the data to the Ising model close to $T_N$ is due to poor resolution, rather than suggesting $KFeF_4$ is not Ising-like in this region. Remember that below the transition, an Ising critical exponent was obtained for the temperature dependence of the order parameter.

## 8.4.2 The Dynamic Susceptibility

The dynamic critical scattering was collected at twelve temperatures above $T_N$ and was fitted to a single Lorentzian

$$S(\omega)=\frac{A}{\omega^2+\Gamma^2} \qquad \textbf{(8.15)}$$

convolved with the energy resolution, see figure 8.12. In equation 8.15, $S(\omega)$ represents $S(\mathbf{Q},\omega)$ at fixed $\mathbf{Q}$. The results of these fits are shown in figure 8.13 along with the theory for the two-dimensional Heisenberg systems. The TAS6 points at 170K and above are clearly inconsistent with the other data points and the theory. This is possibly due to a breakdown

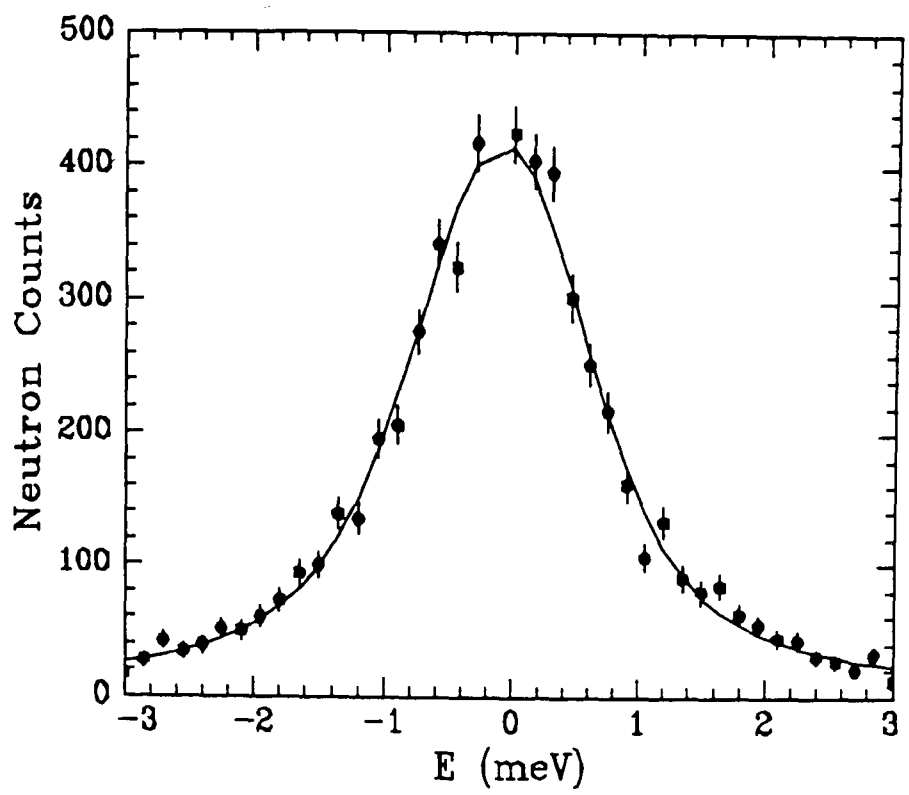


**Figure 8.12: Measuring the dynamic susceptibility of $KFeF_4$ at 147K.**

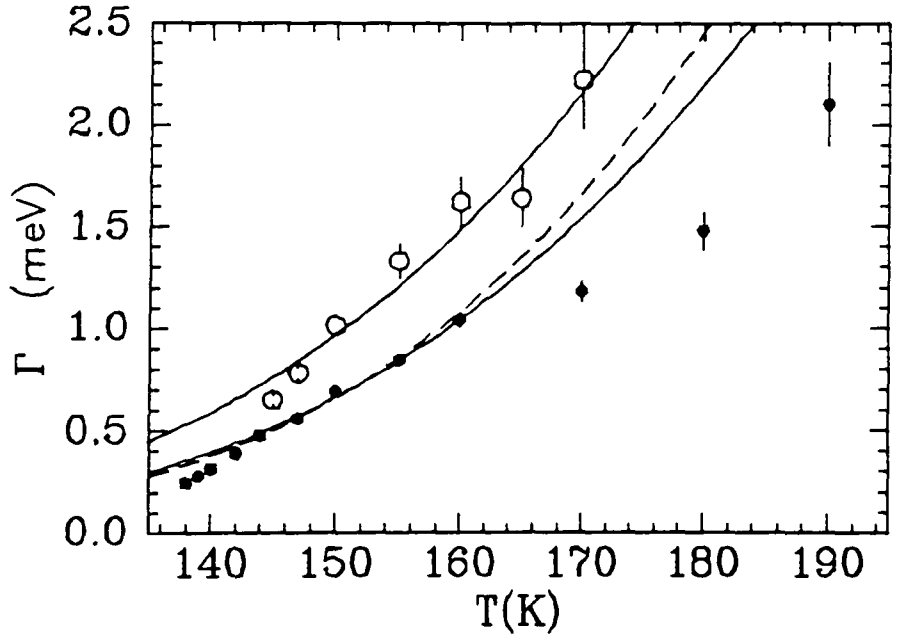


**Figure 8.13: Comparing widths extracted from the I.L.L data (unfilled) with TAS6 data (filled). The CLRM is the solid line, the QHAF model the dashed line.**

in the data analysis as the magnetic contribution becomes small. Divergence from the theory was also seen in the fits to the correlation length and the structure factor data, although in those cases it was seen at higher temperatures (190K). The two-dimensional Heisenberg theory for the dynamic scattering has been fitted between 144K and 160K by adjusting the scaling prefactor to fit the data. Similar data were collected at the I.L.L. and these results are also shown in figure 8.13. The fits in figure 8.13 show that the TAS6 data widths are narrower than the I.L.L. data. This is because resolution effects were not taken into account for the I.L.L: data. There were also complications due to the extra component arising from the structural effect (see figure 8.4). To extract $C_\xi$, and $B_\xi$, from the prefactor obtained from the fits to the dynamic scattering function, the following equation was used, this comes directly from equations 8.9, 8.1 and 8.2

$$prefactor = \frac{\gamma c}{C_\xi a_{NN}}, \tag{8.16}$$

and similarly for $B_\xi$. In Equation 8.16, $\gamma$=0.85 and is a constant, $c$ is the spin-wave velocity which is system dependent and for $KFeF_4$ $c$=70meVÅ. The results extracted for $C_\xi$ and $B_\xi$, as a result of the fits to the widths of the dynamic susceptibility, are shown in table 8.2, for the QHAF and table 8.3 for the CLRM.

In the next section the constants extracted from the fits of the correlation length and the width of the dynamical scattering are compared to both the CLRM and the QHAF theoretical predictions.

## 8.5 Comparison of Experiments With Theory

The results of the fits to the QHAF and the CLRM shown in tables 8.2 and 8.3 for $KFeF_4$. Both theories give scaling constants which are approximately four times different from the predictions. For the QHAF the average value of $C_\xi$ from all the fits is 0.009±0.001. This is of the order 3-6 times smaller than the theoretical predictions. It was possible to fit the data for $KFeF_4$ to the QHAF model in the region $1.04<T/T_N<1.4$, this is in agreement with the $K_2NiF_4$ data.

**Table 8.2 Comparing the results from the fits to the data with the QHAF models.**

| QHAF | $C_\xi$ | $4\pi\rho/K$ | $\chi^2$ |
|---|---|---|---|
| $\xi$ | 0.010±0.001 | 1080 | 4 |
| TAS6 : $\Gamma$ | 0.0079±0.0001 | 1080 | 1.05 |
| I.L.L. : $\Gamma$ | 0.0080 ± 0.0002 | 1030 | 5.5 |
| CHN | 0.06 | - | - |
| MC | 0.03 | - | - |

The fits to the CLRM are given in table 8.3 and give an average value of $B_\xi$=0.040±0.003. This is four times larger than $B_\xi$ calculated from the CLRM. It was also only possible to fit the data in the temperature region $1.04T_N<T<1.4T_N$. Both sets of fits (ie to the CLRM and the QHAF), allowed fits using values of the spin-wave stiffness constant predicted from the dispersion relation. Thus it is concluded that in the region $1.04T<T_N<1.4T$, $KFeF_4$ is equally well described by the QHAF model and the CLRM.

**Table 8.3 Comparing the data with the CLRM.**

| CLRM | $B_\xi$ | $2\pi\rho/K$ | $\chi^2$ |
|---|---|---|---|
| $\xi$ | 0.052±0.001 | 1140 | 6 |
| $\xi$ | 0.033±0.003 | 1220±15 | 4 |
| TAS6 : $\Gamma$ | 0.039±0.001 | 1140 | 0.8 |
| I.L.L. : $\Gamma$ | 0.036±0.001 | 1090 | 6.5 |
| THEORY | 0.01 | - | - |

The previous study on $KFeF_4$ in chapter 6 showed that below $T_N$ it exhibited two-dimensional Ising-like behaviour. Since with the TAS6 data it has not been possible to fit to a power law behaviour in the critical region above the transition temperature, it cannot be said exactly where the crossover from Ising-like to Heisenberg-like behaviour occurs. It is

stated[8.7] that the crossover should occur when $h_A(\xi/a_{NN})^2 \sim 1$; for $KFeF_4$, $h_A = 0.005$ and this implies $\xi/a_{NN} \sim 14$. From figure 8.6 it may be seen that $\xi/a_{NN}=14$ when T=143K, and indeed the theory for the two-dimensional Heisenberg system has departed from the data below this temperature.

When Birgeneau fitted the $K_2NiF_4$ data[8.7] to the QHAF he obtained excellent agreement with the theory in the region $1.05T_N<T<1.5T_N$. The scaling prefactor obtained for the correlation length which was less than 30% from the CHN theoretical prediction of $C_\xi$ for a S=1 system. Similar analyses on $La_2CuO_4$ did not give such good agreement with the theory, $C_\xi$ being twice that for a S=1/2 CHN antiferromagnet. The results of fitting the Heisenberg model to the $KFeF_4$ data are not in as good agreement with the theoretical predictions as these experiments. Given the uncertainties in the theory it is thought that these results are of the correct order of magnitude and show that qualitatively $KFeF_4$ agrees with a two-dimensional Heisenberg analysis in the same temperature range as previous studies.

## 8.6.Conclusions

It has not been possible to fit the static correlation length of $KFeF_4$ to the theory for a two-dimensional Ising model asymptotically close to $T_N$ as was done for $K_2NiF_4$ and as would be expected from the theory. Above $1.04T_N$, $KFeF_4$ seems to be in qualitative agreement with the quantum and classical theories for a two-dimensional Heisenberg system, although the prefactors are not as close to the quantum theoretical predictions as the other systems were. These other systems were not compare to the CLRM. The analysis for $KFeF_4$ seems to break down above $1.4T_N$. To study the crossover from two-dimensional Ising to two-dimensional Heisenberg behaviour it would be necessary to carry out an experiment with better resolution and temperature control close to $T_N$. A summary of these results is shown in figure 8.14.

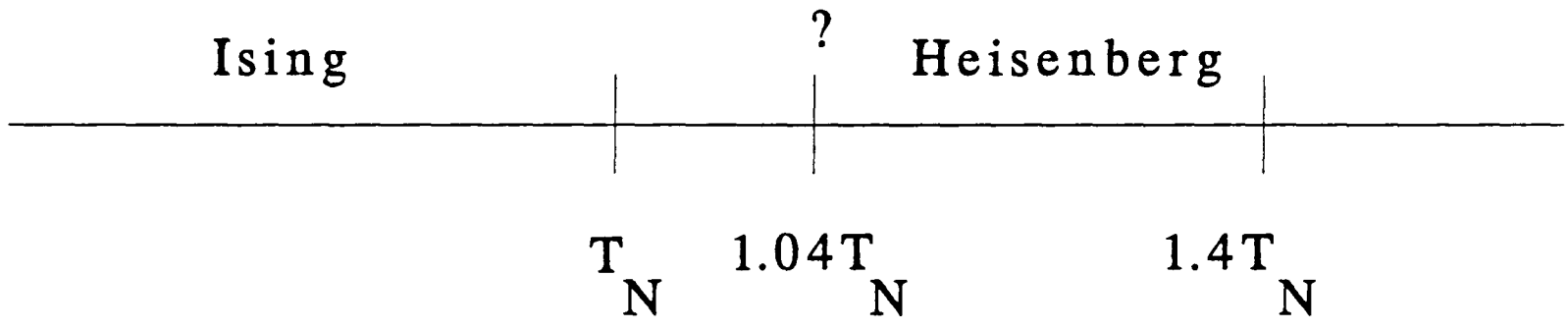


Figure 8.14: A summary of the behaviour of $KFeF_4$

## References


[8.1].J.G.Bednorz, K.A.Muller: Z.Phys. B64 189 (1986).

[8.2].E.Manousakis: Rev.Mod.Phys. 63 1 (1991).

[8.3].Y.Endoh, K.Yamada, R.J.Birgeneau, D.R.Gabbe, H.P.Jenssen, M.A,Kastner, C.J.Peters, P.J.Picone, T.R.Thurston, J.M.Tranquanda, G.Shirane, Y.Hidaka, M.Oda, Y.Enomoto, M.Suzuki, T.Murakami: Phys.Rev. B37 7443 (1988) and references therein.

[8.4].P.W.Anderson: Science 235 1196 (1987).

[8.5].S.Chakravarty, B.I.Halperin, D.R.Nelson Phys.Rev B39 2344 (1989).

[8.6].S.H.Shenker, J.Tobochnik: Phys.Rev.B22 4462 (1980).

[8.7].R.J.Birgeneau: Phys.Rev B41 2514 (1990).

[8.8].R.J.Birgeneau, J.Als-Nielsen,G.Shirane: Phys.Rev. B16 280 (1977).

[8.9].R.A.Cowley, G.Shirane, R.J.Birgeneau, H.J.Guggenheim: Phys.Rev. B15 4292 (1977), R.J.Birgeneau, H.J.Guggenheim, G.Shirane: Phys.Rev. B8 304 (1973), R.J.Birgeneau, J,Skalyo, G.Shirane: Phys.Rev. B3 1736 (1971).

[8.10].A.Desert, A.Bulou, J.Nouet: Sol. State Comm. 83 505 (1992).

[8.11].M.F.Collins: "Magnetic Critical Scattering" (Oxford University Press, 1989).

[8.12].H.Keller, I.M.Savic: Phys. Rev. B28 2638 (1983).

[8.13].P.C.Hohenberg: Phys. Rev. 158 383 (1967), N.D.Mermin, H.Wagner: Phys. Rev. Letts. 17 1133 (1966).

[8.14].T.Oguchi: Phys. Rev. 117 117 (1960).

[8.15].E.Manousakis, R.Salvador: Phys.Rev.Lett. 60 840 (1988), E.Manousakis, R.Salvador: Phys.Rev.Lett 61 1310 (1989).

[8.16].P.Hasenfratz, F.Niedermayer: Phys. Letts. B268 231 (1991).

[8.17].S.Tyc, B.I.Halperin: Phys.Rev B42 2096 (1990), S.Tyc, B.I.Halperin, S.Chakravarty Phys. Rev B62 835 (1989).

[8.18].B.I.Halperin: Jnl.Mgn.Mgn.Mat. 104-107 761 (1992).

[8.19].H.B.Tarko, M.E.Fisher: Phys.Rev B3 1217 (1975), M.E.Fisher, R.J.Burford: Phys.Rev 156 583 (1967).

[8.20].R.A.Cowley, M.Hagen, D.P.Belanger: J.Phys. C17 3763 (1984).

[8.21].M.Eibshutz, G.R.Davidson, H.J.Guggenheim, D.E.Cox: AIP Conf. Proc 5 670 (1972).

[8.22].R.A.Cowley: Methods of Experimental Physics Vol23C 1 (1987).

# Chapter 9

# $KFeF_4$- An X-ray Scattering Study of a Structural Phase Transition

$KFeF_4$ not only has interesting magnetic properties as discussed in the previous chapters, but in recent years there has been a growing interest in its structural phase transitions. Attention has focused on the structural phase transition near 400K, and the possibility that it is two transitions close together in temperature, with an intermediate, possibly incommensurate phase. The work discussed in this chapter was performed using single crystal x-ray diffraction techniques and concentrates on searching for evidence of the two-temperature transition and characterising the nature of the transition. In section 9.1, the experimental evidence for the two-stage phase transition and the possibility of an incommensurate phase is examined. The theoretical arguments suggesting an incommensurate phase are discussed in section 9.2, this is based on the Landau Theory of phase transitions introduced in chapter 7. Before going on to look at the data analysis in section 9.4, there is a brief description of the experimental set up and sample used in section 9.3.

## 9.1 Structural Phase Transitions in $KFeF_4$

The structural phase transitions in $KFeF_4$ have raised more interest than those in the isostructural compounds $KTiF_4$ and $KVF_4$[9.1] because of conflicting evidence as to the nature of the transitions in $KFeF_4$. Unlike these compounds which have one first-order transition, $KFeF_4$ has two transitions, with the possibility of the lower temperature one of these in fact being two transitions close together in temperature. The highest temperature transition is from an undistorted tetragonal structure (Phase I) known as the aristotype phase (Ammm). This undergoes a first-order transition to an orthorhombic structure (Amma) when the fluorine octahedra rotate by 11° around the *b*-axis causing a doubling of the *a* lattice parameter (see figure 9.1). This distortion of the structure was noted by G.Heger et

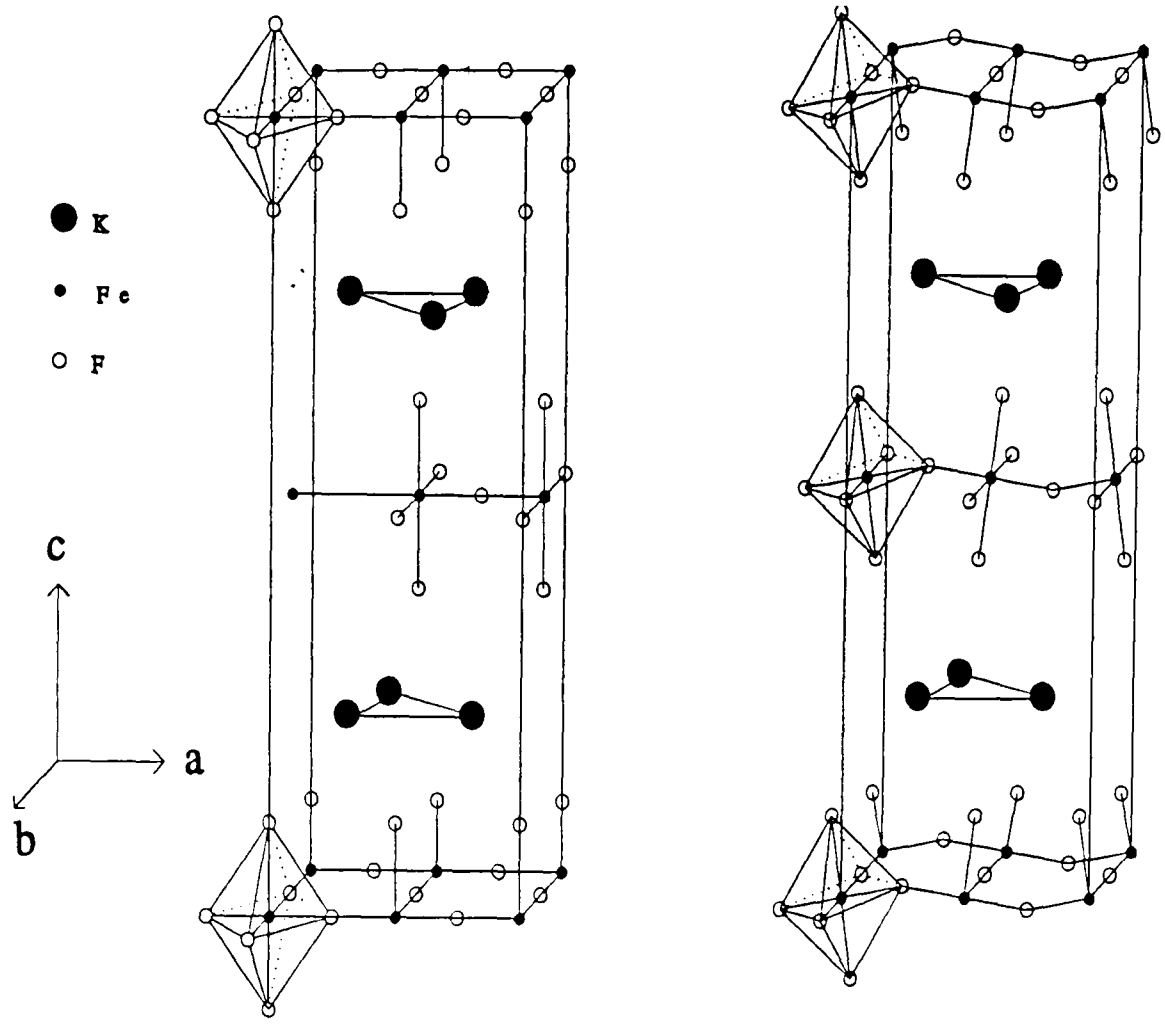


Figure 9.1: The two high-temperature phases of $KFeF_4$. The transition from Phase I to Phase II occurs via a rotation of the fluorine octahedra about the b-axis.

al[9.2], who performed one of the first studies on $KFeF_4$ using both x-ray and neutron diffraction techniques. The transition to the distorted structure occurs at 560K and has proved difficult to detect due to the deterioration of the samples above 470K. It has been observed successfully by one group[9.1] who measured the dielectric constant and who also used single-crystal x-ray diffraction techniques.

The second (and possibly two-temperature) phase transition in $KFeF_4$ has been much more widely studied using techniques such as Raman scattering[9.3], [9.4], and neutron[9.5] and x-ray diffraction[9.6], [9.7]. This transition is found around 400K and is due to two mechanisms: the first is a rotation of the fluorine octahedra by 8° around the *c*-axis[9.6], the second is a rotation of 2° about the *a*-axis[9.5], leading to a doubling of the *b* lattice parameter. Table 9.1 gives the lattice parameters in each of the three phases.

**Table 9.1 The lattice parameters in $KFeF_4$[9.5].**

| | *a* | *b* | *c* |
|---|---|---|---|
| Phase I (673K) | 3.8509 | 3.9233 | 12.48 |
| Phase II (413K) | 7.6621 | 3.9153 | 12.35 |
| Phase III (300K) | 7.6317 | 7.7998 | 12.33 |

Phase I (Ammm) $\rightarrow$ Phase II (Amma) $\rightarrow$ Phase III (Pmcn)

$a',b',c$ $\quad$ $2a',b',c$ $\quad$ $2a',2b',c$

T=560K $\quad$ T=400K

The phase transition at 400K is from the Amma (Phase II) structure to an orthorhombic structure, which in a classical three-dimensional analysis has the space group Pmcn[9.8]. This space group does not fully account for all of the reflection conditions found for the low temperature structure (Phase III). X-ray diffraction studies[9.9] have shown that there is a reflection condition in this system such that

*(hkl) with k even: k+2l=4n*

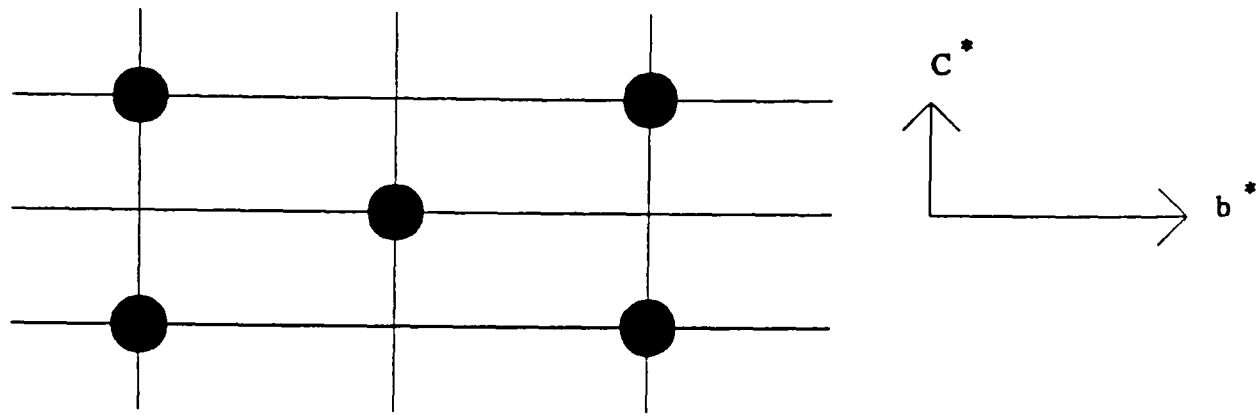


Figure 9.2a: The reciprocal space diagram for Phase II.

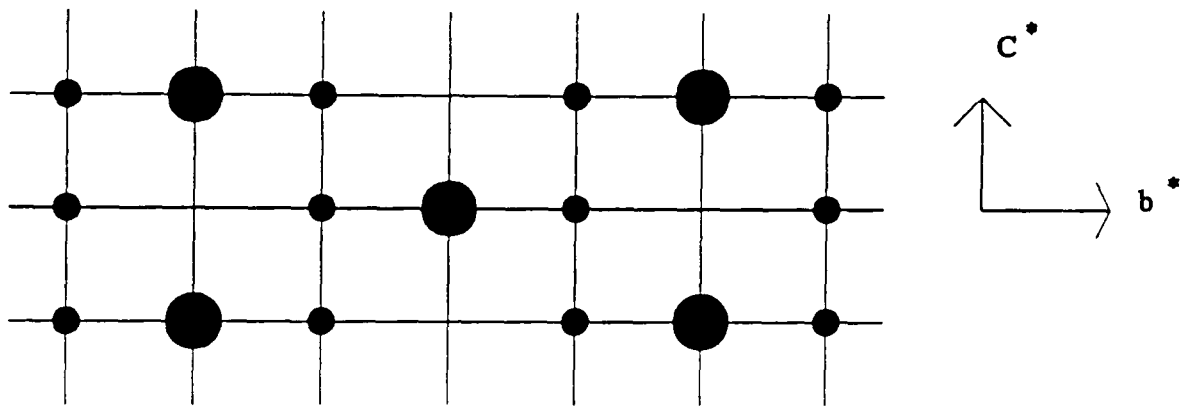


Figure 9.2b: The reciprocal space diagram for Phase III. The small dots represent the superlattice reflections.

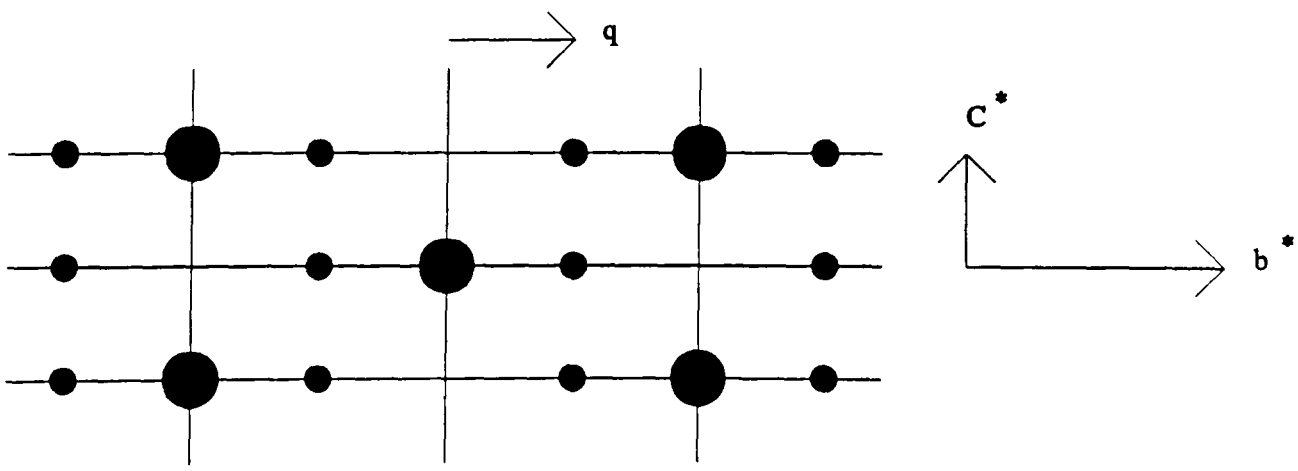


Figure 9.2c: The Phase III structure described as a modulation of Phase II by a wavevector q.

with the $k$ odd reflections representing the superstructure reflections. It is found that there is no three-dimensional space group which can explain this condition and a four-dimensional analysis must be used. This assumes that the weak peaks that appear in Phase III (which shall be referred to a superstructure peaks from now on) can be explained by thinking of phase III as a modulation of phase II. This modulation is the fourth dimension and it is found to be commensurate (see section 9.3.2) with the phase II lattice such that the wavevector is $q=½b^*$. Diagrams of the phase II and phase III reciprocal lattices in the (0kl) plane are shown in figure 9.2. Notice, the larger dots represent the strong structural peaks present in both phase II and phase III, while the small dots represent the weak superstructure peaks present in phase III only. This reanalysis of the structure is fully described by P.Sciau et al[9.9] and allows the number of structural refinement parameters to be reduced without contradicting previous studies describing the mechanisms behind the transition.

Problems have arisen when considering the order of the transition at 400K, and the possibility of there being two transitions with an intermediate incommensurate phase. Only two different experiments have shown evidence for two phase transitions near 400K, and none have shown any sign of an incommensurate phase. These are shown in table 9.2. In what follows, $T_c$ shall represent the phase transition temperature, which if a double transition is found shall denote the lower of the two transition temperatures. $T_*$ shall be used to represent the upper, hypothetical transition in the 400K region.

**Table 9.2 A summary of the previous experimental results.**

| Techniques | $T_c$/K | Order at $T_c$ | $T_*$/K | Order at $T_*$ |
|---|---|---|---|---|
| x-ray single crystal[9.10] | 398 | first | 410 | second |
| x-ray single crystal[9.7] | 393 | - | - | - |
| x-ray powder[9.9] | 395 | second | 408 | second |
| Raman single crystal[9.3] | 390 | first | _ | - |
| Raman single crystal[9.4] | 400 | first | _ | _ |
| specific heat[9.11] | 395 | tricritical | - | - |

Using x-ray powder techniques P.Sciau et al[9.9] have measured discontinuities in the slopes of dilatometric curves (ie lattice parameter versus temperature) of all three lattice parameters. The *a* and *b* lattice parameters were found to change at 395K, while the *c* lattice parameter was found to change at 408K. This implies that $T_c$=395K, while $T_*$=408K.

Saint-Gregoire[9.10] also has evidence for a two-stage phase transition. By using single crystal x-ray diffraction techniques a cusp in the temperature-dependence of the superlattice peak intensity was found at $T_c$=398K, indicating a first-order transition. This was confirmed by measuring the specific heat of a small single crystal. The intensity of the superstructure peaks was seen to persist above $T_c$, with the second phase transition being indicated by an increase in the width of the superstructure peaks at a temperature 12K above the cusp ($T_*$=410K). Although two transition temperatures are predicted by this experiment, no evidence was found for an incommensurate phase. The discontinuity in the intensity of the superstructure peaks at $T_c$ was not seen by P.Sciau[9.9], who concluded that the transitions were continuous at $T_c$ and $T_*$. There has also been evidence put forward by Saint-Gregoire in an earlier paper that in fact the transition in $KFeF_4$ is tricritical[9.11]. This was concluded after measuring the specific heat of a single crystal.

Desert et al[9.4] performed Raman scattering measurements of the phase transition and found that the soft mode which leads to the transition at 400K persists above $T_c$ and is predicted to finally disappear at about 550K. It is suggested that this may lead to diffuse scattering above the transition temperature, $T_c$, and that this may be the reason for intensity in this region, rather than the intensity being evidence for a double transition. Hidaka et el[9.7] like Saint-Gregoire[9.10] have seen intensity higher than background above $T_c$.

The experimental evidence describing the structural phase transitions in $KFeF_4$ is not conclusive. Evidence for a double transition has been seen by some groups, but not by others using similar techniques. There is also debate as to the order of the phase transition: first order, second order or perhaps even tricritical. This study on $KFeF_4$ helps to clear up some of the confusion.

In the next section there is a brief discussion of the soft modes which cause the

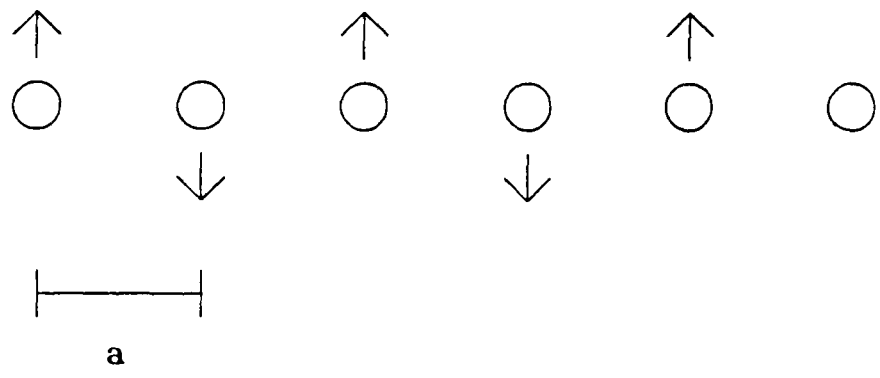


Figure 9.3a: Lattice vibrations of a structure with lattice spacing a.

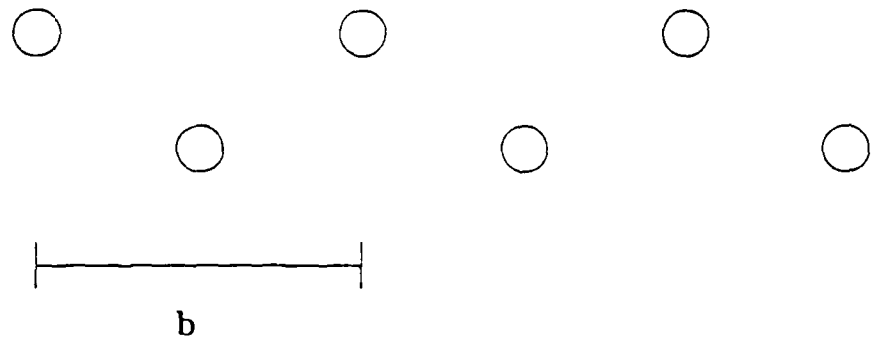


Figure 9.3b: Frozen-in structure with lattice spacing b=2a.

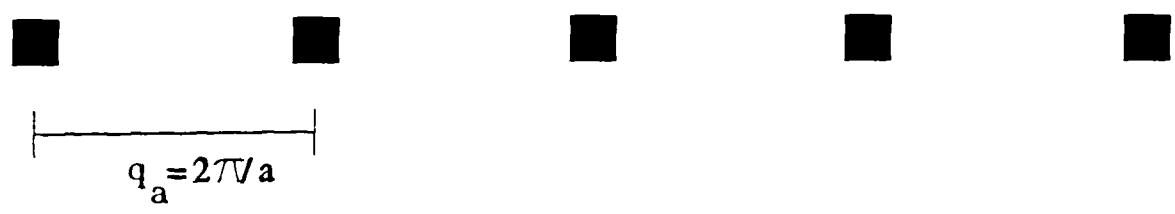


Figure 9.3c: Reciprocal lattice of 9.3a.


Figure 9.3d: Reciprocal lattice of 9.3b.

structural phase transition, and then the reasoning behind the suggestions for an incommensurate phase in $KFeF_4$.

## 9.2 Theory

Many displacive structural phase transitions are due to phonon instabilities, where the critical mode of the high-temperature phase has an imaginary frequency at 0K[9.12]. In a second-order transition, the phonon modes associated with the vibrations of the lattice has a frequency which slows down towards zero at $T_c$, in a first-order transition this condition is not satisfied. This critical vibration is known as a "soft mode" and was proposed by Cochran[9.13] for ferroelectric phase transitions and has been successfully applied to displacive phase transitions. The critical wavevector, $q_c$, of the particular mode determines the new modulation of the structure and at $T_c$ this can lead to new Bragg peaks appearing if the wavevector $q_c$ is non-zero (figure 9.3). The modulation shown in figure 9.3 is commensurate with the underlying structure of the crystal. This means the wavelength of the modulation, $b$, is an integer value of the lattice constant, $a$. This leads to new Bragg peaks at rational positions in reciprocal space, in this case at the 1/2 positions. An incommensurate phase occurs when the ratio $b/a$ is irrational, and is caused by a modulation of the crystal lattice which is not an integer of the underlying lattice[9.14].

Many systems contain incommensurate modulations. CuO is found to have an incommensurate antiferromagnetic phase as discussed briefly in chapter 6. This occurs between the fully ordered antiferromagnetic state and the paramagnetic region. Crystals in the $A_2BX_4$ family represent one of the largest groups exhibiting structural incommensurate modulation. In $K_2SeO_4$, Iizumi et al[9.15] showed how the incommensurate modulation arose from a minimum in the phonon dispersion relation that occurs at a wavevector intermediate to the zone boundary and the zone centre. In this case the wavevector of the modulation was $q_c=1/3(1-\delta)\mathbf{a}^*$, with $\delta$ being the displacement from the commensurate 1/3 position. At low temperatures this structure locks in to $q_c=1/3$. $BaMnF_4$ also has a structural incommensurate phase which has been studied using high resolution x-ray diffraction techniques[9.16]. It is unusual because the structure does not "lock-in" to a commensurate value as the system is cooled down. An exhaustive review of systems

exhibiting incommensurate modulation is given in reference [9.14].

The nature of the phase transition and whether a commensurate or incommensurate structure is allowed may be determined from a knowledge of the symmetry of the order parameter at the phase transition, and the terms which this allows in the Landau free energy. The order parameter for phase transitions was discussed in chapter 7, and is proportional to the displacement of the atoms from the undistorted phase[9.17].

In $KFeF_4$, group theory calculations based on Landau theory have suggested that the symmetry change involved in going from the Amma (Phase II) structure to the Pmcn (Phase III) structure cannot occur if the phase transition is second order. This arises from a study of the Landau free energy which for $KFeF_4$ has the following form[9.9]

$$G(y)=r\eta\eta^*+u(\eta\eta^*)^2+D(\eta^4+\eta^{*4}) \\ +i\sigma\left(\eta\frac{\delta\eta^*}{\delta y}-\eta^*\frac{\delta\eta}{\delta y}\right)+\chi\left(\frac{\delta\eta}{\delta y}\frac{\delta\eta^*}{\delta y}\right) \qquad \textbf{(9.1)}$$

In equation 9.1, the free energy has been written assuming that the representation of the order parameter which causes the symmetry change in $KFeF_4$ is two dimensional. A complex basis has been used, where $\eta$ and $\eta^*$ describe the normal mode coordinates of the phonon causing the phase transition, and have the form $\eta=\rho e^{i\phi(y)}$ with $\rho$ as the amplitude of the distortion and $\phi$ its phase[9.17]. In the free energy expansion for $KFeF_4$ this leads to terms suggesting that a purely second-order transition cannot exist between Phase II and Phase III. This form of the free energy is characteristic of a phase transition known as a "lock-in" phase transition. In these transitions as the system is cooled down there is a continuous phase transition to an incommensurate phase which is followed at lower temperatures by a first-order lock-in transition to a commensurate value close to the incommensurate structure, as seen in $K_2SeO_4$. The third term in equation 9.1 is the lock in energy, also known as the Umklapp term. When this term dominates the structure locks into a commensurate structure via a first-order transition. The fourth term is the Lifshitz invariant which if dominant can lead to an incommensurate modulation of the structure. The only way to avoid this modulated structure is for the transition to be first order. In $KFeF_4$, the transition at $T_*$ is the one which will determine whether or not there is an incommensurate phase. Some experiments have predicted

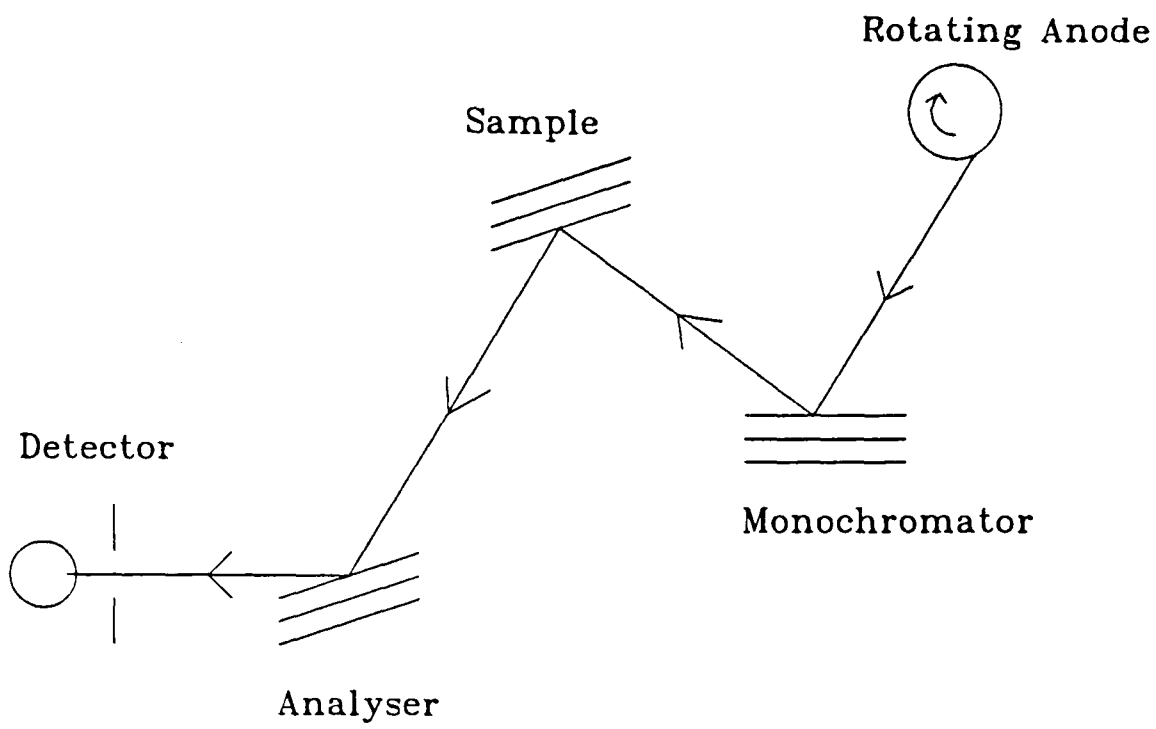


Figure 9.4: A schematic diagram of the x-ray triple-axis spectrometer.

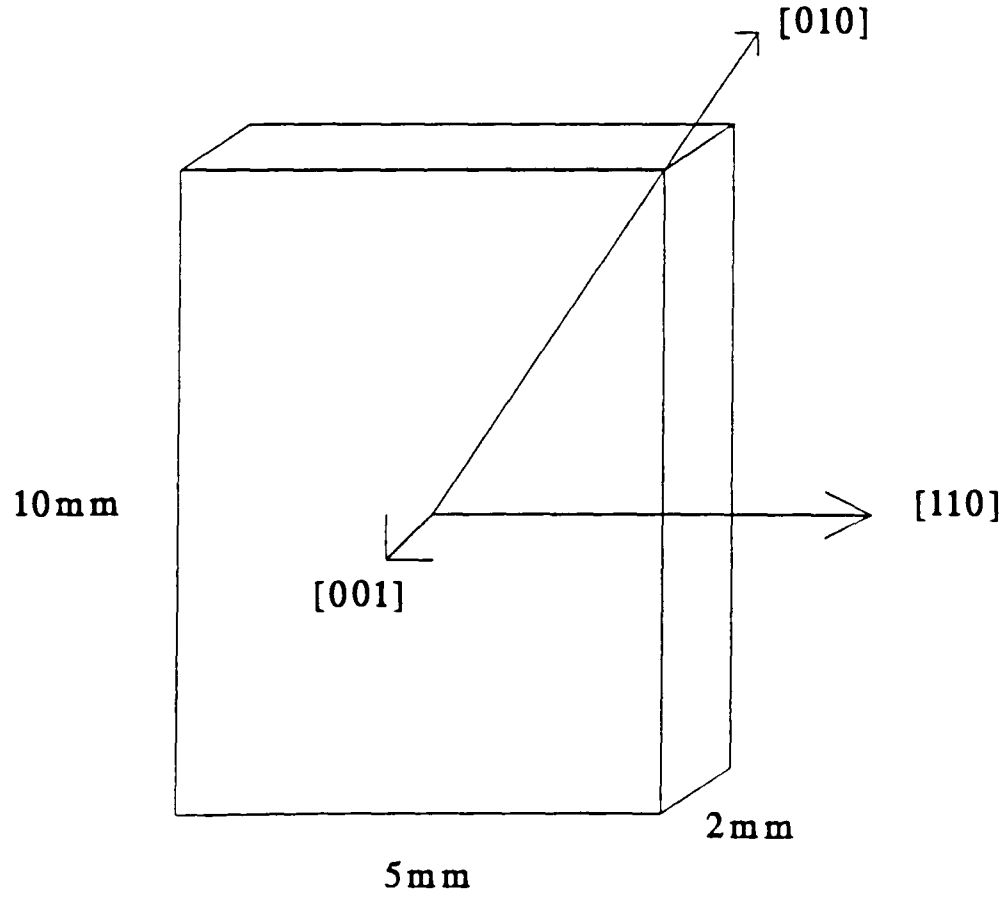


Figure 9.5: A sketch of the crystal showing the crystallographic directions.

this may be a continuous transition with the possibility of an incommensurate phase (see table 9.2). The fifth term is the elastic gradient energy, and acts to make the order parameter homogeneous[9.14].

## 9.3 Experimental Details

To study the structural phase transition in $KFeF_4$, a triple-axis x-ray diffractometer has been used. This is similar in many ways to the neutron triple-axis spectrometers employed during the studies of the magnetic properties of $KFeF_4$. A description of the instrument is given in section 9.3.1. This is followed in section 9.3.2 by a discussion of the sample used.

### 9.3.1 The X-ray Triple-Axis Spectrometer

The x-ray triple-axis spectrometer used to perform the experiment was a Huber two-circle diffractometer in the triple-axis configuration with a rotating anode source. The two circles allow the sample and detector to move independently. The triple-axis configuration involves analyser and monochromator crystals, just as in the neutron TAS. For this experiment the analyser and monochromator were both pyrolytic graphite crystals scattering from the (002) planes. They are used to select the Cu $K_\alpha$ (1.54Å) line which is produced from the Stoe rotating anode source operating at 6kW. This produces a beam size 5mmx1mm. To detect the scattered x-rays, He detector tubes with beryllium windows were used. Using this arrangement and by putting lead shielding around the detector housing, the background was reduced to less than 1 count per second. The resolution for the instrument with this set up is approximately $0.01Å^{-1}$ in the plane, and $0.1Å^{-1}$ vertically[9.18]. A diagram of the x-ray spectrometer is shown in figure 9.4.

### 9.3.2 Sample Details

The single crystal of $KFeF_4$ was grown by the Bridgman-Stockbarger technique in a platinum crucible and has dimensions of 5mmx10mmx2mm with the *c*-axis parallel to the 2mm direction. It proved impossible to line the crystal up when looking at faces with this 2mm

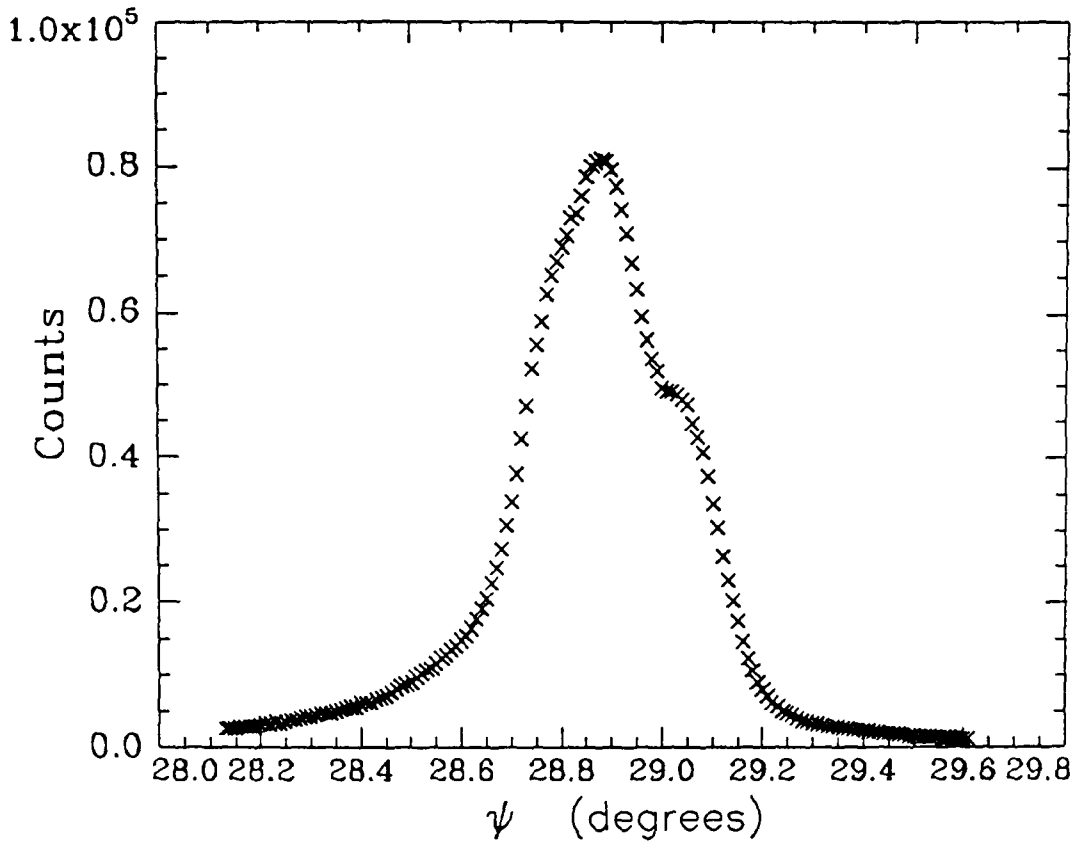


**Figure 9.6: Rocking curve of the (0,0,8) Bragg peak. ψ is the sample angle.**

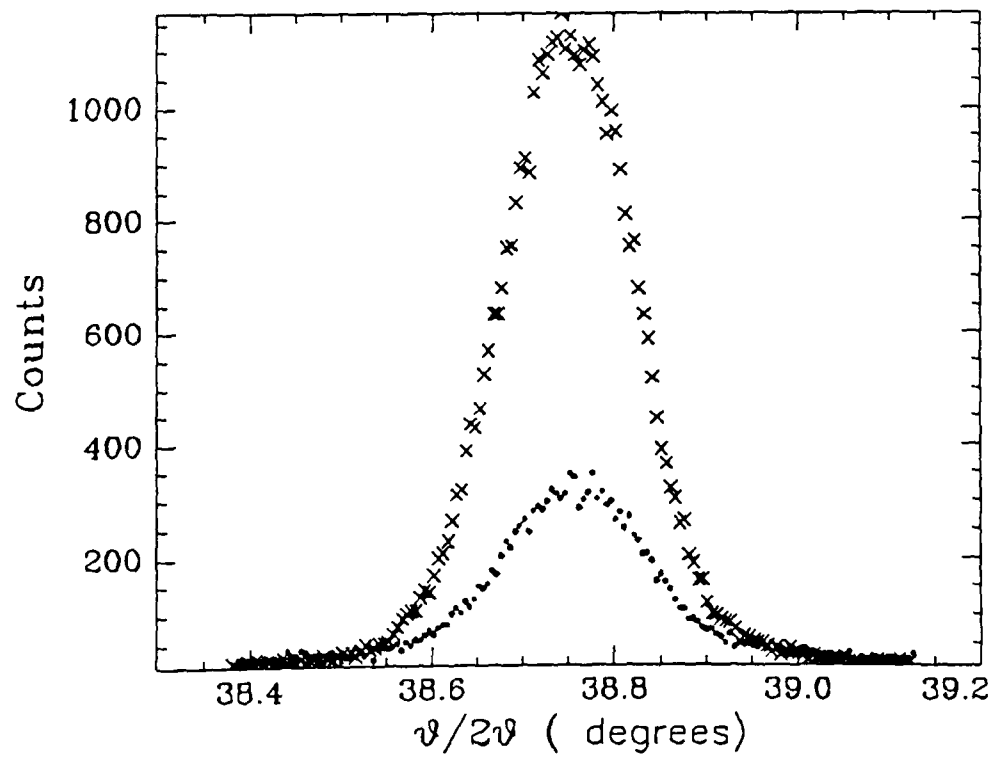


**Figure 9.7: Measuring the integrated intensity of the (0,1,7) superlattice reflection. The crosses represent a scan at T=382K, the dots T=387K.**

dimension. Laue patterns from these faces were almost powder-like and thus it was only possible to line the crystal up with the *c*-axis in the plane (see figure 9.5). During the course of this experiment the sample was aligned so that reflections in the (hhl) and the (0kl)-plane could be accessed. A rocking curve from the (0,0,8) reflection is shown in figure 9.6. This clearly shows that the sample contains at least two crystallites 0.1° apart.

To perform a temperature-controlled experiment to an accuracy of ±0.1K, the crystal was mounted on a copper block with the large flat face stuck to the copper using silver paste to give good thermal contact. A platinum resistance thermometer was embedded in the copper block and was monitored using a Lakeshore 330 Autotuning temperature controller in the manual mode. This also controlled the heater which was located at the base of the copper block. This arrangement was placed in a steel casing with a rotary vacuum pump attached (pressure=$10^{-4}$mbar) to create a stable thermal environment. The steel casing has aluminium coated mylar windows to allow the x-rays to reach the sample.

## 9.4 Experimental Results

Two different types of scans were performed on this sample to discover the nature of the phase transition in the 400K region. The first involved measuring the integrated intensity of some superstructure peaks as a function of temperature. Using these data the presence of one first-order transition has been confirmed. The second set of scans were concerned with measuring the widths of superlattice peaks to see if any anomalies in the widths were present. Finally, some scans were taken to look for evidence of an incommensurate phase.

### 9.4.1 Integrated Intensity Measurements

Radial scans were performed about the superstructure peaks that are predicted to disappear as the sample is heated from Phase III to Phase II. These scans were used to give a measure of how the integrated intensity of the superstructure peaks change with temperature. Particular superlattice reflections (*k* odd) were chosen so as to reduce the possibility of second-order scattering from main structural peaks which have a reflection condition k+2l=4n when k is even. Thus the following superstructure peaks were chosen: (0,1,7), (0,-1,7), (1,1,10) and

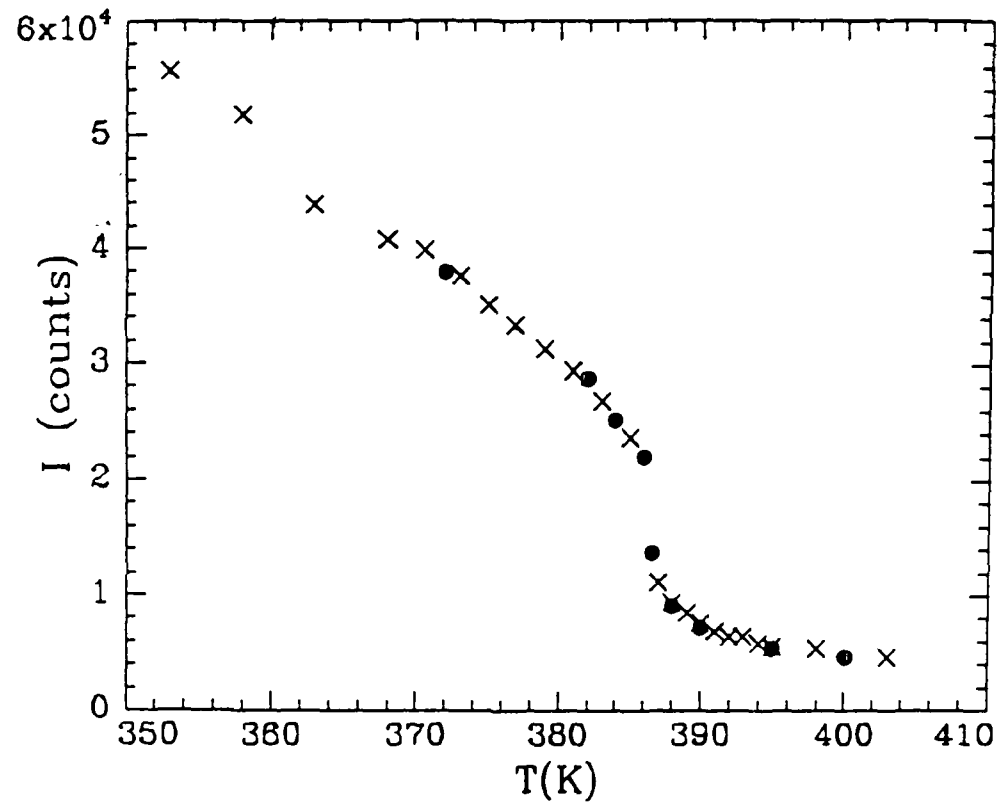


Figure 9.8: The temperature dependence of the (-1,-1,10) superlattice reflection. The crosses are points taken while heating, the dots while cooling.

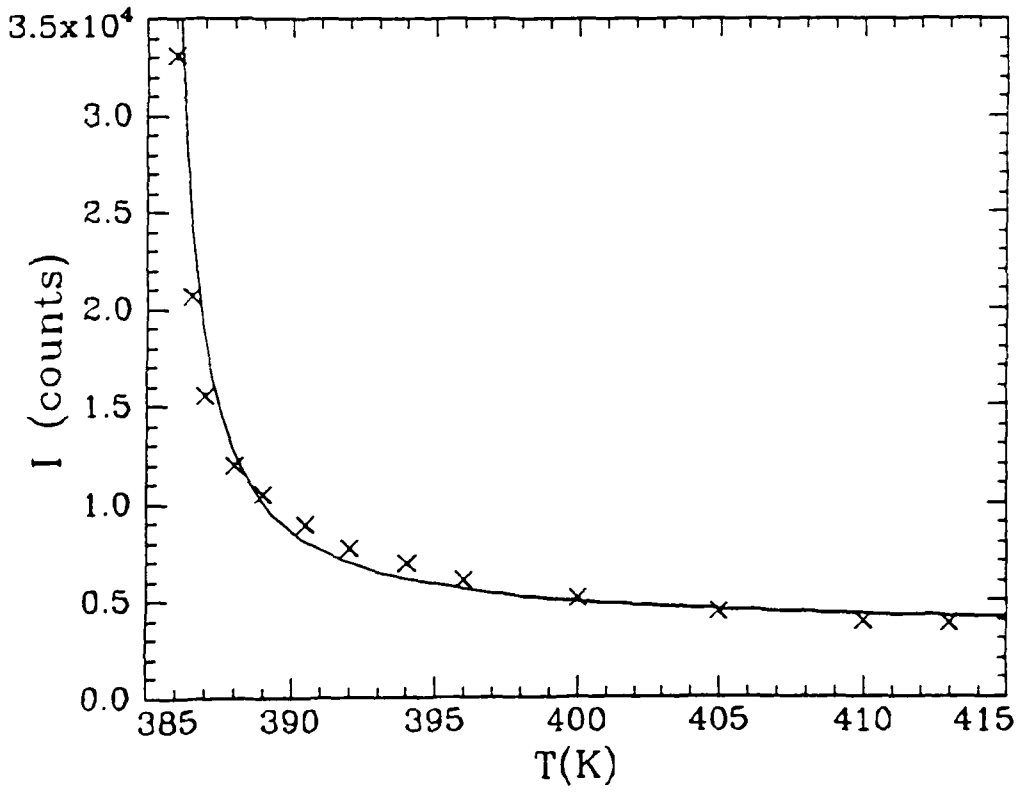


Figure 9.9: Continuous behaviour of the intensity of the (0,-1,7) reflection above $T_c$. The solid line is a simulation of power law behaviour.

(-1,-1,10) (with the lattice parameters defined for phase III). Figure 9.7 shows scans from the (0,1,7) reflection at two temperatures, one above and one below $T_c$. Figure 9.8 shows how the integrated intensity of the (-1,-1,10) peak changes with temperature. In figure 9.9, the tail of the integrated intensity of the (0,1,7) reflection shows continuous behaviour. From these intensity measurements it is clear that there is no evidence for a double phase transition. Note that the integrated intensity has been normalised at each temperature using the integrated intensity of the (2,2,9) Bragg reflection for the (h,h,l)-plane and the (0,2,7) reflection for the (0,k,l)-plane. This was done because no monitor count is available using this equipment. It should also be noted that measurements of the intensity of the (-1,-1,10) reflection were taken while heating and cooling the sample to see if any hysteresis could be detected. Hysteresis is a characteristic of a first-order phase transition[9.19], but was not detected during this experiment.

## 9.4.2 Fitting the Integrated Intensity Data

To characterise the nature of the phase transition the data has been fitted to two different models describing the temperature dependence of the superlattice reflections and thus the order parameter. As discussed in chapter 7, second-order phase transitions can be identified by power-law behaviour and in this case the integrated intensity would be described by the following relation

$$I(T)=A\left(\frac{T_c-T}{T_c}\right)^{2\beta} \qquad (9.2)$$

For classical second-order phase transitions the critical exponent $\beta=1/2$, and if the transition was in fact tricritical Landau theory gives $\beta=1/4$. Notice that if the system does not behave like a classical three-dimensional system the critical exponents may follow scaling behaviour for low-dimensional systems (as discussed in chapter 7) when the Landau theory fails.

When fitting the data to the model, a background term was subtracted from the data. A typical fit is shown in figure 9.10, and the parameters extracted are shown in table 9.3. Looking at different reflections in the same plane gives some idea of the importance of

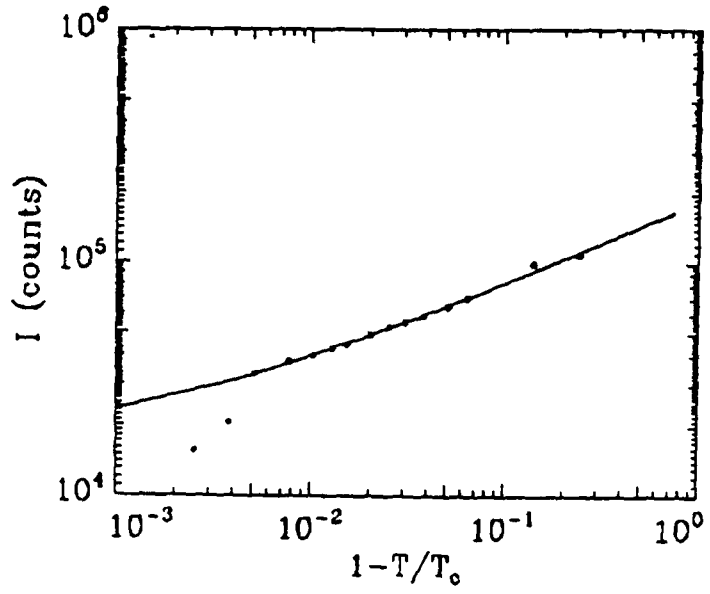


**Figure 9.10: Fit of intensity of the (0,1,7) integrated intensity to power law behaviour.**

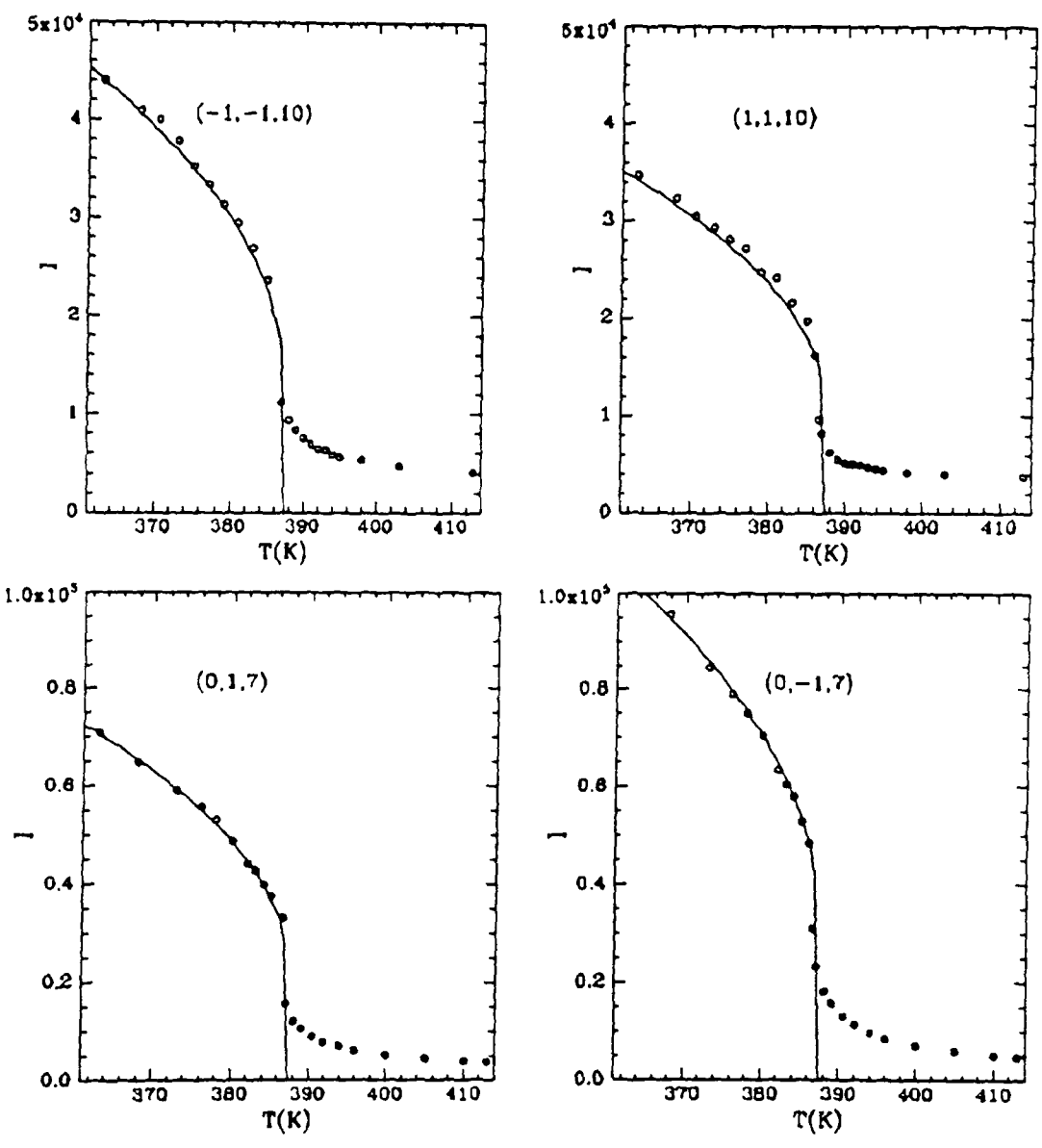


**Figure 9.11: The temperature dependence of the integrated intensity of the superlattice reflections. The solid line represents the fits to first-order behaviour.**

extinction effects. With this data the fits from all the reflections are similar, suggesting that extinction is not playing a large part in any discrepancies in the low values of critical exponent extracted from the fits. The results show that all data sets are fitted with approximately the same parameters, with $T_c$=388.1±1.6K and 2β=0.40±0.08. These results are in agreement with the fits by Saint-Gregoire[9.10], and lie close to those predicted for a tricritical phase transition (2β=0.5).

**Table 9.3 Fits to Power-Law Behaviour**

| Reflection | $T_c$/K | 2β | $\chi^2$ |
|---|---|---|---|
| (0,1,7) | 388.6±0.3 | 0.37±0.03 | 1.5 |
| (0,-1,7) | 388.1±0.3 | 0.40±0.07 | 4.4 |
| (1,1,10) | 388.2±0.4 | 0.40±0.03 | 5.6 |
| (-1,-1,10) | 387.5±1.5 | 0.39±0.03 | 3.2 |

The second model to which the data were fitted was that of a first-order phase transition. Using this model the integrated intensity has the following temperature dependence

$$I(T)=\frac{2}{3}I(T_c)\{1+[1-\frac{3}{4}(\frac{T-T_b}{T_c-T_b})]^{\frac{1}{2}}\} \qquad (9.3)$$

which arises directly from the Landau free energy (see chapter 7). When fitting to this model it was found necessary to fix $T_c$ at 386K and $I(T_c)$ at the values determined from the experiment and to allow only $T_b$ to vary. ($T_b$ defines the lower limit of the metastability of the high temperature phase.) Only data points at $T_c$ and below were included. The persistence of intensity above $T_c$ is the subject of debate and shall be discussed in section 9.5. The results of the fits to this model are shown in figure 9.11 and table 9.4 has a summary of the parameters extracted. These fits suggest that the data are well described by a first-order model (equation 9.3). This, along with the low values of critical exponents obtained from the power law behaviour suggest that the transition in $KFeF_4$ at 386K is of first order. The fact that no hysteresis was seen (figure 9.8) implies that this is only a weakly first-order transition.

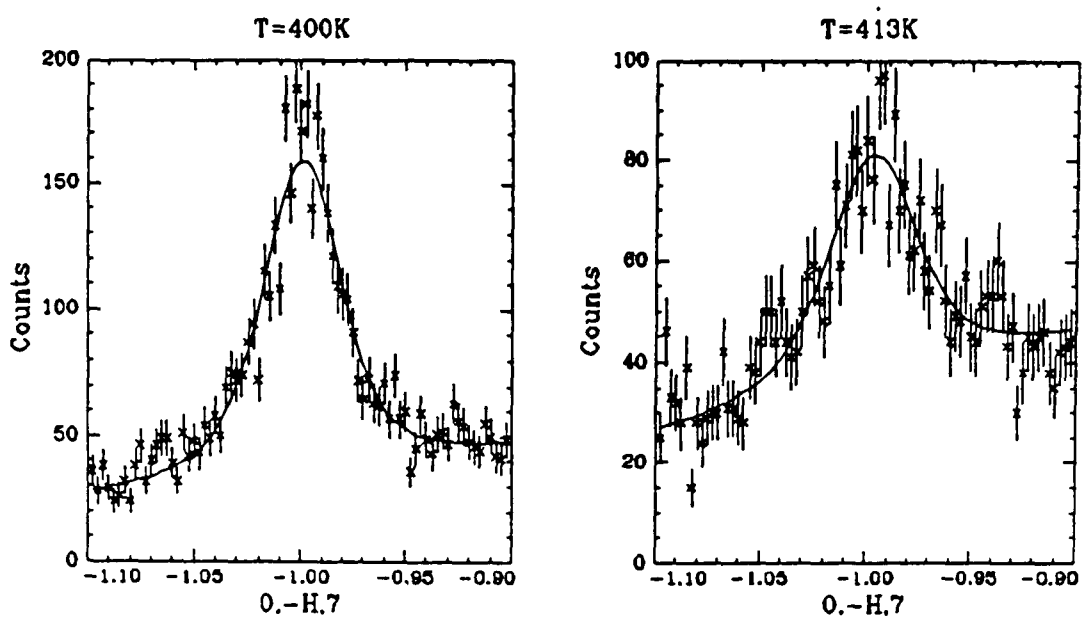


Figure 9.12: Scans of the superlattice reflections along the $b^*$-direction. The solid line is the fit to a Lorentzian convoluted with a Gaussian

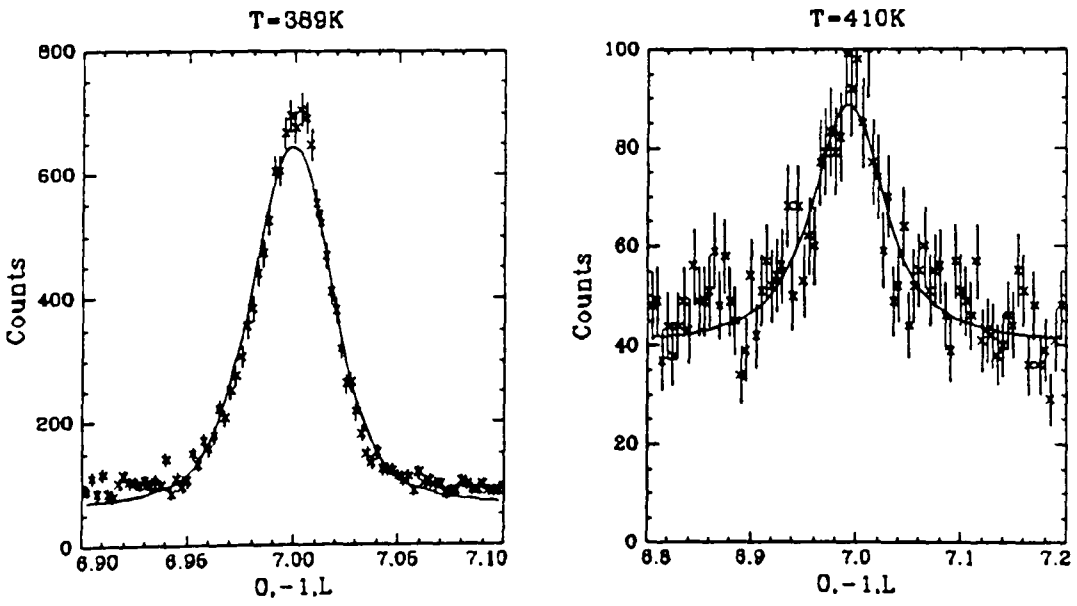


Figure 9.13: Scans along the $c^*$-direction, with fits to a Lorentzian convoluted with a Gaussian.

**Table 9.4 Fits to First-Order Behaviour**

| Reflection | $T_b$ | $\chi^2$ |
|---|---|---|
| (0,1,7) | 382.2±0.1 | 1.9 |
| (0,-1,7) | 382.0±0.1 | 0.7 |
| (1,1,10) | 382.6±0.1 | 2.0 |
| (-1,-1,10) | 383.0±0.1 | 3.5 |

## 9.4.3 Widths of the Superstructure Peaks

Having detected no signs of a second transition while studying the intensity of the superstructure peaks it was decided to look at the widths of these peaks as a function of temperature. Scans in reciprocal space along the $\mathbf{b}^*$ and $\mathbf{c}^*$ directions performed when in the (0kl) orientation show how the width of the superlattice peaks changed. Figures 9.12 and 9.13 show that the general trend is for the intensity of these peaks to decrease with increasing temperature, while the width appears to increase. As was mentioned in section 9.3.2, during this experiment the background count was found to be less than 1 count per second (N.B.the count time for scans in figures 9.12-9.13 was 60 seconds per point). This is much better than previous studies which had a background count of the order 30 counts per second[9.10]. It was thus possible to detect intensity above background at the superlattice positions at temperatures of 430K; possible reasons for this persistence of this intensity will be discussed in section 9.5. The intensity may persist at temperatures higher than this, but worries about sample deterioration prevented any further heating.

To extract widths from the data a Lorentzian was used to describe the diffuse scattering

$$S(Q)=\frac{A}{(\kappa^2+(Q-\tau)^2)} \qquad \textbf{(9.4)}$$

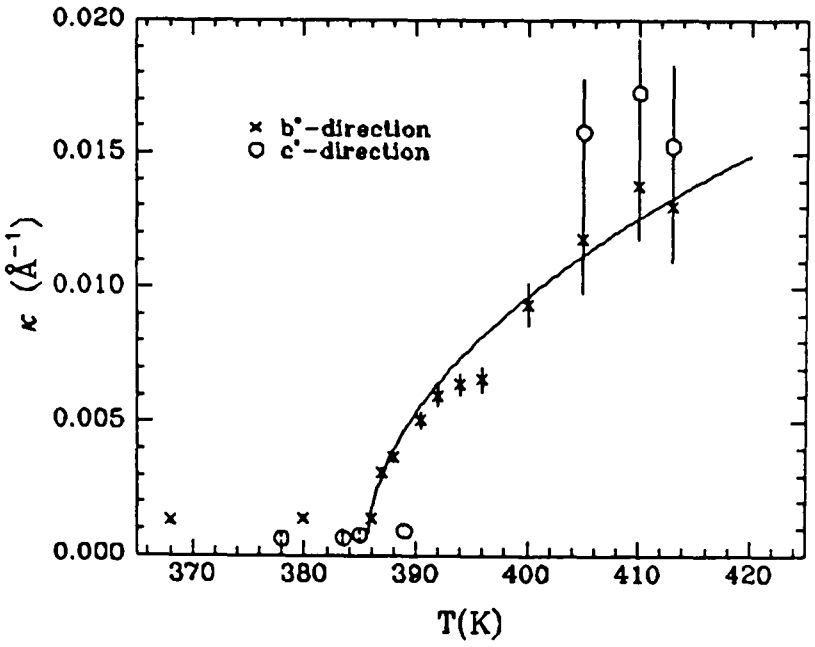


Figure 9.14: The widths, κ, extracted from the fits to equation 9.4. The line is a simulation of power law behaviour, showing the increase in κ is continous.

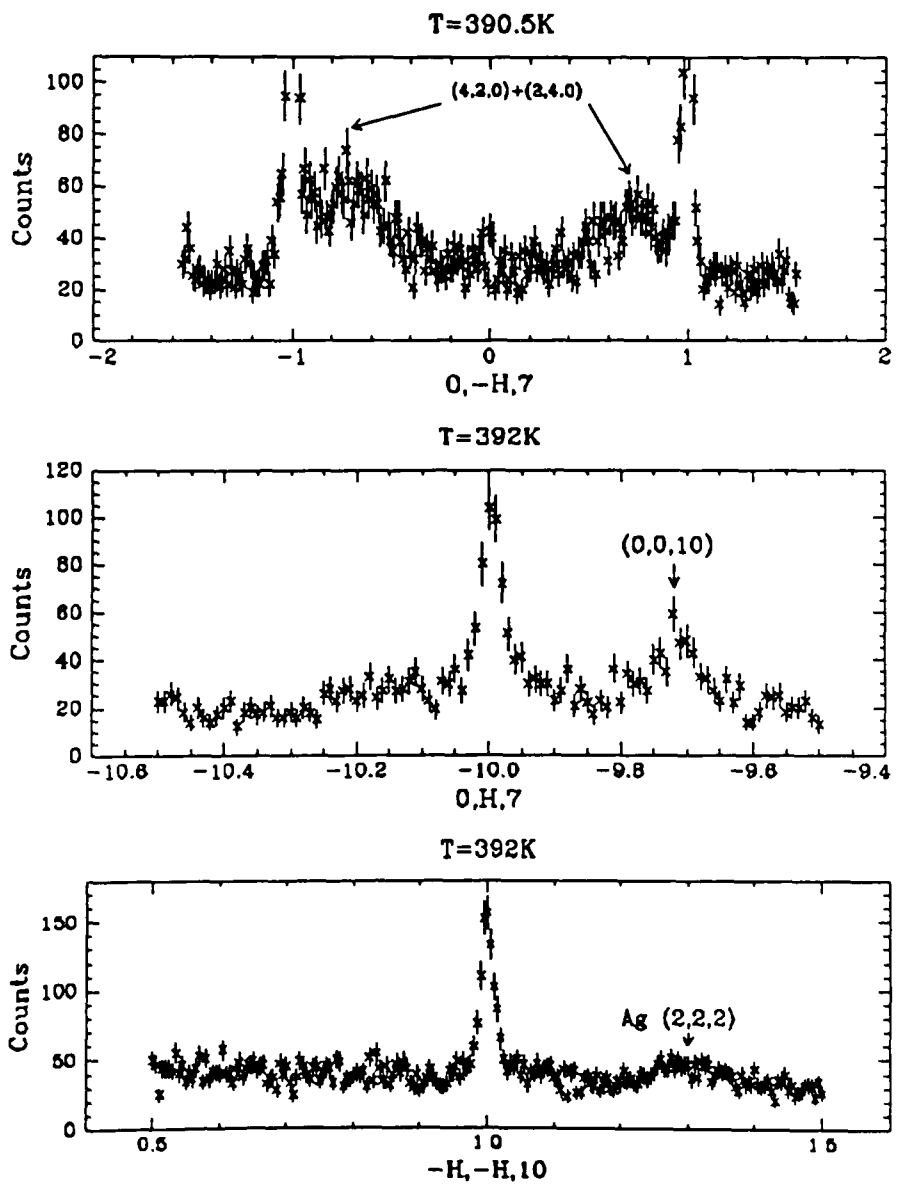


Figure 9.15: Looking for the incommensurate phase. Notice the contamination from $KFeF_4$ powder lines and from the silver paste.

In equation 9.4, $\tau$ is the reciprocal lattice point at the centre of the scan and **Q** is the measured wavevector transfer. This was convolved with a Gaussian which had a width equal to that of the non-superlattice peaks in the direction being scanned. In the $\mathbf{b}^*$ direction the Gaussian had a FWHM of $0.024\text{Å}^{-1}$, while in the $\mathbf{c}^*$ direction it was found to be $0.018\text{Å}^{-1}$. Note this is not a full instrumental resolution convolution because the vertical resolution has not been included, and thus the widths extracted cannot be directly compared to the correlation length, but it does give some idea of the behaviour of the widths as a function of temperature. When fitting the data a background term was included, which was kept fixed for each superlattice scan at each temperature. Notice in the $\mathbf{b}^*$ direction a sloping background was necessary (see figure 9.12).

The widths extracted from the fits are shown in figure 9.14. The solid line is a simulation of power-law behaviour and suggests that the increase in the widths is continuous in this region, with no indication of an anomaly caused by a second phase transition. The data suggests that the widths increase at $T_c \approx 386\text{K}$ and corresponds to the discontinuity in the intensities due to the first-order phase transition, with no evidence for a second transition.

These results are not the same as those extracted by Saint-Gregoire et al[9.10] from their x-ray single-crystal data. They did not see any evidence for an increase in the widths of the superstructure peaks at $T_c$. Their data did not show a change in any of the widths until 12K above the original transition, and then it was only increases in widths in the $\mathbf{a}^*$ and $\mathbf{c}^*$ directions, the widths in the $\mathbf{b}^*$ direction being resolution limited at all temperatures.

### 9.4.4 Looking for the Incommensurate Phase

It was thought worthwhile to look for an incommensurate phase in the region above $T_c$, as the detection of such a structure would be conclusive proof of a double transition. The only phonons studied have been measured with Raman scattering, thus it is difficult to predict where the incommensurate wavevector will be, and therefore where to look for extra peaks in reciprocal space. This could be done with neutron scattering techniques, by measuring the full dispersion relation and looking for a flat phonon branch which softens as $T_c$ is approached.

Saint-Gregoire[9.11] has suggested that the incommensurate modulation will be along the $\mathbf{b}^*$ direction. This is because the soft mode causing the phase transition is at $(0,\pi/b,0)$. This is also the modulation at the lock-in transition and since the Lifshitz invariant in the free energy would displace the incommensurate wavevector from a high-symmetry point $q_c$ to an arbitrary point $q_o = q_c + \sigma/\chi$ (from equation 9.1), this argument seems plausible. When looking for the incommensurate phase this direction was the one which was concentrated on, although scans in the [110] and [001] directions were also taken.

Figure 9.15 shows some of the data collected when looking for the incommensurate phase. It is clear from these scans the difficulties encountered when looking for such a phase using this crystal. Powder peaks were seen not only from the silver paste used to stick the sample on the copper block, but $KFeF_4$ powder lines were also detected. This was discussed in section 9.3.2, and was also a problem when trying to take x-ray Laue patterns from some of the sample faces. These powder peaks are necessarily found to be temperature independent, and cause streaks in reciprocal space. They make any signals arising from an incommensurate modulation, which are expected to be small, even more difficult to detect, and show just how important sample quality is in such an experiment.

In conclusion, using this sample no signs of any extra peaks arising from an incommensurately modulated structure have been seen. With the poor quality of the sample, and the uncertainty of the direction of a modulation (if indeed there is a modulation), these results are perhaps not surprising.

## 9.5 Conclusions

This experiment on $KFeF_4$ has shown that at 386K there is a weakly first-order phase transition. This is indicated in two ways:

1: Low values of $\beta$ extracted from the power law behaviour of the integrated intensity measurements ($\beta \approx 0.2$).

2: Good fits to the Landau theory for first-order phase transitions.

The value of $\beta \approx 0.2$ extracted for $KFeF_4$ is consistent with the values obtained for other systems with first-order transitions[9.20].

No sign of a second transition in the region above $T_c$ has been detected, with both the intensity above the first-order transition and the widths of the peaks in this region being continuous within the accuracy of the experiment. The persistence of intensity in the superlattice positions above $T_c$ was the evidence that some authors used for a second-order phase transition in $KFeF_4$ at $T_c$. This tail of intensity has been seen in other systems which have weakly first-order structural phase transitions. For example in $RbCaF_3$[9.21], which has a first-order transition at 200K, is found to have diffuse scattering in the region above the first-order transition. In that experiment it was shown that the scattering contained two components corresponding to two different length scales in the sample. The first had a Lorentzian shape as expected for diffuse scattering from soft modes. The other had a Lorentzian squared shape which had a width that decreased continuously to zero as $T_c$ was approached, but whose amplitude was different from that of the broad critical scattering. It was found that this component was dependent on sample quality, poorer qualities having more scattering and is thus thought to be due to defects in the sample. This type of behaviour has also been seen in neutron scattering studies and is often referred to the "central peak"[9.22]. Tails in the temperature dependence of the square of the order parameter in first-order systems have also been seen using linear birefringence techniques on the fluoro-perovskite structures[9.23]. Thus in $KFeF_4$ the presence of intensity in the region above $T_c$ does not contradict the first-order nature of the transition.

It is also thought that these results are not inconsistent with the results of Saint-Gregoire[9.10]. They took as evidence for a second transition temperature an increase in width of the superlattice reflection 12K above $T_c$. This could mean that their resolution was so poor that no effective change in the widths could be detected until the diffuse scattering became sufficiently wide. (Nb. in the $\mathbf{b}^*$ direction their superlattice reflections were always resolution limited.)

The only remaining conclusive evidence for the double phase transition comes from P.Sciau et al[9.9], who saw two different temperatures when studying the lattice parameters.

## 9.6 Further Work

To prove conclusively if there is an incommensurate phase in $KFeF_4$, a careful study of the phonon dispersion relations using neutron scattering techniques could be done. Neutron techniques can also be used to look for a central-peak as seen in other structural phase transitions. This will help determine if the extra intensity above $T_c$ is similar to the intensity found in the fluoro-perovskite structures or if it is related to a second upper transition. A higher resolution x-ray scattering experiment could be performed to look for the two-length scales, this should be done on a better quality sample than the one used in this experiment, because intensity arising from different pieces of crystal makes the data difficult to analyze.

## References


[9.1].M.Hidaka, B.J.Garrard, B.M.Wanklyn: J.Phys. C: Solid State Phys. 12 2737 (1979).

[9.2].G.Heger, R.Geller, D.Babel: Sol. State Com. 9 335 (1971).

[9.3].A.Maciel, J.F.Ryan: Jnl de Physique, Colloque C6, 42 (1981).

[9.4].A.Desert, A.Bulou, J.Nouet: J.Phys:Condense Matt. 4 1023 (1992).

[9.5].A.Desert: Doctorate Thesis, L'Universite du Maine (1990).

[9.6].P.J.Lapasset, P.Sciau, J.Moret, N.Gros: Acta Cryst. B42 258 (1986).

[9.7].M.Hidaka, Z.Y.Zhou, B.M.Wanklyn: Phys. Stat. Sol. A115, 149 (1989).

[9.8].P.Saint-Gregoire, R.Almairac, J.Lapasset, J.Moret: Phys. Stat. Sol. A120 K25 (1990).

[9.9].P.Sciau, D.Grebille: Phys. Rev. B39 11982 (1989).

[9.10].P.Saint-Gregoire, A.Perez, R.Almairac,V.Sanovec: Ferroelectrics 105 195 (1990).

[9.11].P.Saint-Gregoire, A.Perez, R.Almairac, M.Lopez: Phys. Sat. Sol. A87, K1 (1985).

[9.12].M.T.Dove: "Introduction to Lattice Dynamics" (Cambridge University Press, 1993).

[9.13].W.Cochran: Adv. Phys. 9 387 (1960), Adv.Phys. 10 401 (1961).

[9.14].H.Z.Cummins: Physics Reports 185 211 (1990).

[9.15].M.Iizumi, J.D.Axe, G.Shirane, K.Shimaoka: Phys. Rev B15, 4392 (1977).

[9.16].T.W.Ryan: J.Phys C: Solid State Phys. 19 1097 (1986).

[9.17].R.A.Cowley: Adv. Phys. 29 1 (1980).

[9.18].M.J.Harris: J.Phys: Condens. Matter 5 5773 (1993).

[9.19].G.Burns: Solid State Physics (Academic Press, 1985).

[9.20].U.J.Nicholls, R.A.Cowley: J.Phys C: Solid State Phys. 20 3417 (1987).

[9.21].A.Gibaud, T.W.Ryan, R.Nelmes: J. Phys. C: Solid State Phys. 20, 3833 (1987), A.Gibaud, R.A.Cowley, P.W.Mitchell: J. Phys. C: Solid State Phys. 20 3849 (1987).

[9.22].S.M.Shapiro, J.D.Axe, G.Shirane: Phys. Rev. B11, 4332 (1972).

[9.23].W.Kleeman, F.J.Schafer: Physica B97 145 (1979).